The Dissertation Committee for Chihhui Wu Certifies that this is the approved version of the following dissertation:

Fano-Resonant Plasmonic Metamaterials and Their Applications

Committee:

Gennady Shvets, Supervisor

Chih-Kang Shih

Alex Demkov

Xiaoqin Li

Andrea Alu

Fano-Resonant Plasmonic Metamaterials and Their Applications

by

Chihhui Wu, B.S.; M.S.

Dissertation

Presented to the Faculty of the Graduate School of

The University of Texas at Austin

in Partial Fulfillment

of the Requirements

for the Degree of

DOCTOR OF PHILOSOPHY

The University of Texas at Austin

August 2012

Fano-Resonant Plasmonic Metamaterials and Their Applications

Chihhui Wu, PhD

The University of Texas at Austin, 2012

Supervisor: Gennady Shvets

Manipulating electromagnetic fields with plasmonic nanostructures has attracted researchers from interdisciplinary areas and opened up a wide variety of applications. Despite the intriguing aspect of inducing unusual optical properties such as negative indices and indefinite permittivity and permeability, engineered plasmonic nanostructures are also capable of concentrating electromagnetic waves into a diffraction-unlimited volume, thus induce incredible light-matter interaction. In this dissertation, I'll discuss about a class of plasmonic structures that exhibit the Fano resonance. The Fano resonance is in principle the interference between two resonant modes of distinct lifetimes. Through the Fano resonance, the electromagnetic energy can be trapped in the so called "dark" mode and induce strong local field enhancement. A variety of Fano resonant nanostructures ranging from periodic planar arrays to simple clusters composed of only two particles are demonstrated in this dissertation. By artificially designing the dimensions of the structures, these Fano-resonant materials can be operated over a broad frequency range (from visible to mid-IR) to target the specific applications of interest. In this dissertation, I'll show the following research results obtained during my PhD study: (1) the double-continuum Fano resonant materials that can slow down the speed of light over a broad frequency range with little group velocity dispersion. (2) Ultra-sensitive detection and characterization of proteins using the strong light-matter interaction

provided by the Fano-reonant asymmetric metamaterials. (3) Metamaterials absorbers with nearly 100 % absorbance, tunable spectral position, expandable bandwidth, and wide angle absorption. These Fano-resonant materials can have profound influences in the areas of optical signal processing, life science, bio-defense, energy harvesting and so on.

Table of Contents

List of Figures

Chapter 1

Introduction

1.1 INTRODUCTION

The study of plasmonic nanostructures and metamaterials has been an active area with great interests over a wide range of applications. Charge carriers and photons can be hybridized into a variety of plasmonic polaritons by shaping the geometries of the nanostructures, which is typically made of noble metals, and provide enormous light-matter interaction. Electromagnetic responses of these materials can be tailored by designing the geometries of the nanostructures and achieve exotic electromagnetic properties such as negative optical index, strong optical activity, slow light, non-reciprocal propagation and so on. With the development of various nanofabrication techniques, these composite materials with sub-wavelength size and exotic electromagnetic properties are being designed and produced for many applications.

In this dissertation, we will specifically discuss about the Fano resonance in plasmonic structures. The Fano resonance generally occurs when two resonant modes with very disparate quality factors are coupled together. In this case, the broadband resonance with a lower quality factor constitutes a background and interferes with the sharp resonance, resulting in an asymmetric lineshape in the far-field radiation. The most intriguing property of the Fano resonance is probably the strong dispersion near the sharp resonance. Since the group velocity of a homogeneous medium is given by $v_g = \frac{d\omega}{dk} = \left(\frac{n}{c} + \frac{\omega}{c}\frac{dn}{d\omega}\right)^{-1}$, it can be dramatically reduced near the Fano resonance, where $\frac{dn}{d\omega} \gg \frac{n}{\omega}$. Although we will focus our discussion in the electromagnetic responses of plasmonic nanostructures, the Fano resonance is a general phenomenon and can be found in many areas of physics. As we will see in the following Chapters, the strong dispersion of the

Fano resonance in plasmonic structures provides a number of advantages, including inducing strong near-field enhancement, tunability of spectral range, and enormous sensitivity to the environment or the applied analyte. During my PhD research, I have investigated several different plasmonic designs that demonstrate the Fano resonances. In this dissertation, I will discuss their intriguing properties, as well as their potential contribution to some of the most pressing challenges of our times: energy challenge, security challenge (especially biodefense), and life-sciences challenge. For example, our research in metamaterial absorbers provides means to enhance the efficiency of solar energy harvesting, while our work using Fano-resonant plasmonic platform demonstrates ultra-sensitive biomolecule detection that provides information on biomass, fingerprints, and conformational states simultaneously.

1.2 ORGANIZATION OF THIS DISSERTATION

The arrangement of my dissertation is as follows: in Chapter 2, I will discuss a general theoretical background of the Fano interference by using the coupled mode theory. For an arbitrary complex plasmonic structure, we focus on a set of resonant modes that dominate the optical properties of interest. Each resonant mode has assigned amplitude. The amplitude satisfies the linearized equation of motion similar to that of the harmonic oscillators. We also introduce electromagnetic coupling between different modes, which is parameterized with a coupling coefficient. In the so called electrostatic limit, this interaction typically originates from the capacitive coupling between the resonant modes. Several physical considerations are also implemented into the model, such as energy conservation and reciprocity of the electromagnetic waves. Using the coupled model established in Chapter 2, we are able to calculate physical quantities such

as surface reflectivity, effective permittivity, and group index of the medium. This coupled mode model describes the physics of the Fano interference very well, and will reoccurring many times in the discussion of the following Chapters.

In Chapter 3, we will consider a more complex situation of the Double-Continuum Fano (DCF) resonance, which involves two or more bright (dispersive) resonant modes and one dark (discrete) mode. We demonstrate the DCF by using a low-symmetry three-dimensional metamaterial as an example. Such metamaterial is described as a birefringent medium supporting a discrete "dark" electromagnetic state weakly coupled to the continua of two nondegenerate "bright" bands of orthogonal polarizations. It is demonstrated that light propagation through such DCF metamaterial can be slowed down over a broad frequency range when the medium parameters (e.g. frequency of the "dark" mode) are adiabatically changed along the optical path. Using a specific metamaterial implementation, we demonstrate that the DCF approach to slow light (SL) is superior to that of the EIT because it enables spectrally uniform group velocity and transmission coefficient over a broad frequency range.

In Chapter 4, we demonstrate ultra-sensitive detection and characterization of biomolecules using the Fano-Resonant Asymmetric MetaMaterials (FRAMMs) introduced in Chapter 3. By utilizing the strong light-matter interaction of the engineered metal surfaces, the technique provides a tag-free platform for studying the behavior and responses of biomolecules on functionalized surfaces. The FRAMM platform provides the following functionalities at the same time: (i) extremely sensitive detection of surface-binding biomolecules with thicknesses in the nanometer scale, (ii) quantitative measurement of the binding biomass, (iii) quantitative characterization of the biomolecular absorption lines (the so-called fingerprints), and (iv) the conformation states determination of the binding molecules by combining the aforementioned biomass

and fingerprint information. The prevalent existing tag-free biosensing technologies either monitor the refractive index change caused by biomass accumulation or measure the absorption fingerprints to characterize the molecules, but not both. The spectral shift approach is non-specific and the results can be misinterpreted when undesired molecules are bond to the platform. On the other hand, the fingerprinting approach is specific to the type of the molecules, but the biomass has to be determined by other means. The proposed FRAMM platform possesses the advantages from both approaches and simultaneously measures biomass and fingerprint intensity. The combination of the two properties is crucial for determining the conformational state of the molecules as well as enhancing the test throughput.

In Chapter 5, we propose and demonstrate the idea of nano-plasmonic protractor that utilizes the Fano interference between a metallic nanoparticle (MNP) and a barely visible emitting/scattering object (ESO). By using the MNP, we are able to achieve the following two things: (1) spectroscopically detecting the ESO, which is undetectable when standing alone because of the very small scattering cross-section, and (2) determining the position of the ESO relative to the MNP using the Polarization Spectro-Tomography (PST). The principle behind the PST is that the MNP is strongly depolarized by the ESO when the Fano resonance occurs, and therefore making the MNP highly anisotropic along one specific direction determined by the position of the ESO.

In Chapter 6, we demonstrate a simple metamaterial-based wide-angle plasmonic absorber, which is fabricated and experimentally characterized using angle-resolved infrared spectroscopy. The metamaterials are prepared by nano-imprint lithography, an attractive low-cost technology for making large-area samples. The matching of the metamaterial's impedance to that of vacuum is responsible for the observed spectrally selective "perfect" absorption of infrared light. The impedance is theoretically calculated

in the single-resonance approximation, and the responsible resonance is identified as a short-range surface plasmon. The spectral position of the absorption peak (which is as high as 95%) is experimentally shown to be controlled by the metamaterial's dimensions. The persistence of "perfect" absorption with variable metamaterial parameters is theoretically explained. The wide-angle nature of the absorber can be utilized for sub-diffraction-scale infrared pixels exhibiting spectrally selective absorption/emissivity.

A simple design paradigm for making broad-band ultra-thin plasmonic absorbers is introduced in Chapter 7. The absorber's unit cell is composed of sub-units of various sizes, resulting in nearly 100% absorbance at multiple adjacent frequencies and high absorbance over a broad frequency range. A simple theoretical model for designing broad-band absorbers is presented. It uses the single-resonance model described in the previous Chapter to describe the optical response of each sub-unit and employs the series circuit model to predict the overall response. Validity of the circuit model relies on short propagation lengths of the surface plasmons.

In Chapter 8, we present the concept of a Solar Thermo-photovoltaic (STPV) collection system based on large-area, nanoimprint-patterned film of plasmonic structures acting as an integrated Solar Absorber/Narrow-band Thermal Emitters (SANTE). The SANTE film concept is based on integrating broad-band solar radiation absorption with selective narrow-band thermal IR radiation which can be efficiently coupled to a photovoltaic (PV) cell for power generation. By employing low reflectivity refractory metals (e.g., tungsten) as a plasmonic material, we demonstrate that the absorption spectrum of the SANTE film can be designed to be broad-band in the visible range and narrow--band in the infrared range. A detailed balance calculation demonstrates the total STPV system efficiency exceeding the Shockley-Queisser limit for emitter temperatures above $T_e = 1200\,K$, and an efficiency as high as $41\,\%$ for $T_e = 2300\,K$. Emitter

temperatures in this range are shown to be achievable under modest sun concentration (less than 1000 suns) due to the thermal insulation provided by the SANTE film. Experimental demonstration of the wide-angle, frequency- selective absorptivity is presented.

Chapter 2

Theoretical Model for the Fano Resonances in Plasmonic Nanostructures

2.1 INTRODUCTION

Before proceeding to more specific designs of the Fano resonant structures, we discuss in this Chapter a general model that can be used to describe the Fano resonances. This mathematical model is based on the coupled mode theory [1, 2, 3, 4, 5], in which each resonant mode is represented by a harmonic oscillator with a given resonant frequency and a damping rate. By simply changing the dimensions of the plasmonic structures, the resonant frequencies can be tuned over a broad range from visible to THz to fit into the desired applications. On the other hand, the damping rates of the resonant modes are typically comprised of the resistive damping and the radiative loss. The resistive damping is an intrinsic property to the composing material and therefore poses a limit to the life time of the resonant modes [6]. The radiative loss, on the other hand, is more controllable by the plasmonic structure design.

In the following, we will refer to the resonant mode with high radiative loss and large bandwidth as the "bright" mode and the one with relatively much smaller radiative loss and narrower bandwidth as the "dark" mode. This is because in a typical scattering experiment, the bright mode has a much larger scattering cross section, and therefore appears to be bright, while the dark mode has a small scattering cross section and can sometimes be challenging to collect its scattering signal.

2.2 THE COUPLED MODE THEORY

The coupled mode theory allows one to decompose a complex physical system into a number of resonating sub-components with various resonant frequencies and lifetimes. It has been successfully developed to describe the responses of circuit components, transmission lines [1], photonic cavities and waveguides [5], and electromagnetic waves scattered from arbitrary objects [2, 3, 4]. In the simplest case with a single resonant mode and one excitation channel, the equations of motion from the coupled mode formalism read:

$$\frac{d}{dt}a = (-i\,\omega_0 - \gamma)a + \kappa^+ S^+, \tag{2.1}$$

$$S^- = \eta S^+ + \kappa^- a. \tag{2.2}$$

The amplitude of the resonance is denoted by a, and it is normalized such that $|a|^2$ corresponds to the energy stored in that resonant mode. ω_0 is the natural frequency of the resonance, and γ is the damping rate. The resonant mode is driven by an external flux, S^+, which is normalized such that $|S^+|^2$ is the incident power. In addition, there is also an outgoing flux from the system, which is denoted by S^-. The coupling coefficient between the resonant mode and the external fluxes, $S^\pm$, is denoted by $\kappa^\pm$, which has the dimension of $t^{-1/2}$. η in Eq. (2.2) represents the direct scattering of the incident flux without exciting the resonant mode. Suppose that S^+ represents the incident field impinging on a metamaterial film and S^- is the reflected field, then $\eta = 0$ corresponds to the case when the metamaterial is embedded in a transmissive medium (examples given in Chapter 4), and $\eta = -1$ when the metamaterials is backed by a mirror reflector (examples given in Chapters 6 and 7). In a more general case where the metamaterials sit on a partially reflective substrate, η is equal to the reflection coefficient of the substrate.

The damping rate, γ, is typically composed of two terms: $\gamma = \gamma_{ohm} + \gamma_{rad}$, where γ_{ohm} is due to the ohmic loss of the material and γ_{rad} is the radiative damping

8

due to coupling to S^-. There are a couple of constraints relating γ_{rad}, κ^+, and κ^-. First, we consider the case with $\gamma_{ohm} = 0$ and $S_+ = 0$. According to Eq. (2.1), $a = a_0 \exp(i\omega_0 t - \gamma_{rad} t)$ is a decaying mode. The rate of modal energy loss is equal to the outgoing flux, therefore $-2\gamma_{rad}|a|^2 = -|S^-|^2$. By the use of Eq. (2.2), one obtains $|\kappa^-|^2 = 2\gamma_{rad}$. Next, we consider the time-reversed solution, $\tilde{a}(t) = [a(-t)]^* = a_0 \exp(i\omega_0 t + \gamma_{rad} t)$, which corresponds to energy building up in the resonant mode. In the time-reversed situation, the outgoing flux becomes the incident flux, or $\tilde{S}^+ = S^-(-t)^*$. By substituting $\tilde{a}$ and $\tilde{S}^+$ into Eq. (2.1), one gets $2\gamma_{rad}\tilde{a} = \kappa^+ \tilde{S}^+$. Since $\tilde{S}^+ = S^-(-t)^* = \kappa^{-*}a(-t)^* = \kappa^{-*}\tilde{a}(t)$, it follows $2\gamma_{rad} = \kappa^+ \kappa^{-*}$. Combining these results, we have:

$$\kappa^+ = \kappa^- = \kappa \tag{2.3}$$

$$|\kappa|^2 = 2\gamma_{rad} \tag{2.4}$$

In most of the case, a resonant mode can be excited through many different incident channels. These different channels include different polarizations, diffraction orders, and wave-vectors. The coupled mode theory can be generalized to include these different incident channels. In the following, we discuss, as an example, the case of a single resonator layer. The result from this specific case will be applied in the following discussion as well.

A layer of resonators can be excited by incident fields coming from either side, and its re-radiation goes into both directions. We denote the incident flux coming from the right and the left by S_R^+ and S_L^+, and the flux escaping to the right and the left by S_R^- and S_L^-. It is natural to adopt the plane wave basis for the external fields. In this case, $\left|S_{R(L)}^{\pm}\right|^2$ is defined as the poynting flux entering or escaping from one unit cell with area $A = L^2$, and is related to the electric field by $\left|S_{R(L)}^{\pm}\right|^2 = \frac{c}{8\pi}\left|E_{R(L)}^{\pm}\right|^2 L^2$ (with a factor of $1/2$ from averaging over time), where $E_{R(L)}^{\pm}$ is the electric field of the incoming or

9

outgoing waves. On the other hand, $|a|^2 = \frac{1}{16\pi}\int \frac{d(\omega\epsilon)}{d\omega}|E|^2 + \mu|H|^2]d^3r$ is the electromagnetic energy per unit cell. In the presence of two incident channels, Eqs. (2.1) and (2.2) can be generalized as:

$$\frac{d}{dt}a = (-i\,\omega_0 - \gamma)a + \kappa_R\,S_R^+ + \kappa_L S_L^+, \tag{2.5}$$

$$S_{R(L)}^- = S_{L(R)}^+ + \kappa_{R(L)}a. \tag{2.6}$$

The damping rate now includes radiative loss into both directions: $\gamma = \gamma_{ohm} + \gamma_{rad}^R + \gamma_{rad}^L$, where $2\,\gamma_{rad}^{R(L)} = |\kappa_{R(L)}|^2$ according to Eq. (2.4). We now consider the case when the incidence comes from the right, i.e., $S_L^+ = 0$. Solving Eq. (2.5) and (2.6), we obtain the reflectance, R, and the transmittance, T:

$$R = \left|\frac{S_R^-}{S_R^+}\right|^2 = \left|\frac{\kappa_R^2}{i\omega_0 - i\omega + \gamma}\right|^2 \tag{2.7}$$

$$T = \left|\frac{S_L^-}{S_R^+}\right|^2 = \left|1 + \frac{\kappa_L\,\kappa_R}{i\omega_0 - i\omega + \gamma}\right|^2 \tag{2.8}$$

In the case without the ohmic damping ($\gamma_{ohm} = 0$), energy conservation indicates $R + T = 1$. Substitute R and T from Eq. (2.7) and (2.8) into the equality, one finds the requirement that:

$$\kappa_R^* + \kappa_L = 0 \tag{2.9}$$

If the structure is symmetric with respect to the left and right, we can further express the radiative coupling coefficients as $\kappa_R = \kappa_L = i\,\kappa$. Equation (2.9) is valid even when the ohmic damping is present, as can be directly verified using the energy conservation law, $1 - |R|^2 - |T|^2 = 2\,\gamma_{ohm}\,|a/S_R^+|^2$, where the right hand side of the equality represents the ohmic loss.

2.3 INTERACTION BETWEEN TWO RESONANCES AND THE FANO INTERFERENCE

By introducing coupling through the electromagnetic interaction, two or more resonant modes can be coupled together. Using the framework of the coupled mode theory presented in Sec. 2.2, we consider a simple case of coupling between two resonant modes, while the resonators are arranged in a planar array. Generalizing the treatment to three or more resonant modes is straight forward. We denote the amplitude of the bright mode by a_B and the dark mode by a_D, and introduce the coupling coefficients, $g_{1(2)}$, to characterize their interaction. The equations of motion can therefore be written as:

$$\frac{d}{dt}a_B = (-i\omega_B - \gamma_B)a_B + g_1 a_D + i\kappa_B S^+,$$

$$\frac{d}{dt}a_D = (-i\omega_D - \gamma_D)a_D + g_2 a_B + i\kappa_D S^+, \qquad (2.10)$$

where $\omega_{B(D)}$ is the resonant frequency of the bright (dark) mode, and $\gamma_{B(D)} = \gamma_{B(D)}^{ohm} + \gamma_{B(D)}^{rad}$ is the damping rate. The radiative damping, $\gamma_{B(D)}^{rad}$, includes radiative loss into both sides of the array. On the other hand, $\kappa_{B(D)}$ is the coupling coefficient to the external field from only one side. It follows that their relation should be $\gamma_{B(D)}^{rad} = \left|\kappa_{B(D)}\right|^2$, with a difference in the factor of two comparing to Eq. (2.4). The factor of i in front of $\kappa_{B(D)}$ is because of the energy conservation consideration, as is explained in Sec. 2.2. The origin of the interaction, g_1 and g_2, can be either the mutual capacitance or the inductance between the two modes. There is a constrain between g_1 and g_2. Suppose that we have two modes with no damping and no coupling to external fields, but are coupled to each other. The conservation of the total energy over time, $\frac{d}{dt}(|a_B|^2 + |a_D|^2) = 0$, implies:

$$g_1 + g_2^* = 0. \qquad (2.11)$$

From the above relation between the coupling coefficients, and notice that the phase of g_1 or g_2 can be redefined without changing the coupled equations, we can denote the coupling coefficients by $g_1 = g_2 = ig$.

11

For the dark mode, we suppose that its far-field coupling coefficient, κ_D, is zero. Equation (2.3) can then be solved to give:

$$a_B = \frac{[i(\omega_D - \omega) + \gamma_D]}{[(i\omega_D - i\omega + \gamma_D)(i\omega_B - i\omega_B + \gamma_B) + |g|^2]} i\kappa_B S^+ ,$$

$$a_D = \frac{ig}{[(i\omega_D - i\omega + \gamma_D)(i\omega_B - i\omega + \gamma_B) + |g|^2]} i\kappa_B S^+ . \qquad (2.12)$$
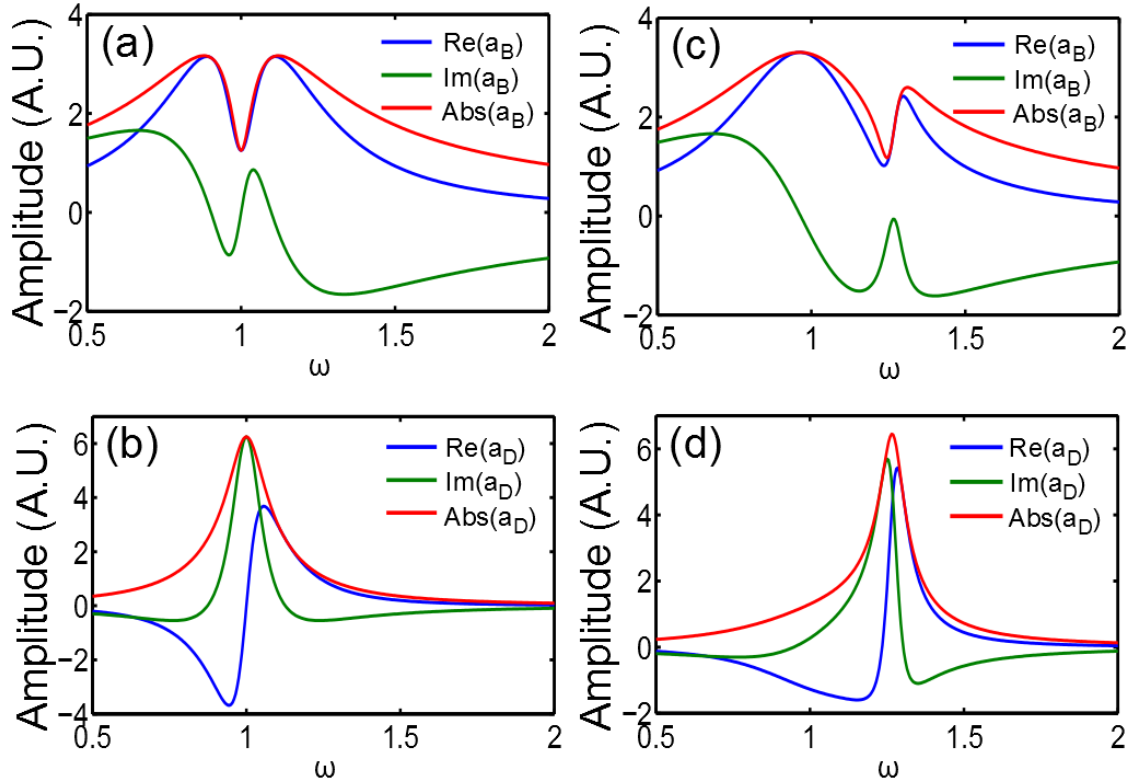
Figure 2.1: The amplitudes of both the bright(a_B) and the dark(a_D) modes when the Fano interference occurs. In (a) and (b), the dark mode resonant frequency matches to that of the bright mode ($\omega_B = \omega_D = 1$), resulting in the EIT. In (c) and (d), the bright mode has $\omega_B = 1$, while the dark mode has $\omega_D = 1.25$. The other parameters are given by $\gamma_B = 0.3$, $\gamma_B^R = 0.2$, $\gamma_D = 0.02$, and $g = 0.1$ for all the examples shown here.

The far-field re-emission, which is typically the reflection when considering a densely arranged array of plasmonic structures, is proportional to the amplitude of the bright

mode. According to Eq. (2.2) with $\eta = 0$ and the derivations leads to Eq. (2.7) and
(2.8), the reflection and the transmission are given by:

$$r = \frac{S^-}{S^+} = -\frac{\kappa_B^2 [i(\omega_D - \omega) + \gamma_D]}{[(i\omega_D - i\omega + \gamma_D)(i\omega_B - i\omega + \gamma_B) + |g|^2]} , \qquad (2.13)$$

$$t = 1 + r = 1 - \frac{\kappa_B^2 [i(\omega_D - \omega) + \gamma_D]}{[(i\omega_D - i\omega + \gamma_D)(i\omega_B - i\omega + \gamma_B) + |g|^2]} , \qquad (2.14)$$

and the absorbance, $A = 1 - |r|^2 - |t|^2$, is given by:

$$A = \frac{2\,\kappa_B^2}{D(\omega)} \{\gamma_B^{ohm}[(\omega - \omega_D)^2 + \gamma_D^2] + \gamma_D^{ohm}\,|g|^2\}$$

$$= 2\,\gamma_B^{ohm}|a_B/S^+|^2 + 2\,\gamma_D^{ohm}|a_D/S^+|^2. \qquad (2.15)$$

In the above equation, $D(\omega) = |(i\omega_D - i\omega + \gamma_D)(i\omega_B - i\omega + \gamma_B) + |g|^2|^2$, and

it is assumed that $\gamma_D^{rad} = 0$. The expression for the reflectivity shown by Eq. (2.13)

represents a typical Fano lineshape. In the case that the dark mode's resonant frequency

is matched to that of the bright mode, $\omega_B = \omega_D$, the reflectivity drops abruptly near the

dark mode resonance, as is shown in Fig. 2.1 (a). This is also referred to as the

electromagnetically induced transparency (EIT) in the plasmonic system [6, 7]. At the

EIT frequency, $\omega = \omega_B = \omega_D$, the amplitude of the bright mode is given by $a_B =$

$i\gamma_D\kappa_B S^+/[\gamma_D\gamma_B + |g|^2]$ according to Eq. (2.12). As the coupling between the bright

mode and the dark mode becomes large enough, $|g|^2 > \gamma_D\gamma_B$, the bright mode is

depolarized by the strongly excited dark mode at the EIT, and the medium appears

transparent to the incident field. When $\omega = \omega_B = \omega_D$, the ratio between the amplitudes

with $(g \neq 0)$ and without $(g = 0)$ the EIT is given by $\frac{\gamma_D\gamma_B}{[\gamma_D\gamma_B + |g|^2]} \ll 1$, assuming

$|g|^2 \gg \gamma_D\gamma_B$. As we discuss in the following, the group velocity of the incident field is

reduced and the electromagnetic energy is stored in the dark mode resonance.

In the case when the resonant frequencies of the two modes are mismatched

$(\omega_B \neq \omega_D)$, the Fano resonance results in an asymmetric lineshape, as is shown in Fig.

2.1 (c). When both the bright mode and the dark mode are passive $(g_1 g_2 < 0)$, the

linewidth of the hybridized dark mode is generally increased by coupling to the bright mode. If we expand the frequency near the vicinity of the dark mode resonance, $\omega = \omega_D + \delta$, and assumes that $|\delta| \ll |\omega_D - \omega_B|$, then the amplitude of the dark mode becomes:

$$a_D \approx -\frac{g}{i\omega_B - i\omega_D + \gamma_B} \kappa_B S^+ / \left[i\delta + \gamma_D + |g|^2 \frac{-i(\omega_B - \omega_D) + \gamma_B}{(\omega_B - \omega_D)^2 + \gamma_B^2} \right]. \qquad (2.14)$$

The above expression for the "dressed" dark mode is still a Lorenzian form, with the resonant frequency being shifted to $\omega' = \omega_D + \frac{|g|^2(\omega_D - \omega_B)}{(\omega_D - \omega_B)^2 + \gamma_B^2}$ and the decay rate being modified by $\gamma_D' = \gamma_D + \frac{|g|^2 \gamma_B}{(\omega_D - \omega_B)^2 + \gamma_B^2}$ [8]. The frequency shift can be understood as the result of the mutual repulsion between the dark mode and the bright mode, and therefore ω' is moving away from the bright mode resonant frequency, ω_B. On the other hand, the linewidth broadening can be interpreted as the combination of the initial dark mode decay rate and the additional decaying into the bright mode resonance.
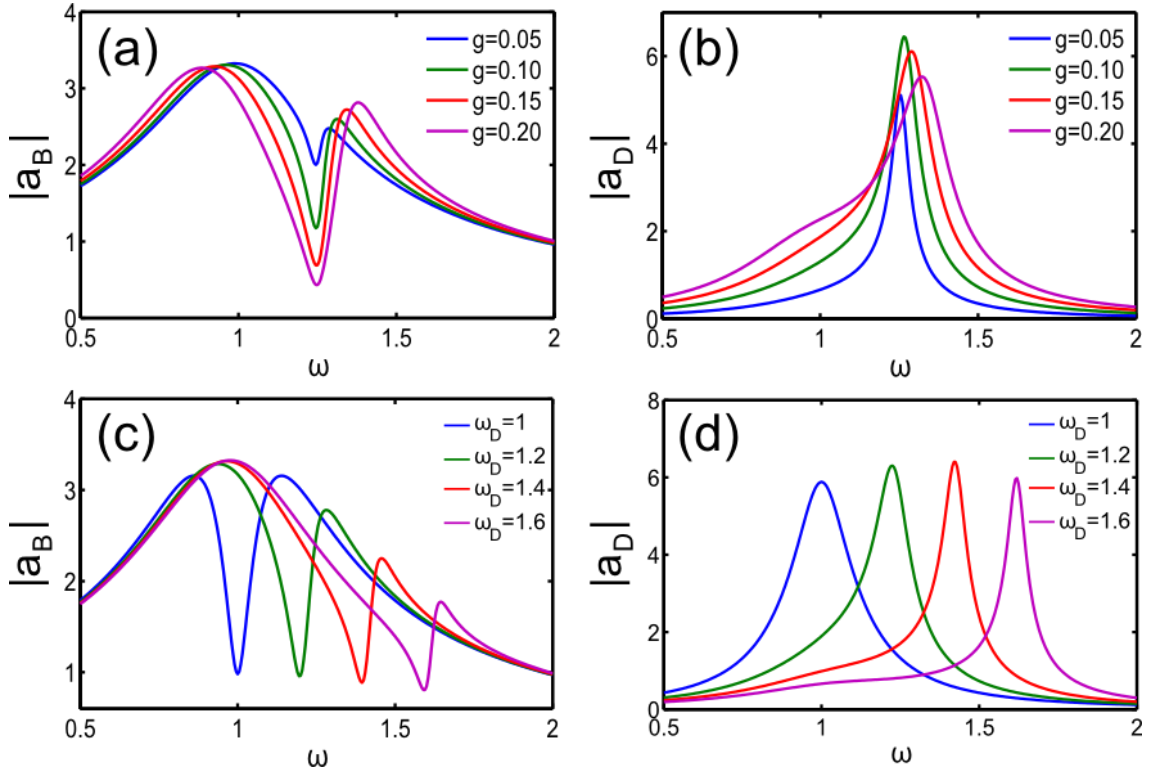
Figure 2.2: (a~b) Amplitude of the bright and the dark mode as the coupling coefficient is varied. (c~d)   Amplitude of the bright and the dark mode as the resonant frequency of the dark mode is detuned from the bright mode. The coefficients are given by $\omega_B = 1$, $\gamma_B = 0.3$, $\gamma_B^R = 0.2$, $\gamma_D = 0.02$. In (a) and (b), $\omega_D = 1.25$. In (c) and (d), $g = 0.12$.

From the expression for the resonant frequency and the decay rate of the dressed dark mode, it can be seen that the bandwidth of the Fano interference is not only determined by the coupling coefficient, g, but also depends on the frequency detuning, $\omega_D - \omega_B$, between the two modes. In general, the bandwidth of the Fano lineshape decreases with the increasing of the frequency detuning or the decreasing of the coupling coefficient, as is shown in Fig. 2.2. As we'll see in the following Chapters, the coupling coefficients can be adjusted by controlling the asymmetry of the plasmonic structure design (Chapter 3 and 4) or the physical separation between the two resonant objects that

host different resonant modes (Chapter 5), while the frequency detuning can be adjusted by simply scaling the resonant structures. Therefore, we generally have full control over the frequency as well as the bandwidth of the Fano resonance by manipulating the design of the plasmonic nanostructures.

2.4 THE SLOW LIGHT NEAR THE FANO RESONANCE

Near the Fano interference, the group velocity of the incident field is dramatically reduced and the electromagnetic energy is stored in the dark mode resonance. Here, we discuss qualitatively how the group velocity, v_g, depends on the linewidth of the resonators and the coupling coefficients. In order to do so, we assume the Fano resonant plasmonic structure can be described as a homogeneous medium with an effective permittivity, ϵ_{eff}, and permeability, μ_{eff}, as is illustrated in Fig. 2.3 (a). This assumption is valid when the structure is deeply subwavelength, i.e., the unit cell of the structure is much smaller than the incidence wavelength. Without any magnetic resonance associated with the structure, we keep $\mu_{eff} = 1$ in the following discussion.

We consider a single layer of the plasmonic resonators constituting a square array that has a periodicity of L, and the layer has a thickness of L as well. When a layer with a permittivity of ϵ is much thinner than the wavelength, $\ll \lambda_0/\sqrt{\epsilon}$, the reflection coefficient from such thin film is given by:

$$r = \frac{i}{2}k_0L(\epsilon - 1) = i\,2\pi\,k_0L\chi\,,\qquad(2.15)$$

where $k_0 = 2\pi/\lambda_0$ is the free space wavenumber and χ is the electric susceptibility in the Gaussian unit. The assumption of small L is consistent with the subwavelength size of the unit cell that are required for homogenizing the effective medium. By comparing

the reflection coefficient with Eq. (2.13), one finds that the susceptibility can be represented by:

$$\chi = \frac{\kappa_B a_B / S^+}{2 \pi k_0 L} \, ,$$ (2.16)

and so the effective permittivity of the resonator array is:

$$\epsilon_{eff} = 1 + 4 \pi \chi = 1 + \frac{2i}{k_0 L} \frac{(i\omega_D - i\omega + \gamma_D)\gamma_B^R}{(i\omega_D - i\omega + \gamma_D)(i\omega_B - i\omega + \gamma_B) + g^2} \, .$$ (2.17)

With the dispersion, $k(\omega) = \sqrt{\epsilon_{eff}(\omega)}\,\omega/c$, obtained from Eq. (2.10), we can calculate the group index inside such effective medium according to:

$$n_g = c \frac{dk}{d\omega} = \left(n + \omega \frac{dn}{d\omega} \right) \, ,$$ (2.18)

where $n = \sqrt{\epsilon_{eff}}$ is the effective optical index in the medium. In Fig. 2.3 (b) and (c), we show both the effective permittivity, ϵ_{eff}, and the group index, n_g, with several different coupling constants between the dark mode and the bright mode.
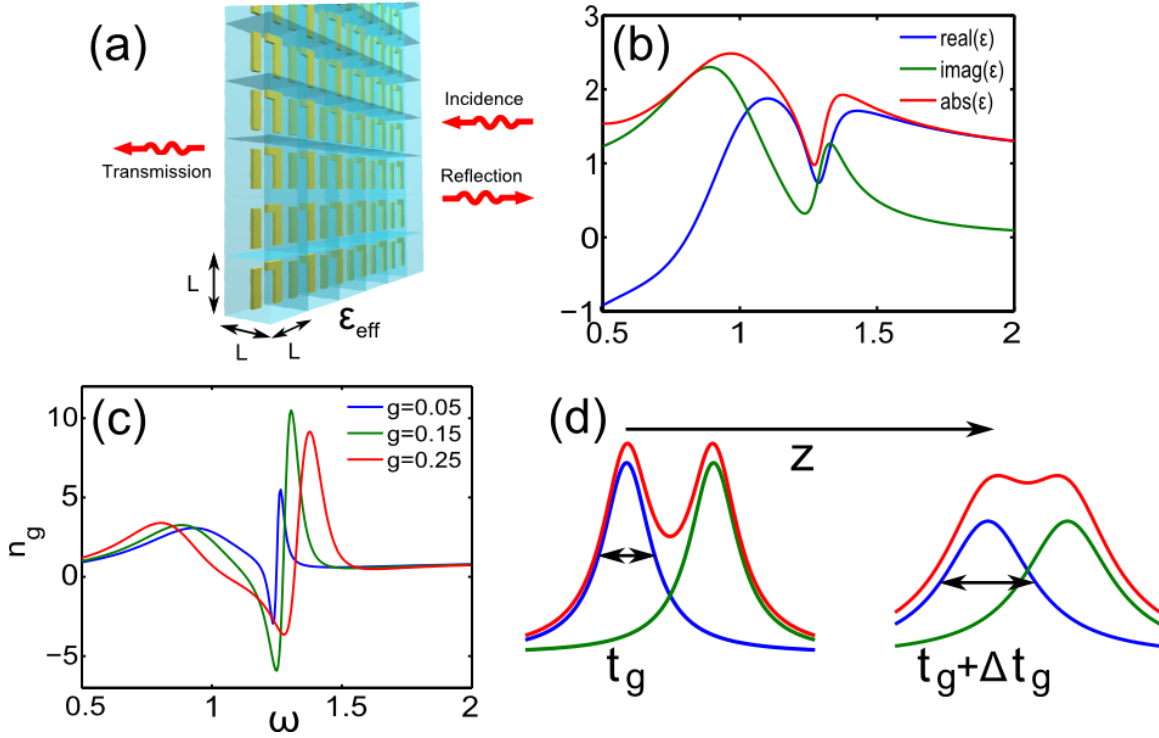
Figure 2.3: (a) A schematic of a Fano-resonant planar array illuminated by an incident wave. The array is described as an effective medium with a permittivity ϵ_{eff} and a thickness of L. (b) An example of the permittivity of the Fano resonant array. $\omega_B = 1$, $\omega_D = 1.25$, $\gamma_B = 0.3$, $\gamma_B^R = 0.2$, $\gamma_D = 0.02$, and $g = 0.15$. (c) The group index calculated from ϵ_{eff} of the medium. The parameters are the same as in (b), except that g is specified by the legend. (d) An illustration of the pulse broadening effect due to the GVD. The pulse 1 is represented by the blue, the pulse 2 is represented by the green, and the red is their superposition. The duration of the pulses increase from t_g to $t_g + \Delta t_g$ after traveling over a distance z, making two originally distinct pulses inseparable.

Although the plasmonic Fano interference is capable of inducing very high group indices, its application in the signal processing and telecommunication is still limited for the following two reasons: (1) the narrow linewidth necessary for inducing the high group index limits the bandwidth of the transmitted pulses, and (2) the strong group

velocity dispersion (GVD), $D = d^2k(\omega)/d\omega^2$, results in pulse broadening when propagating. Both factors place a limitation on the maximum useable bit rate. The former restricted the shortest pulse duration, t_b, that can be slowed down, and so the bit rate is limited by $f_b = \frac{1}{t_b} < \Delta\omega/2\pi$. On the other hand, the signal pulses deform and broaden along the propagation direction due to the GVD, which makes two originally separate signals overlap with each other, as is illustrated in Fig. 2.4 (d). Suppose that a pulse travels by a distance z, the excess time spread of the pulse duration will be $\Delta t_g = Dz\Delta\omega$, where $\Delta\omega$ is the bandwidth of the pulse. Therefore, in order to have separable pulses, the bit rate must be limited by $f_b < 1/(Dz\Delta\omega)$ [9].

Both of the aforementioned limitations appear to be intrinsic to the Fano interference because they originate from the strong dispersion property. Nevertheless, we will show in the following Chapter a schematic that can lift both limitations. By introducing two Fano interferences in a specific way, one can construct a Fano resonant medium that can possess large group index and small GVD over a broad frequency range.

2.5   CONCLUSION

In this Chapter, we provide a general picture of the plasmonic Fano interference by using the coupled mode theory. With present nano-fabrication techniques, the plasmonic structures can be designed and fabricated to exhibit the Fano resonances at frequencies ranging from near-IR to THz.   The strong dispersion induced by the Fano interference results in the slow light and strong light-matter interactions. We will show in the following Chapters some of the specific plasmonic structure designs that demonstrate the Fano resonances, as well as their exciting applications including optical information

processing and storage, biomolecule detection and characterization, diffraction-unlimited

image, energy harvesting and so on.

Chapter 3

Low Symmetry Metamaterials Exhibiting the Double-Continuum Fano Resonance

3.1 INTRODUCTION

The ability to slow down light to low group velocities v_g compared with the vacuum light speed c while maintaining high coupling efficiency [10] is one of the most dramatic manifestations of controlled light manipulation in optics. Apart from its fundamental significance, it has long-reaching technological applications [11], including enhanced nonlinear effects due to the energy density compression by as much as c/v_g; pulse delay and storage for optical information processing [12]; optical switching, and quantum optics. Most approaches to obtaining SL rely on the phenomenon of Electromagnetically Induced Transparency (EIT) [13]. EIT and its analogs have been demonstrated in several media, including cold [10], warm atomic gases [14], and even plasmas [15, 16].

More recently, in response to the emerging applications such as bio-sensing, an increasing attention has shifted towards obtaining EIT using electromagnetic metamaterials [7, 17, 6]. Metamaterials enable engineering electromagnetic resonances with almost arbitrary frequencies and spatial symmetries. For example, the EIT phenomenon has been emulated in metamaterials [7, 17, 6] possessing two types of resonances: a "dark" one, which is not directly coupled to the incident electromagnetic field, and a "bright" one, which is strongly coupled to the incident field. If the respective frequencies of these resonances, ω_Q and ω_R, are very close to each other, they can become strongly coupled by a slight break of the metamaterial's symmetry.

21

3.2   THE BROADBAND SLOW LIGHT

The most serious limitation of the EIT-based SL (EIT-SL) stems from the desirability of achieving the SL over a broad spectral range, especially for optical buffering of ultra-short pulses. Increasing coupling between the bright and dark resonances broadens the spectral range, yet comes at the expense of increasing both the group velocity, v_g, and group-velocity dispersion, $dv_g^{-1}/d\omega$. Qualitatively, the bandwidth limitation of the EIT-SL arises because the flatness of the EIT transmission band (which is necessary for small $d\omega/dk_z$, where ω and k_z are, respectively, the frequency and the wavenumber of the propagating radiation) originates from the finite spectral width $2\Delta\omega$ of the EIT band. Therefore, only the light inside the $\omega_0 - \Delta\omega < \omega < \omega_0 + \Delta\omega$ bandwidth can be slowed down. Using metamaterials with spatially-dependent $\omega_0(z)$ along the propagation direction, z, can potentially increase the total propagation bandwidth of the EIT-SL [17]. However, the EIT band is surrounded by the stop bands, as illustrated below, which block the broadband transmission. Therefore, a natural solution to the bandwidth problem is to design a metamaterial supporting a propagating mode which is *spectrally broad, yet possesses a "flat" segment* with $\frac{\partial \omega}{\partial k_z} \ll c$, as is schematically shown in Fig. 3.1.
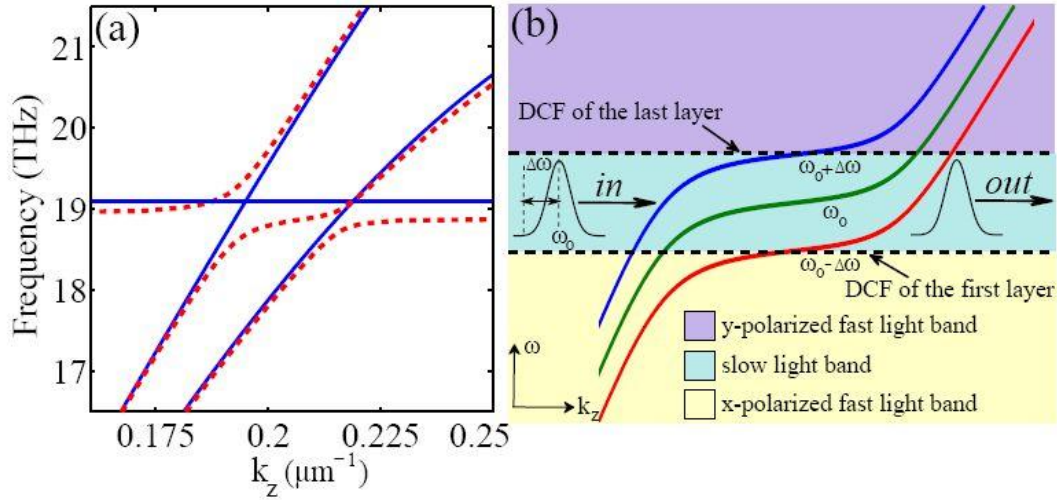
Figure 3.1: (a) Band structure of DCF metamaterial as predicted by the analytical model of coupled oscillators [see Eqs. (1, 2)]. Different line styles correspond to the reduction of the spatial symmetry of a metamaterial: from two mirror-symmetry planes (solid) to none (dashed). (b) Broad-band SL: the medium is comprised of multiple layers of DCF metamaterials with spatially-varying resonance frequency Ω_Q in the $\omega_0 - \Delta\omega < \Omega_Q < \omega_0 + \Delta\omega$ range. The incoming light undergoes polarization transformation and is slowed down.

In this Chapter we discuss a new approach to producing SL which relies on the phenomenon of Double-Continuum Fano (DCF) optical resonance. The Fano resonance is typically observed when resonators are coupled with one or several continua and can be described as an interference of the resonant and non-resonant scattering pathways giving rise to characteristic asymmetric shape of the spectra [18, 19]. In the DCF scenario a single discreet state ("dark" mode) is coupled to two sets of continuum states (two propagating modes of different polarization states). If the frequency of the "dark" mode is embedded in the frequency continua of the propagating modes, a simple symmetry breaking couples all three modes. The result of such coupling is a very unusual propagation band [see Fig. 3.1 (a) and 3.2 (a)] which fulfills the above requirement for

23

broadband SL applications by continuing from one propagating mode to another, with the SL region in between. We demonstrate that multiple layers of such DCF metamaterial with adiabatically changing frequency of the "dark" mode [as illustrated in Fig. 3.1 (b)] give rise to broadband SL with spectrally uniform group velocity and transmission. Unlike the more commonly known single-continuum Fano resonance [19, 20] that can be observed with highly symmetric molecules, DCF resonance requires low spatial symmetry molecules that are not reflection-symmetric with respect to any plane passing through the direction of light propagation.

3.3   THE COUPLED MODE THEORY ANALYSIS OF THE DCF

Before introducing a specific metamaterial realization, we apply the coupled mode theory discussed in Chapter 2 to consider a very general case of a DCF medium comprised of anisotropic molecules containing two "bright" transitions (characterized by the oscillator strengths q_x and q_y, respectively), which are coupled to the two perpendicular light polarizations, and one "dark" transition (characterized by the oscillator strength, Q), which is decoupled from the far-field. The equations of motion for the coupled oscillator strengths q_x, q_y, and Q excited by the light with the electric field components E_x and E_y are:

$$\ddot{q}_x + \Omega_{Rx}^2\, q_x + \kappa_{xy} q_y + \kappa_{xQ} Q = a\alpha_x E_x e^{i\omega t},$$

$$\ddot{q}_y + \Omega_{Ry}^2\, q_y + \kappa_{xy} q_x + \kappa_{yQ} Q = a\alpha_y E_y e^{i\omega t},$$

$$\ddot{Q} + \Omega_Q^2 Q + \kappa_{xQ} q_x + \kappa_{yQ} q_y = 0, \qquad (3.1)$$

where $\Omega_{Rx/\,Ry/\,Q}$ are the resonant frequencies of the transitions and $\kappa_{xy/\,xQ/\,yQ}$ are the coupling coefficients between them. q_x and q_y are coupled to external fields through the coupling constants $a\,\alpha_x$ and $a\,\alpha_y$, where a is a constant with a dimension of ω^2,

and $\alpha_{x/y}$ are the depolarization factors such that the dipole moment (normalized to one molecule's volume V_0) is $p_{x/y} = \alpha_{x/y} q_{x/y}$. On the other hand, the dark state, Q, cannot be directly excited by the electric field, nor does it directly contribute to the polarizability of the medium. It therefore plays the role of the discrete Fano state. Solving for q_x and q_y in the form of $q_i = b_{ij} E_j$ (where $i = x, y$), we can construct the dielectric permittivity tensor $\hat{\epsilon} = \hat{1} + 4\pi \hat{\chi}$, where $\hat{\chi} = (N_0 V_0)\hat{a}\,\hat{b}$, $\hat{a} =$ diag$[\alpha_x, \alpha_y]$, and N_0 is the molecular density. The effective polarizability of the DCF medium is given by:

$$\chi_{xx} = N_0 a \alpha_x^2 (W_{Ry} W_Q - \kappa_{yQ}^2)/D ,$$

$$\chi_{yy} = N_0 a \alpha_y^2 (W_{Rx} W_Q - \kappa_{xQ}^2)/D ,$$

$$\chi_{xy} = \chi_{yx} = -N_0 a \alpha_x \alpha_y (\kappa_{xy} W_Q - \kappa_{xQ}\kappa_{yQ})/D , \qquad (3.2)$$

where $D = W_{Rx} W_{Ry} W_Q - \kappa_{xQ}^2 W_{Ry} - \kappa_{yQ}^2 W_{Rx} - \kappa_{xy}^2 W_Q - 2 \kappa_{xQ} \kappa_{yQ} \kappa_{xy}$ is the determinant of the matrix formed by the l.h.s of Eq. (3.1), and $W_i = (\Omega_i^2 - \omega^2)$. Photonic band structure (PBS) is analytically calculated from the eigenvalue equation for $k_z(\omega)$: $det(k_z^2 \delta_{ij} - \epsilon_{ij}\omega^2/c^2) = 0$, which directly follows from the Maxwell's equations. Unlike the EIT case where the dark mode's frequency needs to be matched to that of the x-dipole resonance [7, 6], the DCF occurs under the following conditions: (i) $\Omega_Q < \Omega_{Rx}, \Omega_{Ry}$, and (ii) at least 2 of the 3 coupling constants (κ_{xQ}, κ_{yQ}, and κ_{xy}) are non-vanishing. Without significant loss of generality, and with an eye on the specific metamaterial implementation (see schematic in Fig. 3.2), we have neglected the direct coupling between q_x and Q. Finite values of the κ's is the consequence of the reduced spatial symmetry of the anisotropic molecule. For example, $\kappa_{xy} = 0$ would be either accidental, or due to the high spatial symmetry of the molecule (e.g., y-z mirror symmetry). Figure 1 (a) shows the PBS in the DCF medium (dashed line) calculated from the analytical model using the following parameters: $[\Omega_{Rx}, \Omega_{Ry}, \Omega_Q] = [27, 23.85, 19.1]$ THz, $[\kappa_{xQ}, \kappa_{yQ}, \kappa_{xy}] = [50, 0, 50]$ THz ^{2}, $\alpha_x = 1$, $\alpha_y = 1.65$, $a =$

25

529 THz ^{2}, and $N_0 V_0 = 10^{-3}$. The unusual PBS in the DCF medium can be understood through its evolution from that in the medium comprised of the symmetric molecules ($\kappa_{xQ} = 0$, $\kappa_{xy} = 0$) [solid lines in Fig. 3.1 (a)]. First, the $\kappa_{xQ} \neq 0$ coupling hybridizes the x-dipole and the quadrupole resonances and creates an avoided crossing between the x-polarized propagation band and the discrete "dark" mode. The second avoided crossing between the y-polarized propagation band and the discrete "dark" mode occurs owing to $\kappa_{xy} \neq 0$. Thus, the DCF medium comprised of the low-symmetry molecules supports a propagation band that smoothly connects the two orthogonally polarized continua by passing through the SL region near the "dark" mode's frequency, Ω_Q. Such PBS has the following advantages over that in the EIT medium: (i) the dark mode frequency has more tunability because it is only required to be embedded inside the continuous bands, and (ii) there are no bandgaps on either side of the SL region. These features of the SL band are necessary for realizing the broadband SL using the approach of adiabatically-varying material parameters [specifically, $\Omega_Q(z)$] schematically shown in Fig. 3.1 (b).
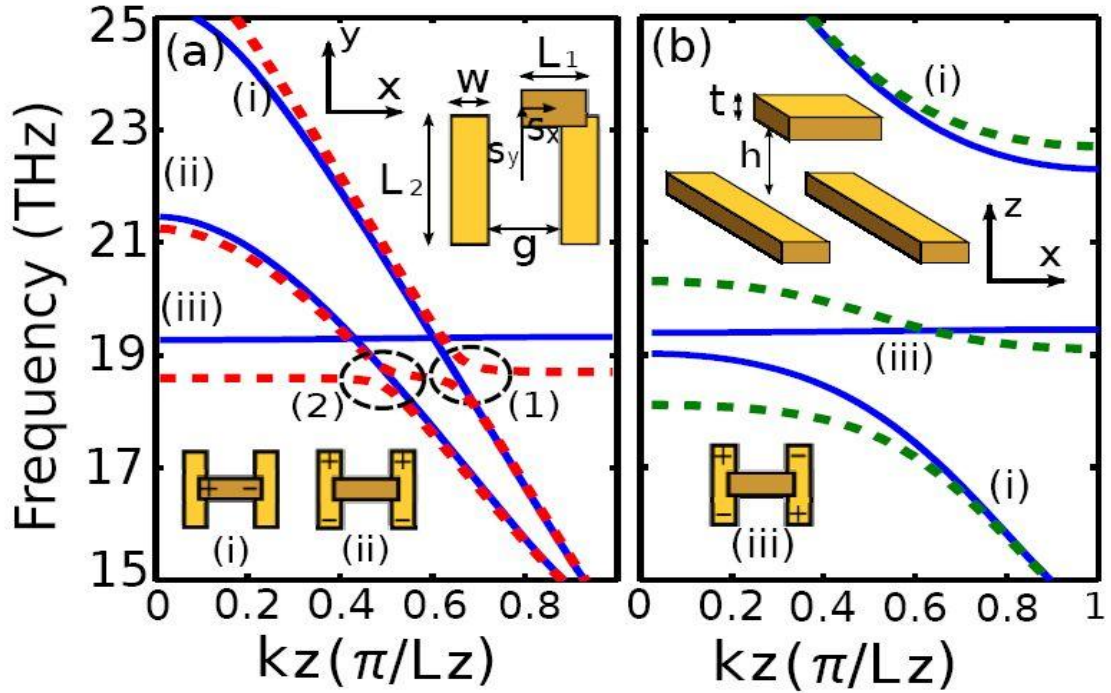
Figure 3.2: PBS for SL metamaterials based on the DCF resonance (a) and on the EIT (b). The insets show the geometry and dimensions of the unit cell and the three supported resonances: (i) horizontal dipole, (ii) vertical dipole, and (iii) the quadrupole. Solid lines: PBS computed for a symmetric unit cell ($s_x = 0$ and $s_y = 0$). (a) Propagation bands for DCF-based metamaterial (dashed lines): $s_x = 700$ nm, $s_y = 2$ μm, $L_1 = 2$ μm. The avoided crossings marked (1) and (2) are caused by $s_y \neq 0$ and $s_y \neq 0$, respectively. Flat portion of the spectrally-extended middle band: SL. (b) Propagation bands for the EIT-based metamaterials (dashed lines) with partial symmetry breaking ($s_x = 0$ nm, $s_y = 500$ nm, $L_1 = 3.8$ μm): emergence of SL for the spectrally-narrow middle band. For (a) and (b): $t = 400$ nm, $h = 400$ nm, $L_2 = 4$ μm, $w = 800$ nm, $g = 2.2$ μm. The metamaterial's periodicities are $6\,\mu m \times 7\,\mu m \times 7\,\mu m$, and the electromagnetic waves are assumed to propagate in the z direction.

3.4 THE LOW-SYMMETRY METAMATERIALS

Both DCF and EIT metamaterials supporting the propagation of slow light can be implemented using a three-dimensional periodic arrangement of the unit cells comprised of three metallic antennas. Such unit cell shown in Fig. 3.2 consists of two vertical and one horizontal metallic antennae embedded in a dielectric medium with n=1.5. It is reminiscent of the ones used for single-layer EIT metamaterials [7, 6], except that both s_x and s_y are allowed to be non-vanishing, thereby dispensing with all reflection symmetries of the unit cell. The two vertical antennas support a bright dipole and a dark quadrupole resonances, while the single horizontal antenna supports another bright resonance. Coupling between all three resonances is induced by breaking the reflection symmetries of the structure. For example, within the general model described by Eqs. (3.1), $s_y \neq 0$ results in $\kappa_{xQ} \neq 0$, while $s_x \neq 0$ results in $\kappa_{xy} \neq 0$. The PBS, calculated using the finite-elements software COMSOL, is shown in Fig. 3.2 (a) and (b) for different geometric parameters of the unit cell. For example, by approximately matching Ω_{Rx} and Ω_Q (this is done by choosing the appropriate length, L_1, of the horizontal antenna) and selecting $s_x = 0$, $s_y \neq 0$, an EIT-SL band is obtained as indicated by the middle dashed line in Fig. 3.2 (b) (the y-polarized bands are not shown). Note that the EIT-SL band is surrounded by the two stop-bands. On the other hand, when (i) $s_x \neq 0$, and (ii) the dark mode of the fully-symmetric structure ($s_x = s_y = 0$) intersects the two propagation continua (the dispersive solid lines in Fig. 3.2 (a)), a DCF-SL band emerges as shown in Fig. 3.2 (a) (the dashed lines). The difference between the DCF bands in Figs. 3.1 (a) and 3.2 (a) is caused by the band-folding owing to the periodic nature of the metamaterial in the z-direction.

28

While it is apparent from the group velocity shown by the PBS that light can be significantly delayed by either the EIT or the DCF-based metamaterials, the spectral width of such SL band is quite limited in both cases. To create a broadband SL, we propose a multi-layered structure with each layer having its DCF's resonance frequency, Ω_Q, adiabatically varied along the propagation direction z. In the metamaterial structure shown in Fig. 3.2, such tuning can be achieved, for example, by changing the length of the two parallel antennae. Because the SL mode in the DCF-based metamaterial contains no band gaps, the adiabatic process smoothly converts one fast mode (e.g., x-polarized) into the hybrid slow mode, and then into another fast mode (y-polarized) without generating significant reflection. Such conversion is not possible for EIT-SL because the SL band is surrounded by the stop bands which lead to reflection of the SL as was recently demonstrated [21, 22]. Specifically, we consider a broadband x-polarized pulse with the central frequency, ω_0, and bandwidth, $\Delta\omega$, incident upon an N-layer metamaterial structure with adiabatically varying resonant frequencies, $\Omega_Q^{(1)} < \Omega_Q^{(j)} < \Omega_Q^{(N)}$ (where j is the metamaterial's layer number), as shown in Fig. 3.1 (b). It is further assumed that, while $\Delta\omega$ is much larger than the spectral width of the SL portion of any individual layer, the following relations are satisfied: $\Omega_Q^{(1)} < \omega_0 - \Delta\omega$ and $\omega_0 + \Delta\omega < \Omega_Q^{(N)}$. As the pulse passes through the structure, each frequency component, ω, is slowed down inside its corresponding layer, j, satisfying $\Omega_Q^{(j)} \approx \omega$ while propagating with no significant delay through the other layers. The light pulse is also gradually converted from x- into y-polarized. Because all the frequency components of the pulse undergo the same adiabatic transition, the entire pulse is slowed down uniformly with no group velocity dispersion.
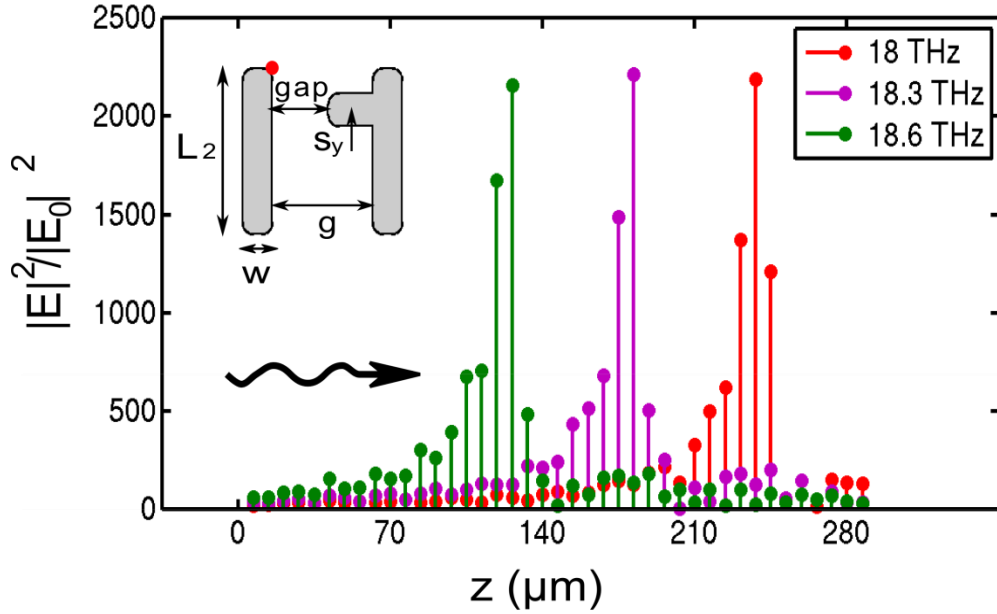
Figure 3.3: Field enhancements of four different frequency components propagating in an adiabatically varying DCF-based metamaterial. Inset: single-layer unit cell. Spectral position of the SL is adiabatically varied: $L_2 = 3.75 + z/700$ (μm). Field intensity is calculated at the red spot shown in the inset. Other parameters: $s_y = L_2/4$, $w = t = 0.8\,\mu$m, $g = 2.7\,\mu$m, and gap = 1.7 μm.

COMSOL simulations of a N=41-layer DCF-SL metamaterial, with the single-layer unit cell shown in the inset to Fig. 3.3, were performed. Note that this unit cell was modified from the one shown in Fig. 3.2 in order to decrease Ohmic losses. Antennas are assumed to be made of silver with the dielectric permittivity described by the Drude model [23]. The structure is triply-periodic with the period $L = 7\,\mu$m and embedded in a dielectric with an index of n=1.5. The SL's frequency is adiabatically varied from layer to layer by increasing L_2 from $3.75\,\mu$m to $4.15\,\mu$m. Other parameters are given in the caption of Fig. 3.3. Field intensity enhancement for three different frequencies is plotted

in Fig. 3.3, which indicates that different frequencies are slowed down inside different layers. Thus, light is slowed down over the entire spectral band $\Omega_Q^{(1)} < \omega < \Omega_Q^{(N)}$.

3.5 COMPARISON BETWEEN THE DCF AND THE EIT

To underscore the advantages of the DCF-based approach to broadband SL, we compare a multilayer DCF-SL structure (unit cell is shown in Fig. 3.3) with its EIT-based counterpart (unit cell is shown in Fig. 3.2, geometric parameters are given in the caption to Fig. 3.4). Both structures are based on silver antennas embedded in a dielectric with n=1.5. Figure 4 (a) and (b) show the simulation results for DCF-SL and EIT-SL structures, respectively. The group velocity is calculated as $v_g = L\, d\omega/d\phi$, where L is the total length of the structure and ϕ is the phase difference between incident and transmitted waves. In the case of EIT, the bandwidth can be potentially increased by increasing the coupling between dipole mode and quadrupole mode (κ_{xQ}). However, it comes at the expense of the increased group velocity dispersion and transmission non-uniformity. Specifically, both v_g and transmittance $|T|^2$ increase in the middle of the EIT band while remaining small near the EIT band edge. In contrast, the adiabatic DCF layers provide uniform group velocity as well as uniform cross-polarized transmittance inside the SL band. The bandwidth can be increased further simply by adding more adiabatically-varying layers. Note that the group velocity in the DCF-SL structure plotted in Fig. 3.4 (a) is averaged over N=41 layers. Therefore by adding more layers the group velocity averaged over all the layers is increasing. Nevertheless, inside the specific resonant layer, the group velocity of the corresponding frequency component is less than $0.01c$. The spectrally-flat transmission and absorption of the DCF-based metamaterial is appealing to a variety of applications including nonlinear optics and sensing. Moreover,

31

because every frequency component is dramatically slowed down in a well-defined layer, applications to spectrally-selective active light manipulation can be envisioned.
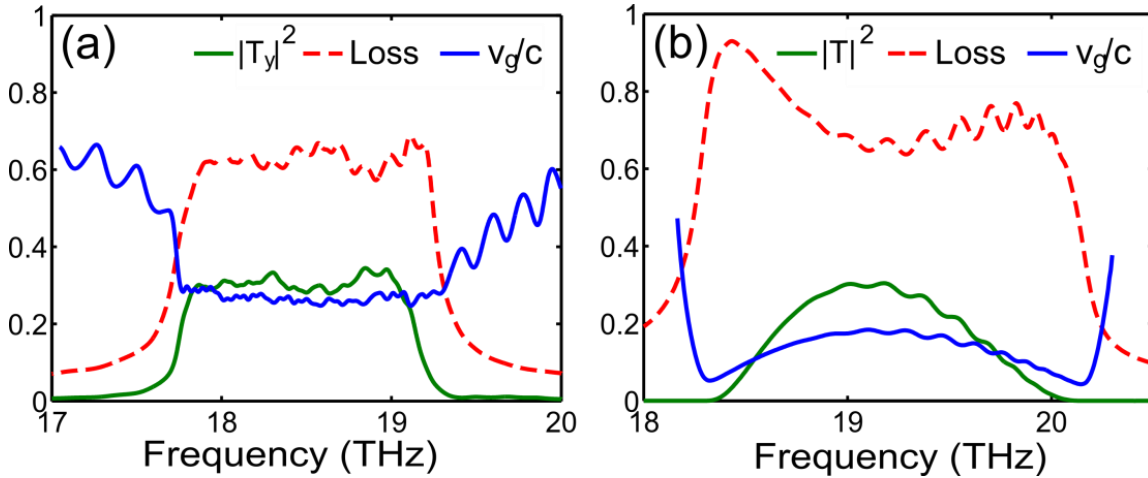
Figure 3.4: Transmission (solid green lines), absorption (dashed red lines), and group velocity (solid blue lines) of (a) adiabatic DCF-based and (b) EIT-based meta-materials. x-polarized incident light is assumed. Parameters of the DCF-based metamaterial: the same as in Fig. 3.3. EIT-based metamaterial is made of 20 identical   layers shown in Fig. 3.2, with the parameters $L_2 = 4\,\mu m$, $L_1 = 3.8\,\mu m$, $w = t = 0.8\,\mu m$, g = 2.7 μm, h = 0.9 μm, $s_y = 0.6\,\mu m$, and periodicity $L_x = L_y = L_z = 7\,\mu m$.

In Fig. 3.5, we compared the bandwidth delay product (BDP) per layer, which is defined as $D = \int \delta t(\omega)d\omega/N$, between the DCF and the EIT cases. Here, N is the number of metamaterial layers, and the delay time is defined as $\delta t = L/v_g - nL/c$, where L is the total thickness, v_g is the group velocity, n is the index of the environment, and c is the speed of light in vacuum. We define the bandwidth of EIT by the frequencies at which the group velocities reduce to 0.8 of the maximum value in the EIT band, i.e., the frequency range with $v_g > 0.14\,c$. The definition is based on two

reasons: first, the transmittance near the edges of the EIT band drops to zero as is shown in Fig. 3.4 (b), and therefore is not suitable for slowing down light, even though the group velocity is small. Second, large group velocity dispersion near the EIT band edge can result in distortion of the transmitted signal. Therefore, we choose the frequency range in which deviation from the center group velocity is within 20% as a reasonable bandwidth. The bandwidth of DCF is defined in the same way. Finally we divide the bandwidth delay product by the number of layers of either EIT or DCF structures, because in both cases the product is proportional to the propagation length. Figure 5 (a) shows the comparison of the BDP per layer between the DCF (the red dashed line) and the EIT (the blue circles) cases, respectively. We pick the EIT structures with several different s_y (displacement of the horizontal antenna in the y-direction), and therefore different bandwidths, to compare with the adiabatically varying DCF structure shown in Fig. 3.3 and 3.4. Figure 3.5 (b) shows the bandwidth for both the DCF and the EIT cases. It can be seen that in small s_y cases, the EIT has larger BDP than the DCF, but the bandwidth is narrower. On the other hand, the bandwidth of EIT can be increased by increasing s_y, but at the cost of reducing the BDP. In specific, when the bandwidth of the EIT structure reaches that of the DCF structure, the BDP for the DCF is 50% more than the BDP for the EIT. Thus, the DCF structure is advantageous compared to the EIT structure for broad band slow light applications.
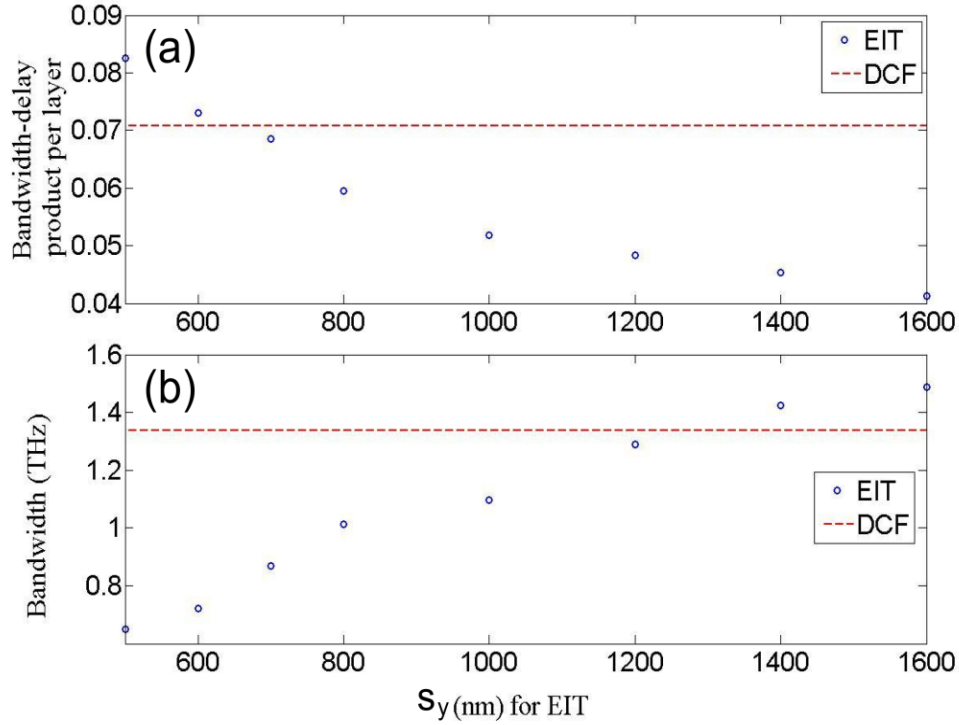
Figure 3.5: (a) The bandwidth-delay product for the DCF (the red dashed line) and the EIT (the blue circles) cases. The geometry of the adiabatically varying DCF layers is defined in the caption of Fig. 3.3, with L_2 increases from 3.75 μm to 4.15 μm. The geometry of the EIT structure is defined in the caption of Fig. 3.4. The EIT structure has identical S_y for all layers, and is indicated by the x axis. (b) The slow light bandwidth for the DCF and the EIT cases.

3.6   SUMMARY

In conclusion, we have proposed a new mechanism of slowing down light over a spectrally broad band by means of low-symmetry metamaterials exhibiting double-continuum Fano (DCF) resonance. This approach is conceptually different from the more common EIT-SL. It is shown that DCF-based broadband slow light with uniform group velocity and transmittance can be achieved by adiabatically changing the DCF resonance frequencies along the light propagation direction. Spectrally-flat light absorbers and

filters, as well as various nonlinear devices requiring extreme light concentration are enabled by DCF-based slow-light metamaterials.

Chapter 4

Single Layer Biomolecules Detection Using Fano-Resonant Asymmetric Meta-Materials

4.1 INTRODUCTION

Engineered optical metamaterials present a unique platform for biosensing applications owing to their ability to confine light to nanoscale regions and to their spectral selectivity. Infrared plasmonic metamaterials are especially attractive because their resonant response can be accurately tuned to that of the vibrational modes of the target bio-molecules. Here we introduce a novel infrared plasmonic surface based on Fano-resonant asymmetric metamaterial (FRAMM) exhibiting sharp resonances caused by the interference between sub-radiant and super-radiant plasmonic resonances. Owing to metamaterial's asymmetry, the frequency of the sub-radiant resonance can be precisely determined and matched to the molecule's vibrational fingerprints. A multi-pixel array of FRAMMs is used as a platform for multi-spectral biosensing of nanometer-scale monolayers of recognition proteins and their surface orientation, as well as for detecting chemical binding of target antibodies to recognition proteins.

In-depth understanding of life-sustaining biomolecular binding processes has the potential for impacting every corner of life sciences and medicine [24, 25]. In general, conformational rearrangements in biomolecular structures are required for matching of the binding sites between the host-guest molecules [26, 27]. However, the state-of-art biosensing techniques can only probe the biomaterial accumulations due to molecular bindings [28, 29, 30], but not the underlying conformational alterations required for binding processes to occur [31]. While surface-enhanced Raman and infrared absorption spectroscopies [32, 33, 34, 35, 36] can provide the vibrational signatures of the conformational states of the molecules structure [37, 38, 39], these spectroscopic

approaches are not directly compatible with "gold standard" biosensing techniques [29] due to fundamentally different working principles. Here we introduce a novel *structure-resolving label-free biosensing* technique based on plasmonic Fano-Resonant Asymmetric Metamaterials (FRAMMs) that addresses this structure-function challenge by simultaneously probing structural and binding characteristics of biomolecular interactions using the full information content of the frequency-dependent infrared response of the bio-molecules.

Plasmonic metamaterials are engineered artificial media with tailored electromagnetic response over a broad range of frequencies: from visible to THz. Their optical properties go beyond those achievable using naturally-occurring optical materials, exhibiting a number of exotic phenomena which include negative refractive index, strong chirality, and indefinite electric permittivity [40, 41, 42, 43, 44]. Metamaterials manifesting these unusual optical properties are typically comprised of highly-resonant plasmonic elements (e.g., split-ring resonators) which have a spectrally-narrow response and high local field concentration. Owing to these properties, plasmonic metamaterials and single meta-molecules have recently emerged as a powerful photonic platform for sensing applications [45, 46, 47, 48, 34] and have been used for linear and nonlinear surface-enhanced spectroscopies [32 , 34, 35]. Especially important for biosensing applications are infrared metamaterials because bio-molecules possess mid-infrared vibrational fingerprints that can be used for their identification, thereby improving specificity of bio-detection [49].

While the concept of tuning metamaterial resonances to specific vibrational lines of a bio-molecule is straightforward [36], its actual implementation is complicated by dense spectral spacing of infrared-active vibrations. For example, selectively tuning resonant metamaterials to the commonly used amide vibrations of the protein backbone

(Amide-I at $\omega_I = 1620 - 1680 cm^{-1}$ and Amide-II at $\omega_{II} = 1510 - 1580 cm^{-1}$) requires the structures' quality factors $q \sim 10$. Even narrower resonances may be required to resolve the secondary structure of the proteins. Such sharp resonant lines are difficult to obtain with most plasmonic metamaterials despite relatively low Ohmic losses at infrared frequencies [34, 36]. Narrow linewidth is also requisite for obtaining large field enhancements over the surface of a planar plasmonic meta-molecule. For example, a half-wave antenna provides neither strong field enhancement nor spectrally-narrow response. By arranging meta-molecules into periodic arrays, it is possible to suppress radiative decay and boost field enhancement due to the formation of collective high quality resonances [50]. The drawback of such coherent metamaterials [34, 51] is their reliance on long-range interactions between unit cells, making their performance sensitive to fabrication imperfections and angular spread of the IR beam.

Another recently emerged approach to achieving sharp spectral response and high field enhancement is based on Fano resonances [19, 18, 52, 7, 53, 54, 55, 56, 20]. The Fano resonance approach relies on local resonances of the meta-molecules and therefore is free of the disadvantages of coherent metamaterials. Fano resonances originate from the interference between two electromagnetic eigenmodes, referred to as "super-radiant" and "sub-radiant" [55, 56], of a multi-resonant meta-molecule. Such structures possessing high quality factors [52, 6, 57] could be used for quantitative biosensing, but suffer from the lack of molecular specificity because of the reliance on the frequency-independent refractive index of the protein. The FRAMM-based platform introduced below enables quantitative biosensing and fingerprinting of nm-scale multi-molecular nano-assemblies, and potentially allows the investigation of the underlying mechanisms of a wide class of bio-molecular interactions that are not accessible with current detection techniques. By tuning individual array elements toward (away from) protein's vibrational

38

resonances, we investigate, respectively, structural/spectroscopic and binding properties of nm-scale protein monolayers. The latter enable, for example, accurate determination of the overall monolayer thickness, while the former provide highly specific information about protein's orientation or conformational state. The asymmetry of the constitutive meta-molecules of the FRAMM enables precise experimental determination of the spectral positions of Fano resonances, while resonant field enhancement dramatically boosts the transduction of the protein's structural and binding properties into an infrared signal. We demonstrate the biosensing and fingerprinting capabilities of the FRAMM-based multi-pixel substrate by testing it on a well-defined ultra-thin multi-protein layer (a target protein monolayer deposited on top of a recognition monolayer). Specifically, we demonstrate: (i) vibrational fingerprinting and measurement of the thickness h_1 of the monolayer of recognition proteins (Protein A/G); (ii) detection of antibody (anti-mouse IgG from goat) binding to protein-immobilized surfaces, and determination of the thickness h_2 of the antibody monolayer using h_1 as a molecular yardstick; (iii) determination of spatial orientation of the proteins with respect to the metal surface normal. The last information is vital in determining their functional availability for bio-targeting [37 , 58, 59]. The FRAMM array also opens exciting possibilities for rapid biosensing when standard techniques of parallel acquisition of multiple infrared spectra by focal plane array (FPA) detectors [60] are applied to multi-pixel FRAMM-based functionalized substrates. Potentially this platform will allow monitoring of a wide class of biomolecular interactions with characteristics that are not accessible with current detection techniques.

4.2 **THEORETICAL BACKGROUND OF THE FRAMM-BASED BIOSENSING**

An example of an asymmetric metamaterial comprised of two plasmonic antennas along the y-axis and a perpendicular antenna coupler attached to one of them is shown in Fig. 4.1. Near-field interaction between the two antennas results in parallel (electric dipole) and anti-parallel (quadrupole/magnetic dipole) current excitations in the y direction corresponding to super- and sub-radiant modes, as indicated in Fig. 4.1(a). Using the coupled mode theory depicted in Chapter 2, we use a_y and a_Q to represent the super- and the sub-radiant modes. On the other hand, the short antenna aligned in the x direction provides a current excitation in the x direction, which we denoted by a_x. If the two parallel antennas are identical, the sub-radiant mode is completely dark ($\gamma_Q^{rad} = 0$) and decoupled from the normally incident light. The short antenna coupler in the x direction makes the meta-molecule asymmetric by breaking all spatial inversion/reflection symmetries in the plane of the structure. Such symmetry breaking not only introduces κ_{Qy} that directly couples the sub-radiant and super-radiant modes (thereby enabling Fano interference for the y-polarized incident light), but also induces κ_{xQ} that couples the sub-radiant mode to the perpendicular (x) polarization. The resonant frequencies of the sub- and super-radiant modes are primarily determined by the length L_1 of the two parallel antennas, while the length and position of the short horizontal segment determine the degree of symmetry breaking and the resonant frequency of the x polarized mode.

The equations of motion for the above system with three resonant modes can be obtained by extending Eq. (2.10), and are given by :

$$\frac{d}{dt}a_y = \left(i\omega_y - \gamma_y^{rad} - \gamma_y^{ohm}\right)a_y + ig_y a_Q + i\kappa_y S_y^+, \qquad (4.1)$$

$$\frac{d}{dt}a_x = (i\omega_x - \gamma_x^{rad} - \gamma_x^{ohm})a_x + ig_x a_Q + i\kappa_x S_x^+, \qquad (4.2)$$

$$\frac{d}{dt}a_Q = \left(i\omega_Q - \gamma_Q^{ohm}\right)a_Q + ig_y a_y + ig_x a_x \ . \qquad (4.3)$$

The resonant frequencies for the three modes are denoted by $\omega_{x/y/Q}$, and the radiative and the ohmic damping rates are given by $\gamma_{x/y}^{rad}$ and $\gamma_{x/y/Q}^{ohm}$ (the radiative damping of the quadruple is assumed zero), respectively. Coupling between the quadruple and the x/y dipoles are denoted by $g_{x/y}$, and the x/y dipoles are excited by the incident fields, S_x^+ and S_y^+, with the coupling coefficients, κ_x and κ_y. The total damping rate for the x and y polarized resonances are denoted as $\gamma_{x/y} = \gamma_{x/y}^{rad} + \gamma_{x/y}^{ohm}$. The constraints derived in Chapter 2, such as $\kappa_{x/y}^2 = \gamma_{x/y}^{rad}$ (notice that there are two radiation channels, see the discussion in Sec. 2.3), are still valid for this system. Noticing that the x polarized resonance is spectrally distant from the sub-radiant mode, $\left| \omega_x - \omega_Q \right| \gg \gamma_Q^{ohm}$, because of the shorter length of the horizontal antenna, we can solve Eq. (4.2) by approximating $\frac{d}{dt} a_x \approx i\omega_Q a_x$. Substituting $a_x \approx (ig_x Q + i\kappa_x S_x^+)/(i\omega_Q - i\omega_x + \gamma_x)$ obtained from Eq. (4.2) into Eq. (4.3), one has:

$$\frac{d}{dt} a_Q = i\omega_Q' - \gamma_Q' + ig_y a_y + i\kappa_x' S_x^+ \ , \qquad (4.4)$$

with $\omega_Q' = \omega_Q + q_x^2 \frac{\omega_Q - \omega_x}{\left[(\omega_Q - \omega_x)^2 + \gamma_x^2 \right]}$, $\gamma_Q' = \gamma_Q + q_x^2 \frac{\gamma_x}{\left[(\omega_Q - \omega_x)^2 + \gamma_x^2 \right]}$, and $\kappa_x' = \frac{q_x \kappa_x}{\omega_Q - \omega_x - i\gamma_x}$.

Equation (4.4) indicates that the quadrupolar mode is dressed by interacting with a_x, and acquires modified resonant frequency, damping rate, and coupling constant to the x polarized incidence. Combining Eqs. (4.1) and (4.4), the problem is then reduced to the system with coupling between two resonant modes:

$$\begin{pmatrix} i\omega - i\omega_y^* & -ig_y \\ -ig_y & i\omega - i\omega_Q'^* \end{pmatrix} \begin{pmatrix} a_y \\ a_Q \end{pmatrix} = \begin{pmatrix} i\kappa_y & 0 \\ 0 & i\kappa_x' \end{pmatrix} \begin{pmatrix} S_y^+ \\ S_x^+ \end{pmatrix}, \qquad (4.5)$$

where $\omega_y^* = \omega_y + i\gamma_y$ and $\omega_Q'^* = \omega_Q' + i\gamma_Q'$ are the complex natural frequencies. To find the eigenmodes of the system, we diagonalize Eq. (4.5) using the bright mode (a_B) and dark mode (a_D) basis and obtain:

$$\begin{pmatrix} i\omega - i\omega_B^* & 0 \\ 0 & i\omega - i\omega_D^* \end{pmatrix} \begin{pmatrix} a_B \\ a_D \end{pmatrix} = \begin{pmatrix} i\kappa_{By} & i\kappa_{Bx} \\ i\kappa_{Dy} & i\kappa_{Dx} \end{pmatrix} \begin{pmatrix} S_y^+ \\ S_x^+ \end{pmatrix}, \qquad (4.6)$$

where

41

$$\begin{pmatrix} a_B \\ a_D \end{pmatrix} = \begin{pmatrix} cos\theta & -sin\theta \\ sin\theta & cos\theta \end{pmatrix} \begin{pmatrix} a_y \\ a_Q \end{pmatrix} = \widehat{M}(\theta) \begin{pmatrix} a_y \\ a_Q \end{pmatrix} , \tag{4.7}$$

and

$$\begin{pmatrix} i\kappa_{By} & i\kappa_{Bx} \\ i\kappa_{Dy} & i\kappa_{Dx} \end{pmatrix} = \widehat{M}(\theta) \begin{pmatrix} i\kappa_y & 0 \\ 0 & i\kappa_x' \end{pmatrix} . \tag{4.8}$$

$\omega_{B/D}^* = \frac{1}{2} \left[\omega_y^* + \omega_Q'^* \pm \sqrt{\left(\omega_y^* - \omega_Q'^* \right)^2 - 4g_y^2} \right]$ are the eigen-frequencies of the coupled

system. The diagonalization matrix, $\widehat{M}(\theta)$, is defined in Eq. (4.7) with $tan2\theta = 2g_y/(\omega_Q'^* - \omega_y^*)$, or $\theta \approx g_y/(\omega_Q'^* - \omega_y^*)$ in the case of small g_y.

By using Eq. (4.6), the 2-by-2 reflection tensor $r_{\gamma\beta}$ (relating the reflected and incident electric fields according to $S_\alpha^- = r_{\alpha\beta} S_\beta^+$ with $\alpha, \beta = x$ or y) from the FRAMM substrate can be derived in a similar way as in deriving Eq. (2.13):

$$\begin{aligned} r_{\alpha\beta}^{(bare)} &= i\kappa_{B\alpha} a_B (S_\beta^+ = 1) + i\kappa_{D\alpha} a_D (S_\beta^+ = 1) \\ &= -\frac{\kappa_{B\alpha}\kappa_{B\beta}}{i(\omega - \omega_B) + \gamma_B} - \frac{\kappa_{D\alpha}\kappa_{D\beta}}{i(\omega - \omega_D) + \gamma_D} , \end{aligned} \tag{4.9}$$

Equation (4.9) is a double Lorenzian expression. The polarized reflectivities, $R_{\gamma\gamma}(\omega) = |r_{\gamma\gamma}|^2$, have either the Fano or the Lorenzian lineshapes because of disparate lifetimes $(\gamma_B \gg \gamma_D)$ of the modes and their different coupling efficiencies to y- and x-polarizations $(\kappa_{Bx} \ll \kappa_{Dx}$ and $\kappa_{By} \gg \kappa_{Bx})$.

Solid lines in Fig. 4.1(c) show the reflection spectra from one of the FRAMM samples for both y- and x-polarized incidence. The y-polarized reflection exhibits the typical Fano (i.e. asymmetric non-Lorentzian) resonance shape: it peaks at the frequency $\omega_B \approx 2000cm^{-1}$ of the dipole resonance, and experiences a rapid dip-to-peak variation as the frequency decreases from $\omega_{dip} \approx 1600cm^{-1}$ to $\omega_{peak} \approx 1450cm^{-1}$. Such variation indicates the presence of a dark resonance at the frequency $\omega_{dip} < \omega_D < \omega_{peak}$, but does not exactly identify its frequency ω_D which must be determined by other means.
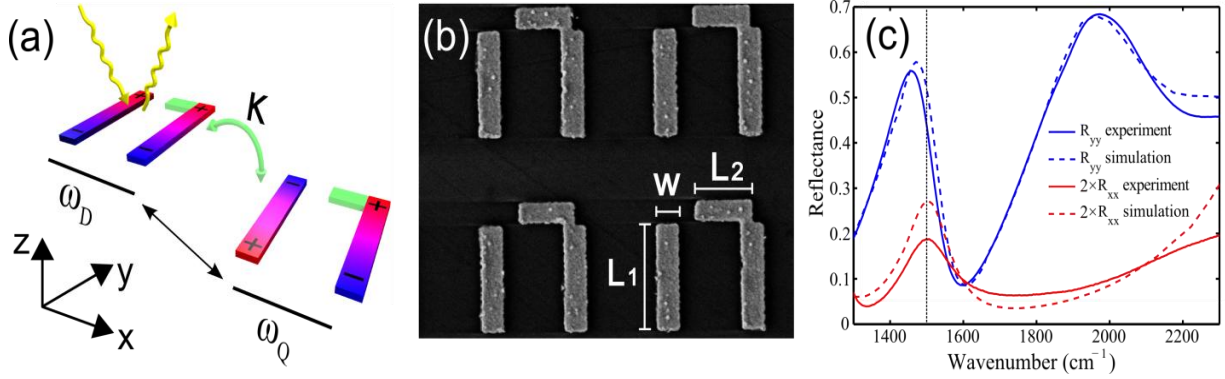
Figure 4.1: Geometry and electromagnetic properties of a Fano-resonant asymmetric metamaterial (FRAMM). (a) Schematic of the dark and the bright modes of the FRAMM coupled to incident infrared light. (b) SEM image of a typical fabricated FRAMM and geometric sizes: $L_1 = 1.8\mu m$, $L_2 = 0.9\mu m$, $w = 0.36\mu m$, metal thickness=70 nm, and periodicities in x- and y-direction are $P_x = 2.7\mu m$ and $P_y = 3.15\ \mu m$. (c) Experimental (solid) and theoretical (dashed: COMSOL simulations) polarized reflectivity spectra: Fano (Lorentzian) lineshaps for vertical (horizontal) polarizations.

On the other hand, the x-polarized spectrum in Fig. 4.1 (c) shows a nearly Lorenzian lineshape peaking at ω_D. This is because the FRAMM allows the dark mode to be excited alone with x-polarized light, in which case no interference with the y-polarized bright mode occurs. Earlier work on Fano interferences [55, 56, 61] relied on numerical

simulations of the charge distribution inside the plasmonic structures for identifying the exact spectral position of the sub-radiant resonances. Asymmetric structures enable direct experimental identification of the sub-radiant modes. Using the orthogonally-polarized spectroscopy (E field parallel to the x-direction), the Lorenzian reflectivity peak accurately identifies the spectral location of the quadrupolar mode.

According to the coupled mode theory, the difference in lifetimes and polarization-dependent radiative coupling efficiencies determines the near-field enhancement at the FRAMM's surface that is crucial for plasmon-enhanced sensing techniques [34, 36, 46]. Specifically, it can be shown that field intensities corresponding to y-polarized excitation of dark (Fano) and bright modes scale with their lifetimes as: $(\frac{|E_{Dy}/E_{inc}|}{|E_{By}/E_{inc}|})^2 = \frac{\gamma_B}{\gamma_D} = \frac{q_D}{q_B}$, where $q_{D(B)}$ are the quality factors ($q_D \approx 8.4, q_B \approx 2.7$ for the structures in Fig. 4.1). Excitation of the Fano resonance using x-polarized radiation yields a much smaller field enhancement: $(\frac{|E_{Dy}/E_{inc}|}{|E_{Dx}/E_{inc}|})^2 = (|\kappa_{Dy}/\kappa_{Dx}|)^2$. These analytic predictions were confirmed using COMSOL simulations shown in Fig. 4.2 (a,b), where the near-field enhancement around the FRAMM is computed for the three possibilities of exciting FRAMM's resonances: (i/iii) narrow-band Fano resonance excited by *y/x*-polarized radiation, and (ii) broad-band super-radiant resonance excited by *y*-polarized radiation. Only the Case (i) corresponding to Fano interference leads to large spectrally-selective enhancement of the near field and holds promise for sensing applications as demonstrated below.
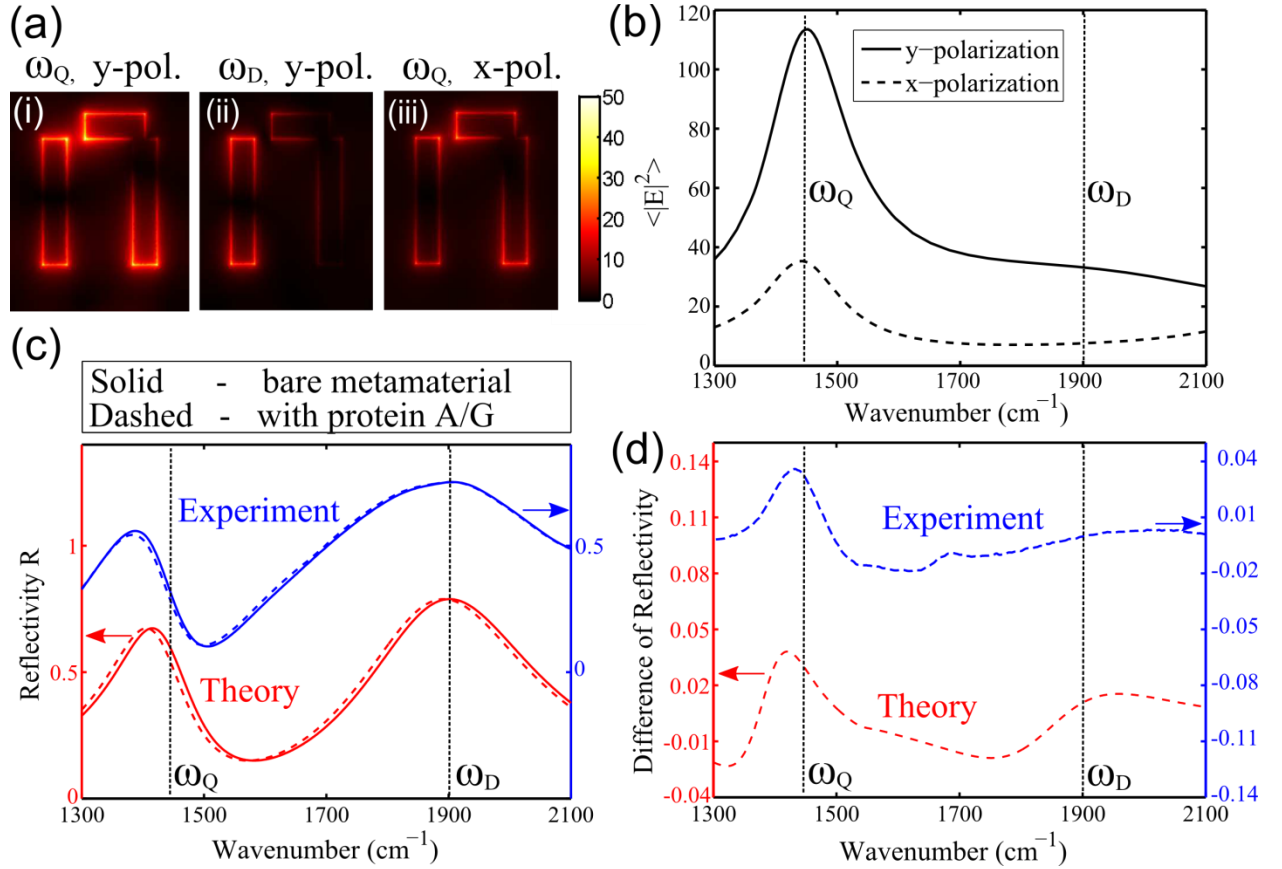
Figure 4.2: Near fields of the FRAMMs for different frequencies and incident polarizations and their manifestations in IR reflectance spectroscopy. (a) Field profiles and enhancement of $|E|$ (color bar). (b) Enhancement of $|E|^2$ averaged over a hypothetical 10nm thick monolayer is highest for Fano resonance (i). (c) Analytic and measured reflectivity from FRAMMs before (solid lines) and after (dashed lines) functionalized with a 3nm thick Protein A/G monolayer. (d) Analytic and experimental reflectivity difference $\Delta R(\omega)$ caused by the Protein A/G monolayer.

Detection and characterization of protein monolayers with FRAMMs are accomplished by measuring difference reflectivity, $\Delta R(\omega) = |r_{yy}^{(bare)}(\omega)|^2 - |r_{yy}^{(func)}(\omega)|^2$, between the bare and functionalized substrates. Presence of the protein monolayers of thickness h changes the dielectric environment of the FRAMM and results in frequency shifts $\Delta\omega_{D(B)}$ given by [62]:

$$\Delta\omega_{D(B)}/\omega_{D(B)} =$$

$$-\frac{1}{2}\int_0^h \boldsymbol{E}_{D(B)}(\boldsymbol{r}) \cdot (\hat{\epsilon} - 1) \cdot \boldsymbol{E}_{D(B)}(\boldsymbol{r})d\boldsymbol{r} / \int_0^\infty |\boldsymbol{E}_{D(B)}(\boldsymbol{r})|^2 d\boldsymbol{r}, \quad (4.10)$$

where $\boldsymbol{E}_{D(B)}(\boldsymbol{r})$ is the near field of the dark (bright) mode, and $\hat{\epsilon}$ is the permittivity tensor of the protein. The complex-valued $\Delta\omega_{D(B)}$ affects both the spectral position (index-induced shift) and lifetime (surface-enhanced absorption) of the FRAMM's resonances. The modified reflectivity tensor, $r_{\gamma\beta}^{(func)}$, of the functionalized FRAMM is obtained from Eq. (4.9) by substituting $\omega_{D(B)} \to \omega_{D(B)} + \Delta\omega_{D(B)}$, resulting in the change, $\Delta R(\omega)$, as shown in Fig. 4.2 (c,d).

Because the electric field is predominantly normal to the metal surface, the frequency shift scales with h according to $\Delta\omega_{D(B)}/\omega_{D(B)} \propto (\epsilon_n - 1)h/l_{D(B)}$. Here we assume that the modes' surface-averaged localization length $l_{D(B)} \gg h$. According to numerical simulations for the sub-radiant mode $l_D \sim 50\, nm$. The direction-dependent permittivity, $\epsilon_n \equiv \boldsymbol{n} \cdot \hat{\epsilon} \cdot \boldsymbol{n}$, is assumed to be approximated by a multi-resonant series:

$$\epsilon_n(\omega) = n_\infty^2 + \sum_m \frac{A_m <cos^2 \theta_m>}{(\omega-\omega_m)-j\gamma_m}, \quad (4.11)$$

where the summation is over all infrared-active vibrational modes with natural frequencies ω_m, damping rates $\gamma_m \equiv 1/\tau_m$, and dipole strengths A_m, and $n_\infty \equiv \epsilon_\infty^{1/2} \approx 1.55$ is the non-specific refractive index. The surface selection rule [63] rescales the dipole strength: $\tilde{A}_m \equiv A_m < \cos^2 \theta_m >$ according to the averaged orientation of the m'th vibration mode with respect to the metal surface normal $\boldsymbol{n}$. The *structure-resolving biosensing* is accomplished by an array of FRAMM pixels that are spectrally-tuned either *to* various vibrational resonances (spectroscopic characterization of conformational states and orientations of bio-molecules) or *away* from them (determination of the nano-layer thickness h using the non-specific n_∞).

4.3 APPLICATIONS OF FRAMMS TO FINGERPRINTING AND CHARACTERIZATION OF PROTEIN MONOLAYERS.

Several arrays of gold FRAMMs were fabricated on a quartz substrate, as shown in Fig.1(b), with their reflectivity spectra measured using a Fourier-transform infrared (FTIR) microscope (see Methods). 150 μm×150 μm FRAMM pixels were designed to resonate at different frequencies $1340 cm^{-1} < \omega_D < 1860 cm^{-1}$ by uniformly scaling their dimensions. Measured reflectivity spectra from a typical pixel shown in Fig. 4.1 (c) are used to determine the Fano resonance frequency ω_D from the peak of $R_{xx}(\omega)$, and are accurately fitted with numerical (COMSOL) and analytic (coupled mode theory) calculations. The structure-specific biosensing was demonstrated by immobilizing two protein nano-layers on the FRAMM's surface: (a) monolayer of a single recognition protein A/G of thickness h_1 , and (b) multi-protein bi-layer of thickness $H = h_1 + h_2$ consisting of a monolayer of goat antibody IgG of thickness h_2 on top of the protein A/G as shown schematically in Fig. 4.3(b). Optical transduction of protein binding to gold is done by measuring normalized differential reflectivity $D^{(\omega_D)}(\omega) \equiv \Delta R^{(\omega_D)}(\omega)/R_D^{(\omega_D)}(\omega = \omega_D)$ for each FRAMM pixel uniquely labeled by its ω_D.

To illustrate the concept of structure-specific biosensing, we note that the spectral maximum $D^{(\omega_D)} \equiv D^{(\omega_D)}(\omega = \omega_D)$ depends on the frequencies' mismatch between ω_D and those (ω_m's) of the vibrational modes of the proteins (e.g., Amide-I/II), as well as the specific (and *a priori* unknown) properties of the modes: their dipole strengths, lifetimes, and bond orientation. The strongest interaction between the proteins and the FRAMMs corresponding to the largest $D^{(\omega_D)}$ occurs when the frequency/lifetime $(\omega_D, 1/\gamma_D)$ of the FRAMM coincides with those (ω_m, τ_m) of one of the vibrational modes of the molecules [64]. Although the lifetime matching is beyond the scope of this

work, frequency matching of ω_D to ω_I (green line) yields the largest $\Delta R/R_D$ among the three FRAMMs shown in Figs. 4.3 (a,c). However, if the Fano resonance is tuned *away* from the Amide vibrations ($|\omega_D - \omega_m| \gg 1/\tau_D$), the value of $D^{(\omega_D)} \sim h(\epsilon_\infty - 1)$ yields the non-specific protein's thickness h. By comparing theoretically and experimentally obtained difference spectra, we found that $h_1 \approx 2.7nm$, which is in good agreement with $h_1 \approx 2.8nm$ obtained by ellipsometry. Protein A/G monolayer changes the reflectivity by easily detectable $\Delta R^{(mono)}(\omega = \omega_D) = 4\%$ (see Fig. 4.2 (d) and blue/red spectra in Figs. 4.3 (a) (c)), indicating that molecular monolayer thickness can be reliably measured with nm-scale accuracy.
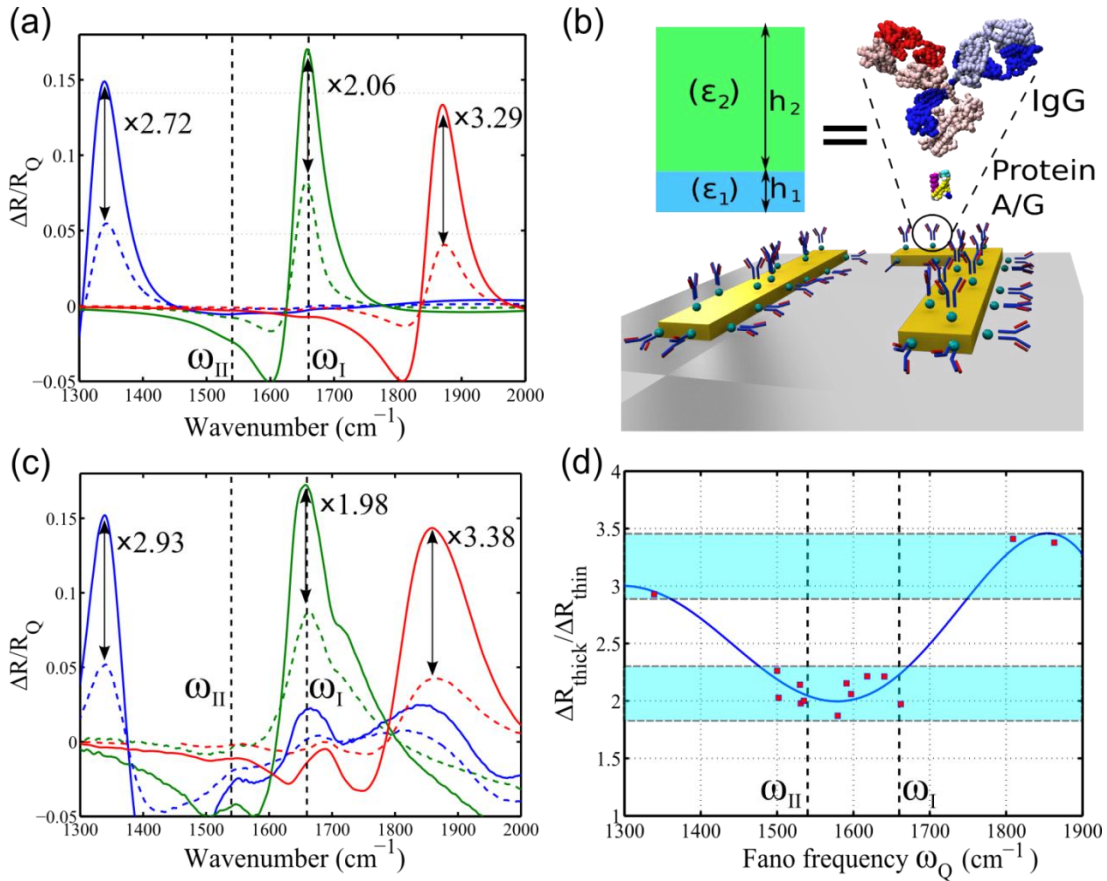
Figure 4.3: Application of FRAMM-based substrates to reflectivity-difference spectroscopy of protein mono- and bi-layers. Protein A/G serves as a recognition moiety; IgG antibodies are the target molecules binding to Protein A/G. The plotted quantity is the normalized reflectivity $D^{(\omega_D)}(\omega) \equiv \Delta R^{(\omega_D)}(\omega)/R_D^{(\omega_D)}(\omega = \omega_D)$ (a) Theoretical and (c) experimental spectra before (dashed lines) and after (solid lines) binding of IgG antibodies to three different FRAMM substrates immobilized by the Protein A/G. Indicated reflectivity ratios vary with the spectral position of the FRAMMs' resonant frequencies. (b) Schematics of proteins' mono- and bi-layers binding to the metal surface (not to scale) and the equivalent dielectric model. (d) Experimental peak reflectivity ratios (markers: 14 FRAMM arrays on 3 separate wafers). Dashed vertical lines: frequencies of the Amide-I and Amide-II vibrational modes.

Similarly, binding of the IgG antibody monolayer to the protein-immobilized FRAMMs is detected by measuring the $\Delta R^{(bi)}(\omega)$ (solid lines) spectra of the resulting protein bi-layer with the thickness $H^{(el)} = h_1 + h_2 \approx 7.9 nm$ (ellipsometric value) and comparing it with $\Delta R^{(mono)}(\omega)$ (dashed lines) in Fig.3(c). Larger overall thickness of the bi-layer clearly manifests in the peak reflectivity ratios $T(\omega_D) \equiv \frac{\Delta R_{max}^{(bi)}}{\Delta R_{max}^{(mono)}} > 1$ for all three FRAMMs in Fig. 4.3(c). The expected $T(\omega_D) \approx H/h_1$ for the FRAMMs satisfying $|\omega_D - \omega_m| \gg 1/\tau_D$ provides an accurate measurement of the thickness h_2 of the IgG monolayer by using h_1 as a *molecular yardstick*. By comparing the experimental data to the analytical model, $T(\omega_D) \approx 2.9$ was estimated, or $H \approx 7.8 nm$ and $h_2 \approx 5.1 nm$. For antibodies, h_2 provides indirect information [58, 65] about their orientation on the surface and the availability of antigen binding. Specifically, h_2 is a lower bound of the actual height of the IgG layer (which has a high void fraction due to its multi-fragmented structure). Because the height of the lying-on IgG is only about 4 nm, we conclude that the IgGs are mostly end-on oriented.

While the above thickness measurement is not structure-specific, we demonstrate below that an array of FRAMM pixels (labeled by their ω_D) can be used for *vibrational fingerprinting* of proteins. The non-specific contribution to $\Delta R/R_D$ due to ϵ_∞ is effectively eliminated by calculating the first frequency derivative of the reflectivity spectrum $G^{(\omega_D)}(\omega) \equiv -\frac{d(\Delta R^{(\omega_D)})}{d\omega} / \frac{d(R^{(\omega_D)})}{d\omega}(\omega = \omega_D)$. Specifically, $G^{(\omega_D)}(\omega = \omega_D)$ exhibits a local maximum when the Fano resonance frequency ω_D is matched to that of a vibrational mode (e.g., $\omega_{I,II}$). This occurs because of the reduction of the sub-radiant mode's lifetime due to the energy exchange between the FRAMM's electromagnetic mode and the protein's vibrational mode. Specifically, the magnitude of the spectral peak $G^{(\omega_D)}(\omega = \omega_D) \sim (h/l_D) \times (A_m < \cos^2 \theta_m > /\gamma_m^2)$ yields information about spatial orientation of the vibrational modes.
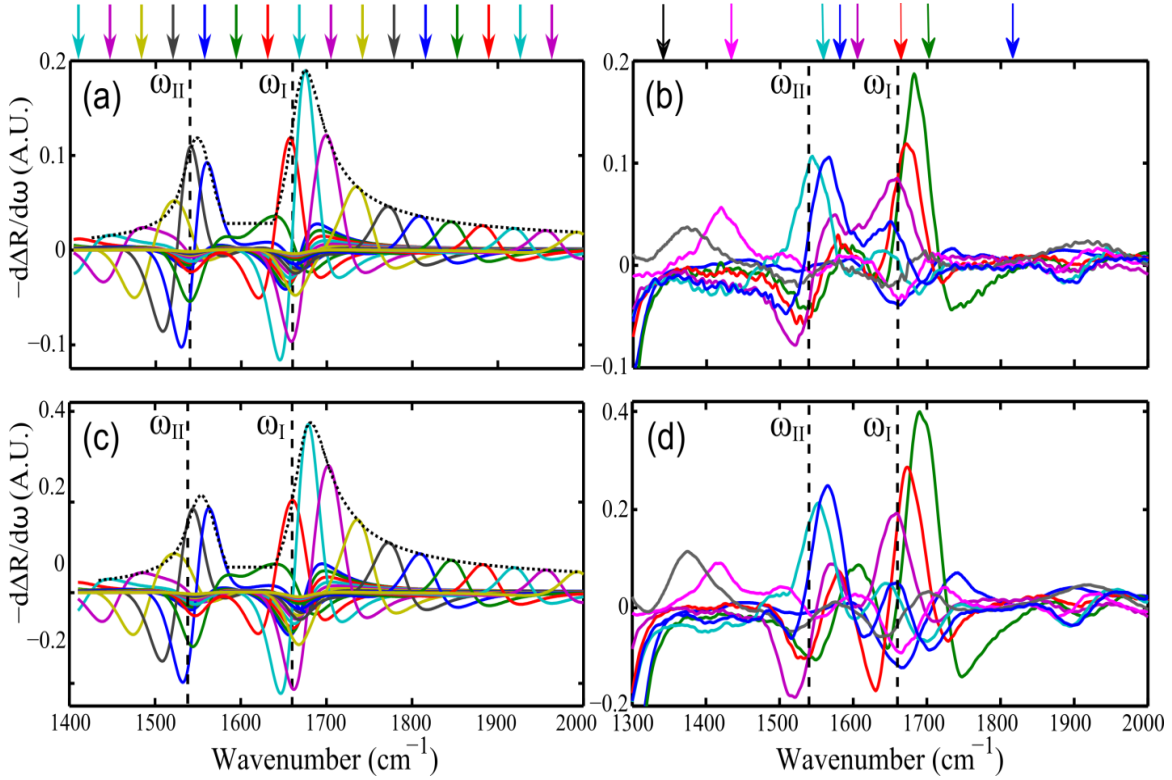
Figure 4.4: Visualization and identification of vibrational resonances of proteins using the normalized first frequency derivative spectra $G^{(\omega_D)}(\omega)$ from an array of FRAMM-based pixels. (a,c) theoretical and (b,d) experimental data for (a,b) Protein A/G monolayer (recognition moiety) and (c,d) Protein A/G + IgG antibody bi-layer. Different FRAMM pixels are color-coded and their resonant frequencies ω_D are indicated by arrows. Vertical dashed lines: frequencies of protein backbone vibrations (Amide I/II) strongly coupled to the resonantly-tuned FRAMMs. Smaller peaks in (b,d) around $\approx$ $1400 cm^{-1}$: CH3 bending modes of the proteins' side chains. Dotted curves in (a,c): envelopes of the maxima of $G^{(\omega_D)}$.

Theoretical plots of $G^{(\omega_D)}(\omega)$ are shown in Figs. 4.4 (a,c) for an array of 16 different FRAMM pixels coupled to Protein A/G (recognition moiety) monolayer and the combined Protein A/G + IgG (recognition moiety + target) bi-layer, respectively, where both proteins are described by the two-resonance model of $\epsilon^{(1,2)}$ given by Eq. (4.11). Experimental measurements shown in Figs. 4.4 (b,d) confirm that the maxima of

51

$G^{(\omega_D)}(\omega)$ are spectrally co-located with vibrational resonances of the monolayer and bi-layer. The data in Figs. 4.4 (b,d) indicates that there is strong coupling of the FRAMM with the strongest conformation-sensitive protein backbone vibrations (Amide I-II) that are frequently used for studying proteins' secondary structure [37, 38, 39]. They can also be used for estimating surface orientation of small highly anisotropic proteins such as protein A/G. One qualitative feature of Figs. 4.4 (b,d) is that the effective dipolar strength of the Amide I (C=O stretch) is stronger than that of the Amide II (C-N and C-C stretch, and N-H bend). This has been attributed [63] to stronger alignment of the Amide I with the axes of protein's alpha-helices, which are normal to the metal surface for oriented proteins.

Although our experiment involved single-detector *sequential* measurement of the FTIR spectra from eight FRAMM pixels, an FPA of infrared detectors would enable *parallel* [60] acquisition of the spectra from a large number of FRAMM pixels. Such parallelization of data acquisition from multiple pixels, each producing a resonantly-enhanced spectrum, results in enormous speed-up of label-free structure-sensitive optical bio-sensing.

4.4   ANISOTROPIC PROTEIN POLARIZABILITY REVEALING THE CONFORMATIONAL STATE

Finally, we illustrate how FRAMM-based biosensing enables distinguishing between multi-protein nanolayers by comparing $\Delta R^{(mono)}(\omega = \omega_D)$ for single-protein and $\Delta R^{(bi)}(\omega = \omega_D)$ for two-protein layers. If proteins A/G and IgG were identical, then $T(\omega_D) \approx H/h_1$ would be expected for all FRAMMs. However, Figs. 3(c,d) reveal a considerably smaller $T(\omega_D) < H/h_1$ for the resonantly-tuned FRAMMs. This implies a stronger contribution of Protein A/G's C=O vibration to $\epsilon_n(\omega)$ relatively to that of the

IgG, i.e. $\tilde{A}_I^{(A/G)} > \tilde{A}_I^{(IgG)}$. The analytical model predicts a similar trend for $T(\omega_D)$ when $\omega_D \approx \omega_I, \omega_{II}$. To interpret this result, we have used the Protein Data Bank (PDB) to extract and diagonalize the C=O directional tensors of the IgG and protein A/G.

The Amide I vibrational mode originates from the stretching of the C=O bond of the protein's backbone. To obtain proteins' directional tensor, $< \cos\theta_i \cos\theta_j >$ $(i, j = x, y, z)$, we acquired orientation of each C=O bond from the data provided by PDB. For each C=O bond, the tensor is given by $\cos\theta_i\cos\theta_j = < \hat{\imath}|\hat{d} >< \hat{d}|\hat{\jmath} >$, where $\hat{d}$ is the unit orientation vector aligned with the C=O bond. The total tensor is obtained by averaging over all amino acids. Protein A/G is a fusion protein that has four (67%) IgG binding domains from protein A and two (33%) from protein G. The 3D structure of protein A domains are obtained from PDB codes 1EDI and 1BDC and protein G domains from the Protein Data Bank codes 1GB1 and 2IGD. Although only two domains are available from PDB for protein A, the directional tensor is mainly determined by the secondary structure and is similar for the other domains. On the other hand, calculation for IgG is based on 3D structure obtained from PDB code 1IGY.

By assuming that the alpha-helices of protein A/G and the Fc region of IgG are parallel to the surface normal, we obtained $< \cos^2 \theta_I^{(IgG)} >_{kk} = (0.29; 0.32; 0.39)$ (almost isotropic) and $< \cos^2 \theta_I^{(A/G)} >_{kk} = (0.14; 0.22; 0.63)$ (highly anisotropic: strong Amide I contribution), where $k = x, y, z$. These estimates are consistent with the resonant absorption data $G^{(\omega_D)}(\omega)$ shown in Fig.4(b,d) by indicating that a bi-layer, which is $H/h_1 \approx 2.9$ times thicker than a monolayer, produces only twice the absorption:

$$G^{(\omega_D)}(\omega = \omega_Q) = 1 + (h_2/h_1) \times (< \cos^2 \theta_I^{(IgG)} >_{zz} / < \cos^2 \theta_I^{(A/G)} >_{zz}) \approx 2.2 \qquad .$$

Note that this result is not sensitive to IgG's binding orientation, but is highly sensitive to Protein A/G's surface binding. Therefore, the multi-pixel FRAMM provides valuable

53

information about the thickness and surface binding of small anisotropic proteins, as well as the target antibodies on protein-functionalized substrates.

4.5 OUTLOOK

The concept of a Fano-resonant asymmetric metamaterial (FRAMM) enables novel plasmonic substrates that combine strong near-field enhancement, sharp spectral features, and easy identification of the resonance frequency via polarized reflection spectroscopy. Designed to operate in mid-infrared part of the electromagnetic spectrum, such substrates can be used for implementing the structure-resolving label-free biosensing. Tremendous improvements in sensitivity, speed, and time-resolution of biosensing can be achieved by parallel acquisition of the FTIR spectra from large functionalized arrays of narrow-band FRAMM pixels covering a significant portion of the fingerprint spectral region. By using infrared-transparent substrates, one can envision unlocking the mysteries of the conformational dynamics of biomolecules in their natural aqueous environment responsible for life-sustaining molecular binding processes.

Chapter 5

Plasmonic Nano-protractor Based on Polarization Spectro-Tomography

5.1 INTRODUCTION

Near-field coupling between plasmonic nanoparticles (NPs) is sensitive to nanometer spatial changes of constituent components, which, in turn, leads to drastic changes in the far-field scattering spectra of the plasmonic cluster. Such idea of transducing spatial variation into spectral differences has been used in plasmonic rulers to measure length variations in biomolecules and nanoclusters. We propose and demonstrate a novel plasmonic protractor, which is based on a low-symmetry heterogeneous nanostructure comprised of simple yet distinct parts: a sphere and a rod. When the two NPs are coupled, a Fano resonance emerges from the interference between the dark, quadrupole mode of the rod and the bright, dipolar mode of the sphere. Polarization sensitive and tomography-like scattering measurements from different directions allow us to determine the relative position and orientation between the two NPs at the nanometer scale. The design principle of the protractor is general, therefore, applicable to a wide variety of NPs, including quantum dots. These plasmonic protractors may be useful for studying in-situ conformational changes such as rotation and bending at the single molecule level.

Subwavelength plasmonic nanostructures, typically made of noble metals, exhibit a wide variety of optical responses. By shaping the structural geometries and therefore confining conducting electrons within the nanostructures, the surface plasmonic resonances can be tailored in desired ways for various kinds of applications. One consequence of the small dimensions of the nano-resonators is their capability of confining electromagnetic fields in subwavelength regions, leading to enormous near

field enhancement [66, 67, 68]. The near fields are evanescent waves that exist only close to the plasmonic structures. Because the characteristic lengths of the near fields are much shorter than the free space wavelength, imaging techniques utilizing the near fields can reach resolution far beyond the diffraction limit [69, 70, 71, 72].

Metallic nanostructures exhibit rich and unique optical properties. Even individual nanoparticles (NP) of very simple geometric shape, such as spheres, rods, and cubes, host a variety of plamonic modes that evolve in a non-trivial way as the size and material change. When NPs are placed in close proximity of each other, the incident and scattered light interferes and produces a complex near field and far field scattering spectra. The possibility of shaping and controlling near field and far field optical properties expands enormously [56]. Since the near fields are evanescent waves that exist only close to the plasmonic structures, small variations in the cluster geometry can result in significant difference in the optical response of the whole cluster, and in turn changes the far field spectrum. For example, the resonant frequency of an assembled cluster depends strongly on the inter-particle distance [73, 74]. Such idea of transducing spatial variation into spectral differences is the main principle behind the plasmonic rulers capable of measuring length variations on the nanometer scale, and the subsequent development of practical tools for the real-time monitoring of biomolecules conformational dynamics on the single molecule level [75]. However, conformational changes in the molecular state can involve not only length variation, but also rotation and bending between binding sites [76]. Therefore, a sensor that can provide complete information on all degrees of freedom is much desired[77].

Optical detection and imaging of very small objects using monochromatic light is made extremely challenging by two general physical principles. First, the finite wavelength of light λ limits spatial resolution: locations of individual nanoparticles

(NPs) can be determined with the accuracy of $\approx \lambda / 2$ known as the diffraction limit. Second, small NPs with a characteristic spatial dimension $a \ll \lambda$ are virtually "invisible" because of their poor scattering efficiency scaling as $(a / \lambda)^6$. The diffraction limit can be partially overcome by, for example, ensuring that the NPs are far away from each other. This approach, however, does not permit spatially resolving several proximal NPs. Near field optical scanning microscopy (NSOM), on the other hand, is not constrained by the diffraction limit by employing scattering tips or holes with sub-wavelength dimensions $R \ll \lambda$ which defines the spatial resolution. In addition to the inconvenience of mechanical scanning, another drawback of NSOM is that the same poor scattering efficiency that renders NPs "invisible" also severely limits NSOM's optical signal. Therefore, relatively high power radiation sources, as well as complicated interferometric signal retrieval procedures must be employed to achieve strongly sub-diffraction resolution.

As demonstrated below, both diffraction and poor scattering limits can be overcome by coupling a resonant NP to a much larger plasmonic scattering particle (SP) of the dimension $R \ll \lambda$ and measuring the dark-field polarization-resolved scattering spectra of the resulting SP-NP hybrid. To mimic a barely visible resonant NP, we use a plasmonic nanorod whose length is chosen to correspond to possess a sharp "dark" (i.e. poorly scattering) resonance in the visible part of the spectrum. The SP is chosen to be a plasmonic nanosphere possessing a broadband ("bright") scattering resonance. By conducting the polarization spectro-tomography (PST) described below, we demonstrate that not only the proximity between the NP and SP can be ascertained, but also the angular position of the contact point between the two can be identified with the equivalent spatial resolution far exceeding the size of the SP. The PST approach relies of the phenomenon of Fano interference between the "bright" resonance of the SP and the

57

"dark" resonance of the NP. By engaging the individual spectral signatures of the NP's, this approach could be used for spatially resolving multiple NPs proximate to the SP.

In this chapter, we demonstrate a novel concept of plasmonic protractor both theoretically and experimentally. The plasmonic protractor is essentially a low-symmetry heterogeneous nanostructure comprised of very distinct parts: a rod and a sphere in our case. By using the Fano interference between the bright mode of a probing NP (i.e., the sphere) and the dark mode of a target NP (i.e., the rod), far-field optical scattering measurements can be used to determine the relative position and orientation between the NPs with a resolution well beyond the diffraction limit. The dark mode of the target NP alone is not visible in the scattering measurement due to its small cross section. When coupled to the probing NP via the near-field interaction, however, the target NP modifies the scattering spectrum significantly. The plasmonic protractor offers numerous advantages over existing sensing and imaging techniques. In general, plasmonic sensors provide large photon counts [75] and improved photo-stability compared to fluorescence resonance energy transfer [78, 79]. In contrast to the plasmonic rulers, the plasmonic protractor shown here also provides additional rotational information on the relative orientation between the NPs. In addition, several NPs with non-overlapping dark states can be monitored simultaneously due to the narrow linewidth of the dark modes.
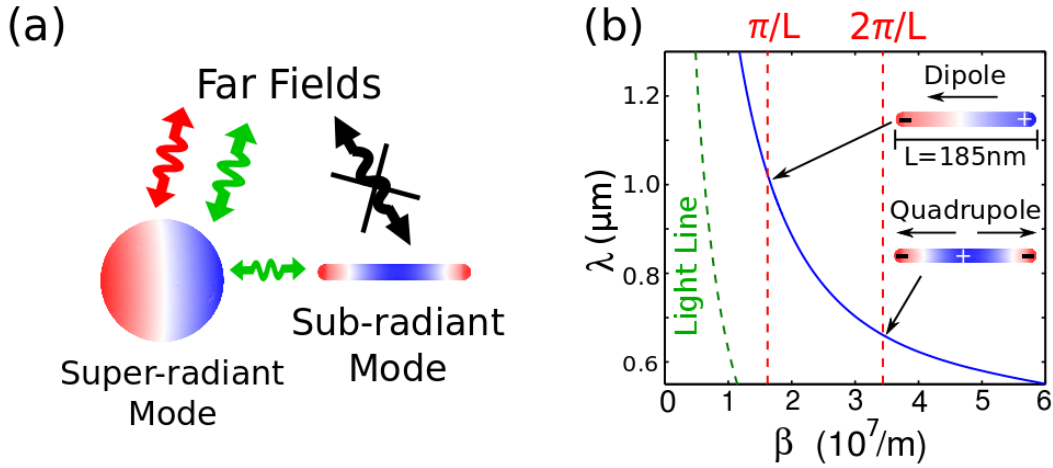
Figure 5.1: (a) An illustration of the Fano resonance. Green and red represent two different path ways giving rise to the Fano interference. (b) The dispersion of the surface plasmon in a gold nanorod with a 20nm diameter. The resonance condition is $\beta \approx n\,\pi/L$ where n=1 (2) is the dipolar (quadrupolar) mode.

Fano resonances generally originate from the interference of two spectrally overlapping resonant modes with very distinct quality factors (Q). In our case, the low Q resonance is the dipole mode of the sphere where the resonant wavelengths depend on the particle size. The high Q resonance is the quadrupolar mode of the rod. The resonances of a nanorod correspond to the standing waves of the surface plasmon oscillation along the length of the rod [80]. The resonance condition is given by $L \approx n\,\pi/\beta$, where β is the propagation constant of the surface plasmon along the rod. The $n = 1$ mode corresponds to a dipolar resonance, while the $n = 2$ mode is a quadrupolar resonance. The resonant wavelengths of the dipolar and quadrupolar modes of the rod used in this experiment are estimated from the standing wave criterion as shown in Fig. 5.1 (b). Since

the net dipole moment of the quadrupolar mode is zero, the associated radiative loss is suppressed, making the eigenmode dark. The spectral position of this dark resonance is tunable with the nanorod length. When the sphere and rod are placed in close proximity with each other, the optically excited bright mode of the sphere can either decay directly into the far field or undergo energy transfer with the dark mode of the nearby rod. The interference of these two pathways, as illustrated in Fig. 1(a), leads to an asymmetric lineshape in the scattering spectra [6, 19, 52, 7, 54, 20, 81, 55 , 53, 82]. Fano resonances have been extensively studied in plasmonic structures including periodic arrays [6, 52, 7, 53], self-assembled clusters [56, 55], and core-shell structures [81]. The previous observations of Fano resonances are based on the collective mode of an array of metallic structures or relatively simple and symmetric NPs such as disks or spheres. The plasmonic protractor under investigation is a low symmetry heterogeneous nanostructure, therefore, possesses a much more complex optical response that includes cross-polarizability (i.e. a non-diagonal polarizability tensor) and bi-anisotropy (coupling between electric and magnetic responses).

5.2   THE FANO INTERFERENCE INDUCED BY THE NEAR FIELD INTERACTION

We first identified the Fano resonance in the scattering spectrum of the rod-sphere cluster. The cluster consisting of a single gold sphere (~150 nm in diameter) and rod (~ 20 nm in diameter and ~185 nm in length) is assembled by atomic force microscope (AFM) nanomanipulation method depicted in Fig. 2 (a). The two NPs were initially spatially separated on a substrate. The green spectrum in Fig. 2 (c) shows the scattering spectrum in the relevant spectral range from the dipolar resonance of the isolated sphere. However, no significant scattering from the nanorod was observed in the detection

window from 600 nm to 900 nm, since the quadrupolar mode is dark. Next we pushed the nanosphere toward the nanorod using an AFM tip. Several steps in the manipulation process are shown in Fig. 2 (b) as we gradually moved the sphere to the rod. When the sphere was moved very close to one end of the rod, the precise distance and alignment between the two NPs can no longer be resolved by AFM imaging. Remarkably, such information can be obtained in the far-field optical scattering spectra. We observed a Fano resonance in the scattering spectrum, shown by the blue curve in Fig. 2 (c), indicating a dark mode close to 680 nm. In this case, the sphere and rod were close but not physically touching due to a dense layer of ligand coating on the surfaces of the NPs. We estimated that the distance between the two NPs was below 5nm. By comparing spectra from the preassembled and assembled clusters, we identified the Fano resonance without any ambiguity.
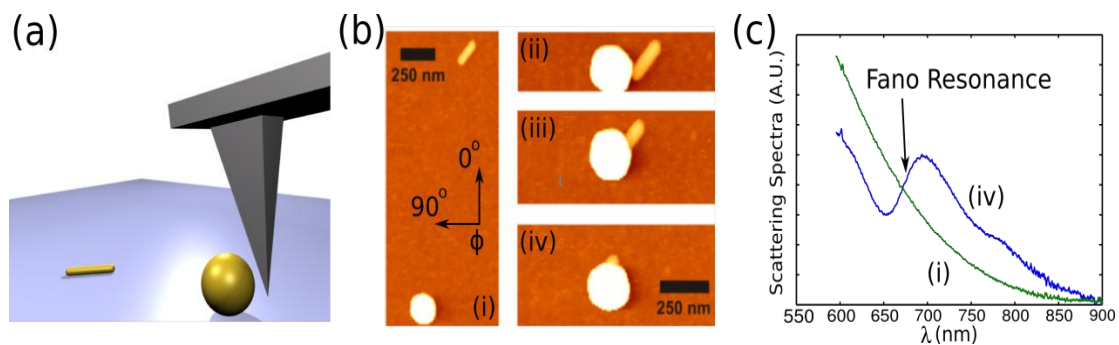
Figure 5.2: (a) An illustration of assembling the nanoculster using AFM. (b) AFM images of the nanosphere and the nanorod at different steps of assembling. (c) The scattering spectra measured before (green) and after (blue) the two NPs are assembled. After assembling, a Fano resonance is shown at $\lambda \approx 675 nm$.

There are three nearly degenerate dipolar modes with distinct spatial orientations in a sphere. The degeneracy of such isotropic dipolar modes is lifted when the sphere   is

coupled to the rod. Only the dipolar mode pointing along a certain direction (which we refer to as the Fano axis in the following discussion) is involved in the Fano resonance. The other two perpendicular modes remain uncoupled to the dark mode of the rod. The orientation of the Fano axis uniquely depends on the position of the nanorod with respect to the nanosphere. Quantitatively, the direction of the Fano axis is determined by the electrostatic interaction between the two NPs. When the radius of the sphere is much smaller than the wavelength of the scattered light (about 1/9 in our case), the near fields of the sphere can be expressed as electrostatic fields according to $E_i = -\nabla \phi_i$. Here $i = x, y, z$ denotes the direction of the individual dipolar mode of the sphere, and ϕ_i is the typical electrostatic potential of a dipole pointing in the i direction. As mentioned previously, the quadrupolar mode of the nanorod results from the full-wavelength resonance of the surface charge oscillation. The charge along the long axis of the rod can be represented by $\rho(x) = \rho_0 \cos(\beta x)$, where x is the distance from one end of the rod along the long axis, and $\beta = 2\pi/(L + \Delta L)$ is the propagation constant of the charge oscillation. The difference, ΔL, between the effective antenna length and the physical dimension (L) is due to the reactance of the rod's tips [80]. Using a Lagrangian model [83] and taking into account only the capacitive interaction between the two NPs, the interaction between the i dipolar mode and the quadrupolar mode is given by $\kappa_i = \int \phi_i(x)\rho(x)dx$ [84, 83]. It can be shown by rotating the reference coordinate system that only the specific dipolar mode parallel to $(\kappa_x, \kappa_y, \kappa_z)$ interacts with the quadrupolar mode of the nanorod. Therefore, the Fano resonance occurs along one specific direction that is determined by the position and orientation of the nanorod. Figure 3(b) shows the orientation of the Fano axis as a function of the rod position predicted by the quasistatic model. The same dependence is confirmed by the full electromagnetic as well as electrostatic simulations. In the case of small sphere radius compared to the rod

length, the Fano axis, denoted by the angular coordinate of θ_F, points along the line that connects the center of the sphere to the near end of the rod, denoted by the angular coordinate of θ_r. As the sphere radius increases, the Fano axis starts to deviate from the point closest to the nanorod, as is shown in Fig. 3 (b). This is because the extent of the nanosphere's near field is proportional to its radius. As the radius increases, the near field sees not only the charge distribution at the near end of rod but also that along the entire rod. Nevertheless, there is still a one-to-one correspondence between the Fano axis and the physical orientation of the two NPs. We note that the Fano axis is mainly determined by the angular coordinate θ_r. Although it does depend on the rotations of the rod around the tip, this effect is much less sensitive.
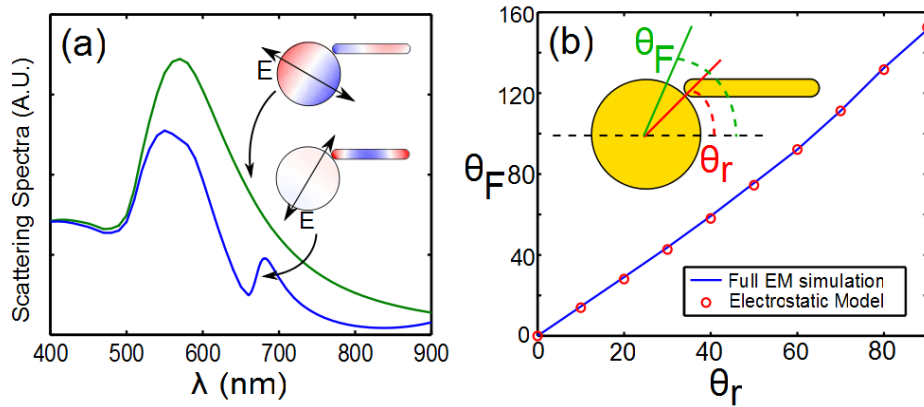
Figure 5.3: (a) The calculated scattering spectra when the incidence polarization is parallel (blue) and perpendicular (green) to the Fano axis. Insets show the charge distribution with different polarizations. At the Fano resonance, the dipolar mode is depolarized by the quadrupolar mode. (b) The dependence of the Fano axis angle on the rod position. θ_r is defined by the line connecting the sphere center to the near end of the rod.

5.3   DETERMINATION OF THE FANO AXIS USING POLARIZATION SPECTRO-TOMOGRAPHY

In order to specify the orientation of the Fano Axis, we need to determine its relative angle to two reference axes. We have chosen one reference axis ($\theta = 0°$) to be along the p-polarization direction of the incident beam and the other reference axis to be the projection of the incident beam on the substrate ($\phi = 0°$), as illustrated by Fig 4(a) and 4(b), respectively. These reference axes are chosen because they allow us to analyze the polarization resolved scattering spectra readily. We now describe the procedure for determining the Fano axis using polarization resolved dark field spectroscopy. Firstly, the incident beam passing through a polarizer is used to excite the sphere-rod cluster. The interference is most pronounced when the projection of the Fano axis onto the polarization direction is maximal. Therefore, this polarization scan enables the determination of the angle, denoted by θ in Fig. 4 (b), between the p-polarization and the Fano axis' projection onto the plane perpendicular to the incidence wave vector. Secondly, we fix the polarization of the incident beam, for instance, in the p-polarization, and then scan over the polarizations of the scattered field by using a polarization analyzer in the path of the scattered light. Similar to the situation of rotating the polarizer in the incident beam, the interference pattern is minimal when the analyzer is perpendicular to the Fano axis projection and maximal when they are parallel. The Fano axis can then be determined by combining these two measurements outlined above.

To quantify the Fano resonance, we introduce the spectral derivative at the resonant frequency: $D = -dI/d\omega|_{\omega_{Fano}}$, with I being the intensity of the scattered light. It can be seen in Fig. 3 (a) that D is negative when there is no Fano interference, and becomes positive when the Fano interference results in an asymmetric lineshape [82]. Figure 4 (c) shows an example of D versus θ, the direction of the polarizer, and

64

ϕ, the direction of the analyzer, when the Fano axis is intentionally aligned along the $\theta = 0°$ and $\phi = 0°$ direction. The maximum of D corresponds to the angular coordinates of the Fano axis.
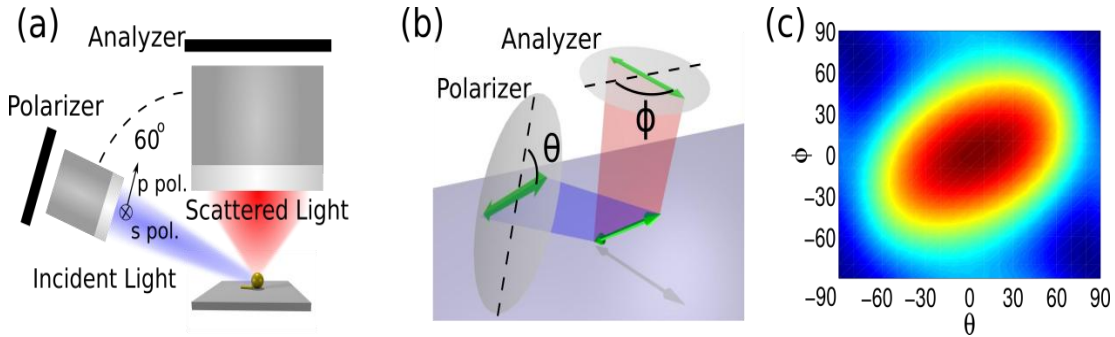
Figure 5.4: (a) A schematic of the PST using the dark field microscopy. (b) The Fano axis is determined by projecting onto both the polarizer and the analyzer. (c) An example when the Fano axis is along $\theta = 0$ and $\phi = 0$. Color represents the spectral derivative D.

We applied the procedure described above to determine the Fano axis of our particular nanocluster. A schematic of the dark field scattering set-up is shown in Fig. 4 (a). The incident angle of the white light beam was kept at $60°$, which then allow us to define the p-polarized light as $\theta = 0°$. the orientation of the sample the angle, $\phi = 0°$, is defined as the projection of the incident light on the substrate as illustrated in Fig. 5(a). The sample was rotated such that the structure is aligned with $\phi = 0°$as specified in Fig. 4(a). The nanocluster was first illuminated from the $\phi = 0°$ direction. By changing the angle of the polarizer, we observed variations in the scattering spectra shown in Fig. 5 (d) corresponding to the various degrees of excitation of the Fano resonance. The spectral

derivatives, D, corresponding to different polarizations were calculated and shown in Fig. 5 (g), from which we determined $\theta_{F1} = 110°$. Next, we fixed the incident beam at the p-polarization and varied an analyzer in the path of the scattered light. We found $\phi_{F1} = 80°$ from the measured spectra shown in Fig 5(f). Finally, we changed the incident direction to be $\phi = 180°$ and measured θ_{F2} without using the analyzer. The spectra in Fig. 5 (e) yielded $\theta_{F2} = 70°$. The Fano axis can then be determined by combining any two of the three measurements in principle. Figure 5 (a~c) show the resultant projection of the Fano axis determined from the experimental measurements. We note that both combinations of $[\theta_{F1}, \phi_{F1}]$ and $[\theta_{F1}, \theta_{F2}]$ give consistent results of the Fano axis.
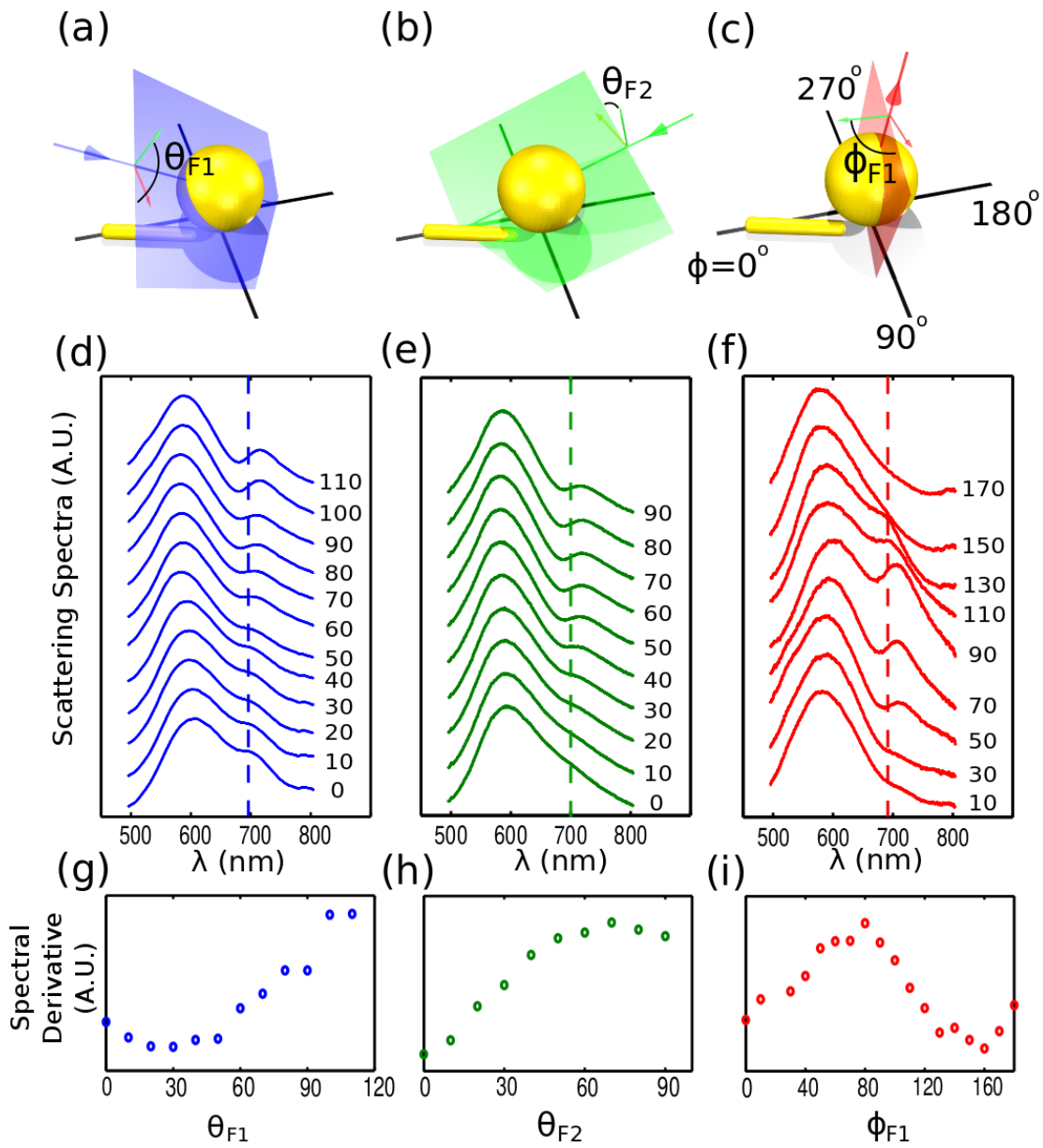
Figure 5.5: (a~c) Projection of the Fano axis onto the polarizers in (a) (b) and the analyzer in (c). (d,e) The measured spectra with the polarizers. The incidence came from $\phi = 0^o$ in (d) and from $\phi = 180^o$ in (e). (f) The measured spectra when the incidence is p polarized from $\phi = 0^o$ and with the analyzer. Spectral derivative as defined in the text are shown in (g~i).

67

5.4 CONCLUSION

In summary, we demonstrated that a simple nanocluster composed of two NPs can be used as a nano-plasmonic protractor to determine the NPs' relative position and orientation. The two NPs, one hosts the super-radiant mode and the other the sub-radiant mode, exhibit the Fano interference when they are coupled through the near-field interaction. Such interference enables the detection of the sub-radiant states in far field scattering measurements. In addition, the near-field interaction defines the polarization of the Fano resonance and is very sensitive to the position and the orientation of the NPs. Therefore, by determining the Fano axis one can track tiny movement of the nanorod with sensitivity well beyond the diffraction limit. We measured the Fano axis of an AFM-assembled nanocluster by using polarization-resolved scattering spectra. By either using both a polarizer and an analyzer to study the incident and the scattered lights or varying the polarizations of two incident beams coming from different directions, we obtained consistent results of the direction of the Fano axis. This information can't be obtained from scanning probe microscopy method such as AFM and SEM, which only provide two-dimensional mapping of topologic features. Although we used AFM nano-manipulation to assemble the prototypical NP cluster, the proposed nano-protractor is simple enough to be self-assembled. Finally, the proposed design principle of a protractor is general, therefore, applicable to a wide variety of target NPs, including quantum dots. We believe such nanoprotractors are useful for studying- angular molecular motions in the microscopic scale.

Chapter 6

Wide Angle and Nearly Perfect Absorption Induced by Fano Resonances

6.1   INTRODUCTION

The field of electromagnetic metamaterials (MMs) has been rapidly developing in recent years. New composite materials with sub-wavelength size and exotic electromagnetic properties generally unattainable in nature are being designed and produced for many applications such as perfect lenses [85], cloaking devices [86], sub-wavelength transmission lines and resonators [87], and agile antennas [88]. Another important application of MMs is the development of spectrally selective "perfect" absorbers [89] (near-unity peak absorptivity). Such absorbers can be used for developing sensitive detectors for a variety of security-related applications, as well as narrow-band thermal emitters for thermophotovoltaic (TPV) [90, 91] applications. In photovoltaic (PV) applications, ultra-thin MM absorbers can be applied on surfaces of thin-film solar cells to reduce reflectivity [92], thereby increasing the external quantum efficiency.

Miniaturization of these devices is highly desirable and can be achieved by making the metamaterial's unit cell strongly sub-wavelength. Strong confinement of electromagnetic fields to sub-wavelength regions of the resonant metamaterials results in spectrally selective absorption. An added benefit of the sub-wavelength unit cell is the wide-angle response of the metamaterials. The wide-angle response is important for making hyper-spectral focal plane arrays (FPA) comprised of ultra-small detector pixels. Angular directivity can also be detrimental for TPV applications because it effectively broadens the emission spectrum. While miniaturizing the unit cell for microwave/THz applications can be done using traditional MM approaches---such as making split-ring resonators [93]---fabrication challenges make such approaches impractical for optical

MMs. Therefore, plasmonic resonances of much simpler metallic structures [84] must be utilized to reduce the unit cell's size in optical MMs. Examples of such structures used in MM-based optical absorbers include metal strips [94, 95] and patches [96, 45] separated by a thin dielectric layer from a metallic ground plate. While the wide-angle absorption of these structures has been theoretically demonstrated [94, 95, 96, 45], no experimental evidence presently exists. Here we report on the fabrication and experimental demonstration of wide-angle, spectrally selective plasmonic surfaces exhibiting near-unity absorption of infrared radiation. The fabricated structure schematically shown in Fig. 6.1(a) is comprised of plasmonic strips separated from the plasmonic ground plate by an ultra-thin ($< \lambda/50$) dielectric spacer. Metamaterials with various unit cell dimensions and spacer materials were prepared using the method of ultraviolet nano-imprint lithography (NIL) [97]. The NIL process provides a means for large-area replication of the device pattern after an initial electron beam lithographic process is used to generate the reticle. This MM absorber encompasses the following advantageous characteristics: extremely high absorption approaching 100% over a wide range of incident angles, tunability of the absorption peak frequency demonstrated by changing the unit cell's dimensions, robustness against structure imperfections, sub-wavelength ($< 1 \, \mu m$) unit cell sizes, strong field confinement within the MM structure, and large MM area (> 1 mm^2 per MM pattern).

The rest of the Chapter is organized as follows. In Section 6.2, we describe theoretical tools used in calculating the effective impedance of a resonant plasmonic surface and introduce the single-resonance impedance model. Using eigenvalue simulations, we compute the complex impedance of the plasmonic absorber and explain the phenomenon of "perfect" absorption in terms of impedance matching of the absorber to that of vacuum. In Section 6.3, we describe the fabrication of the absorber using NIL.

In Section 6.4, we demonstrate high absorptivity and spectral tunability of the absorber both experimentally and theoretically. An external beamline based on FTIR spectroscopy was used to verify the wide-angle absorptivity predicted by numerical calculations. Implications of the wide-angle absorptivity are discussed in Section 6.5. The surface mode responsible for the high absorptivity is shown to be highly localized and has a propagation length shorter than the structure periodicity. Unit cells of the absorber function almost independently and have little cross-talk.

The absorber design creates an impedance-matched surface by strongly subwavelength patterning. It can be regarded as a homogeneous MM surface because each subwavelength unit cell absorbs independently. The origin of such impedance match is the magnetic resonance resulting from the structural design in additional to the electric response of the material. As a result of the subwavelength design and the plasmonic nature of the material, fields are locally confined and the absorption occurs within a small region of the material.

6.2 THEORETICAL DESCRIPTION OF THE FREQUENCY-SELECTIVE PLASMONIC ABSORBER

In the following we concentrate on the specific geometry of a resonant plasmonic absorber schematically shown in Fig. 1 (a) and (b), which is comprised of a periodic array of either plasmonic strips or square patches separated from a thick, non-transparent plasmonic mirror (further referred to as the ground plate, following the standard microwave terminology). As shown in Section 6.4, the spectral response of the square-patch structure shown in Fig. 1 (b) is qualitatively (and even quantitatively) similar to that of the one-dimensional structure. In this section we concentrate on the one-dimensional array of plasmonic strips [94] shown in Fig. 1 (a), where all dimensions of

the plasmonic absorber are defined. The structure is assumed uniform in the z direction and repeating in the y direction with a periodicity of L. Below we develop the theoretical formalism for computing the absorption of the nano-structured plasmonic surface based on the eigenvalue/eigenmode analysis. For simplicity, we restrict the incident wave to be P-polarized as shown in Fig. 6.1 (a), i.e., the incident wavenumber and the electric field lie in the x-y plane, whereas the magnetic field is aligned in the z direction.
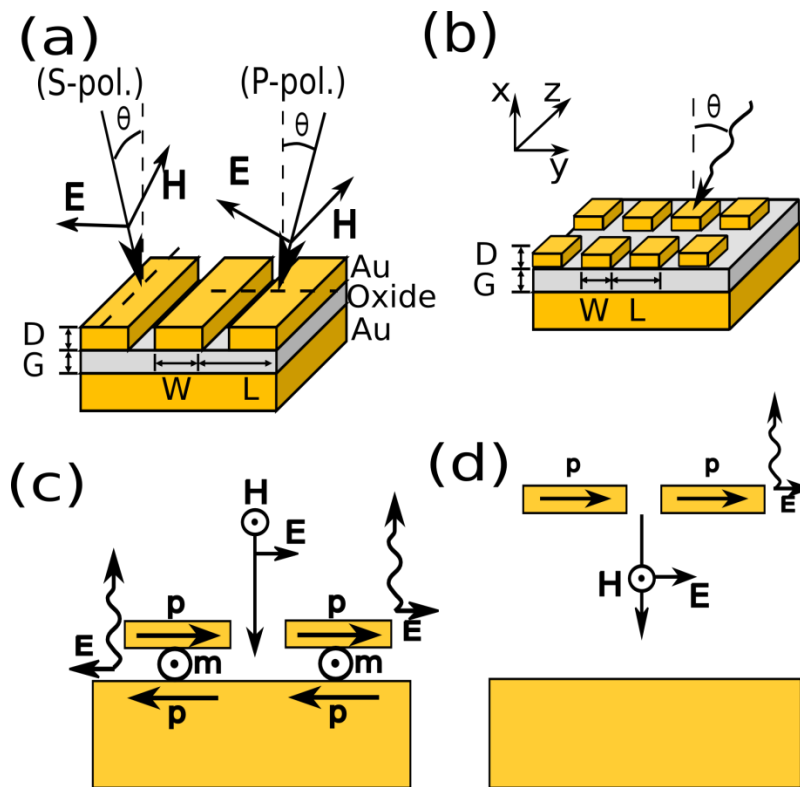
Figure 6.1: Schematic of the plasmonic absorber with (a) parallel strips and (b) square patches placed above the ground plate. (c), (d) Reduced radiative loss rate due to destructive interference between ground plate reflection and magnetic dipole radiation. (c) Strong magnetic dipoles are induced when G is small; (d) negligible magnetic dipoles are induced when G is large.

In earlier reports on MM absorbers, perfect absorption was explained in terms of matching the bulk metamaterial's impedance, $z = \sqrt{\mu_{eff}/\epsilon_{eff}}$, to that of vacuum [98, 89, 99, 100], where ϵ_{eff} and μ_{eff} are the effective permittivity and permeability of the bulk multi-layer (i.e., stacked in the vertical x direction) metamaterial. Typically, these effective constitutive parameters are obtained from the scattering matrices of either a single layer or multiple layers of the MMs [101] under the assumption of homogeneous media. To satisfy the condition of matched impedances, the condition of $\epsilon_{eff} = \mu_{eff}$ (which are both, in general, complex numbers) is achieved [98] by manipulating the spectral positions and strengths of the electric and magnetic resonances of the MMs. However, this viewpoint is not appropriate for MMs using a thick ground plate because the S-matrix is not fully defined when transmittance vanishes. Additionally, the ambiguity in the MM thickness also poses a problem in calculating ϵ_{eff} and μ_{eff} with the presence of a semi-infinite ground plate.

Here we explain the phenomenon of perfect absorption in terms of critical coupling to the MM surface. This perspective is more adequate for our situation with blocked transmission. It provides a guideline on how the structure should be designed, and also reveals the persistence of high absorbance over structural variation. Critical coupling occurs when a leaky eigenmode of the structure has equal resistive and radiative losses. For a critically coupled MM, an incoming field excites the eigenmode through radiative coupling, and the incoming energy transforms into resistive loss without generating reflection. Therefore, a MM absorber with blocked transmission is analogous to the single resonator coupled to a single input waveguide. This problem has been well-studied [1], and the reflection coefficient, r, can be expressed as a function of the resonant frequency, ω_0, the radiative damping/coupling rate, ω_{iR}, and the resistive

73

damping rate, ω_{iQ}, of the resonator. (add the expression for r). The impedance of the MM surface defined as $z = (1 + r)/(1 - r)$ is given by:

$$z = \omega_{iR}/[i(\omega - \omega_0) + \omega_{iQ}].$$ (6.1)

From Eq. (6.1), the critical coupling condition, $z = 1$, is satisfied when $\omega_{iR} = \omega_{iQ}$. Because the ground plate transmits no light, the absorptivity of the structure, $A(\omega)$, which is determined by its reflectivity according to $A \equiv 1 - |r|^2$, reaches unity at $\omega = \omega_0$. Note that $r(\hat{\omega})$ diverges at the complex frequency $\hat{\omega}$ if $z(\hat{\omega}) = -1$, or $\hat{\omega} = \omega_0 - i\,\omega_i$, where $\omega_i \equiv \omega_{iR} + \omega_{iQ}$. Because the divergence of the reflectivity corresponds to the eigenmode of the "leaky" resonator (or, in our case, leaky plasmonic absorber), we can calculate $\hat{\omega}$ by computing the complex eigenfrequency of the absorber. The corresponding plasmonic eigenmode is further used to break up the total decay rate, ω_i, into the Ohmic (resistive) and radiative parts. A similar approach [102] was recently used to describe critical coupling to surface polaritons excited in the Otto configuration.
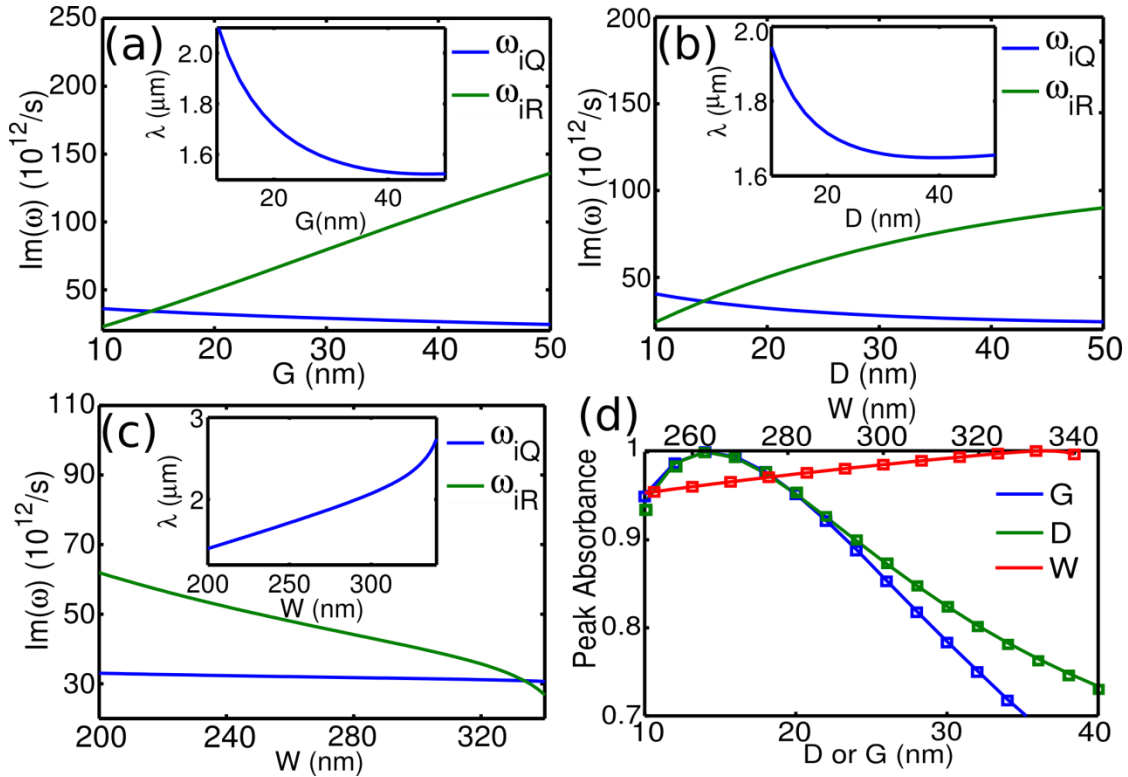
Figure 6.2: Resistive (ω_{iQ}) and radiative (ω_{iR}) loss rates of the eigenmodes as functions of (a) the dielectric gap size (G), (b) metal strip thickness (D), and (c) metal strip width (W). The parameters are varied around $L=350$ nm, $W=250$ nm, $D=20$ nm, and $G=20$ nm. Equal resistive and radiative loss rates correspond to critical coupling and perfect absorption. Insets: dependence of the resonant wavelengths of the corresponding eigenmodes. (d) Peak absorbance calculated from eigenmode (markers) and driven simulation (solid lines), with the parameters in the same range as (a-c).

The calculation was performed using the finite element method (FEM) software COMSOL Multiphysics. A single unit cell was modeled; periodic boundary conditions (BCs) in the y-direction (corresponding to the normal incidence) and radiative BCs in the x-direction were assumed in the simulation. The magnetic field distribution (color) and electric field vectors (arrows) of the most dominant (magnetic resonance) mode is shown in Fig. 6.4 (b). Both the strips and the ground plate are gold with dielectric permittivity

given by the Drude model: $\epsilon_{Au} = 1 - \omega_p^2/[\omega(\omega + i\gamma)]$, where $\omega_p = 1.32 \times 10^{16} \, s^{-1}$ and $\gamma = 1.2 \times 10^{14} \, s^{-1}$.

Using the COMSOL eigenmode solver, we can obtain both the eigenmode and the complex eigen-frequency, $\omega = \omega_r + i\omega_i$, associated with the eigenmode. We used the eigenmode to calculate the ohmic losses, W_Q, and the power out-flux, W_R, proportional to the Poynting vector. These quantities were then used in computing the resistive and radiative damping rates, ω_{iQ} and ω_{iR}, according to:

$$\omega_{iQ} = \omega_i \times \frac{W_Q}{W_Q + W_R} \, ,$$
$$\omega_{iR} = \omega_i \times \frac{W_R}{W_Q + W_R} \, . \tag{6.2}$$

These two quantities are required for calculating $z(\omega)$ from Eq. (6.1). The dependence of ω_{iQ} and ω_{iR} on the geometric parameters of the absorber are shown in Fig. 6.2.

According to Fig. 6.2 (a), the radiative loss associated with the eigenmode dominates over the resistive loss whenever plasmonic strips are separated from the ground plate by a large distance, G. Therefore, $|r(\omega)|$ of an external beam tuned to $\omega = \omega_0$ ($\lambda(G) = 2\pi c/\omega_0(G)$ is plotted in the inset) is large, and the absorbance is small, which is not surprising because the ground plate is highly reflective. On the other hand, if the strips are close to the plate, a strong image dipole moment is generated behind the ground plate as shown in Fig 6.1 (b). The resulting strong magnetic moment, $\vec{m}$, directed along the strips produces back-scattered fields with phase opposite to those produced by the reflection from the ground plate. Such destructive interference reduces the total backward scattering. With a suitable choice of G, critical coupling can be achieved when the scattering cross-section becomes equivalent to the resistive cross-section. Such cancellation does not occur for large Gs because electric field is mostly concentrated between the adjacent strips, not between the strips and the ground plate. Therefore, the magnetic moment is too weak to significantly reduce ground plate

76

reflection. Other geometric parameters also affect the total radiative loss. For a fixed periodicity L=350 nm, we observe from Fig. 6.2 that radiative loss can be decreased by increasing the strip width, W, or decreasing the strip thickness, D.

Assuming the single dominant resonance of the absorber, the peak reflectivity $|r(\omega)|^2 = |(z-1)/(z+1)|^2$ at the resonant frequency $\omega = \omega_0$ can be recast as:

$$|r(\omega_0)|^2 = |(\omega_{iQ} - \omega_{iR})/(\omega_{iQ} + \omega_{iR})|^2, \tag{6.3}$$

confirming that "perfect" peak absorption is achieved if $\omega_{iR} = \omega_{iQ}$. The peak absorbance, $A = 1 - |r(\omega_0)|^2$, obtained from Eq. (6.3) is plotted in Fig. 6.2 (d) (markers) and compared with the peak absorbance obtained from driven simulations (solid lines) for varying structure parameters. Excellent agreement is found between the single-pole impedance approach based on eigenvalue simulations and the driven simulations that include incident waves with frequencies scanned over a wide spectral range. The advantage of the eigenvalue-based approach is that only a single simulation is required to compute z and, therefore, the peak absorbance. A full frequency scan (i.e., multiple FEM simulations) is needed to find the peak absorbance using driven simulations.

One interesting consequence of Eq. (6.3) is that the absorbance can still be large even when the radiative loss is considerably mismatched from the resistive loss. For example, the absorbance still reaches 96 % when $\omega_{iR} = 1.5\,\omega_{iQ}$. We refer to this phenomenon as the persistence of high absorptivity despite considerable variations of the absorber's parameters. This insensitivity to the strip width, W, strip thickness, D, and strip-to-ground plate spacing, G, is shown in Fig. 6.2 (d): the absorbance stays above 70 % despite considerable variation (by as much as a factor of 4) of these parameters.
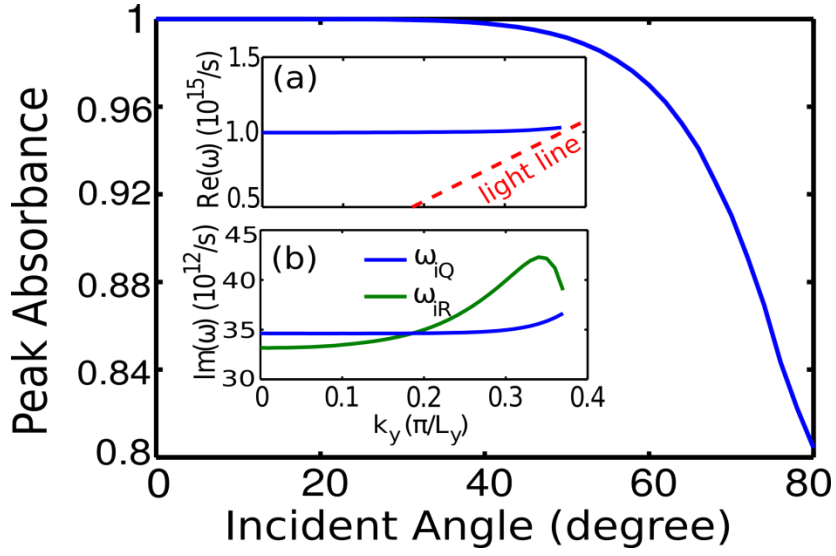
Figure 6.3. Angular dependence of the plasmonic resonance responsible for "perfect" absorption. (a) Peak absorbance remains above 80% for all incidence angles, θ. (b) Real and (c) imaginary parts of the eigenfrequency as a function of the wavenumber, $k_y = sin(\theta)\omega/c$, in the periodicity direction. The imaginary part is separated into radiative and Ohmic loss rates.

To investigate the angular response of the plasmonic absorber, we have computed eigenmodes and eigenfrequencies of "leaky" surface plasmons with a finite wavenumber k_y in the y-direction. As long as $ck_y < \omega$, such plasmons are "leaky" because they can directly couple to the radiation with the frequency ω incident at the angle $\theta = arcsin(ck_y/\omega)$ with respect to the (normal) x-direction. Therefore, they can be responsible for wide-angle absorption of the obliquely incident radiation. Just as for the normal incidence, one expects critical coupling and "perfect" absorption when $\omega_{iQ} \approx \omega_{iR}$. Indeed, as Fig. 6.3 indicates, the two damping rates are very close to each other. Moreover, the resonant wavelength $\lambda_0 = 2\pi c/\omega_0$ remains essentially flat for all values of k_y. The consequence of a flat response is persistently high absorbance (between 80 % and 100 %) of the plasmonic structure as the incidence angle, θ, is

78

varied in the $0° < \theta < 80°$ range. In Section~\ref{sec:spectroscopy}, we present experimental confirmation of wide-angle absorption.

6.3 FABRICATION OF THE ABSORBER

In this section we provide a detailed technical description of the fabrication procedure of the Large Area Wide-Angle Spectrally Selective Plasmonic Absorber (LAWASSPA). The structure was fabricated by Nanohmics using nano-imprint lithography [103, 97], which provides a means to create many replicate copies of devices via pattern transfer from a quartz master template that is initially defined using electron beam lithography (EBL). Once the EBL pattern is etched into quartz, the patterned quartz template is used to stamp photoresist layers under UV exposure (i.e., a step-and-flash process). Release of the quartz template leaves the desired relief pattern on the wafer surface. Subsequent dry etching transfers the pattern into the desired layer, which are thin gold strips in this work. The feature dimensions are limited only by the resolution of the initial electron beam process, which is 50 nm for the JEOL JBX6000 EBL tool at the University of Texas at Austin's Microelectronic Research Center (MRC). For volume production, resolution can be as low as 20 nm.

To fabricate the devices, Cr-Au-Cr layers (3 nm-94 nm-3 nm) were deposited on a 4" silicon wafer by electron beam evaporation. A layer of In_2O_3 (20 nm) followed by SiO_2 (1 nm) were deposited by PECVD as the dielectric spacer. An additional Cr-Au layer (3 nm-30 nm) was subsequently deposited on the dielectric spacer. Nano-imprint lithography is used to pattern the top Cr-Au layer into metal strips, which begins by spin-coating a layer of $TranSpin^{TM}$. A number of combinations of metal strip width W

(100-300 nm) and pitch L (175-450 nm) were patterned into the quartz template as 1.4 mm^2 islands, providing a range of peak absorbance wavelengths to investigate.

Nano-imprint lithography begins by dispensing curable liquid (silicon-based $MonoMat^{TM}$) with high precision over the desired area. The quartz master is pressed against the surface of the wafer (feature side down) and the $MonoMat^{TM}$ flows to fill the relief pattern in the quartz. Ultraviolet exposure sets the $MonoMat^{TM}$ and the quartz master is released from the surface leaving the imprinted pattern. After release, the residual $MonoMat^{TM}$ layer is dry etched by reactive ion etching (Oxford RIE, 200 V DC bias, 15 sccm CHF$_3$, 7.5 sccm O$_2$, 25 mtorr) followed by dry etching of the $TranSpin^{TM}$ layer (200 V DC bias, 8 sccm O$_2$, 5 mtorr). The pattern is transferred into the Au/Cr layer using a physical reactive ion etch in Ar (250 W, 50 sccm Ar, 40 mtorr). A final O$_2$ plasma etch (March Asher) was used to remove remaining $MonoMat^{TM}$ and $TranSpin^{TM}$, yielding the final device structure. An representative SEM image of the structure with L=300 nm and W=230 nm is shown in Fig. 6.4 (a). A single wafer contains a large number of LAWASSPA pixels with different unit cell sizes. Each pixel has the size of approximately 1 mm^2, and is tuned to a different resonant wavelength $\lambda_0 = 2\pi\, c/\omega_0$ determined by the unit cell's dimensions W and L.
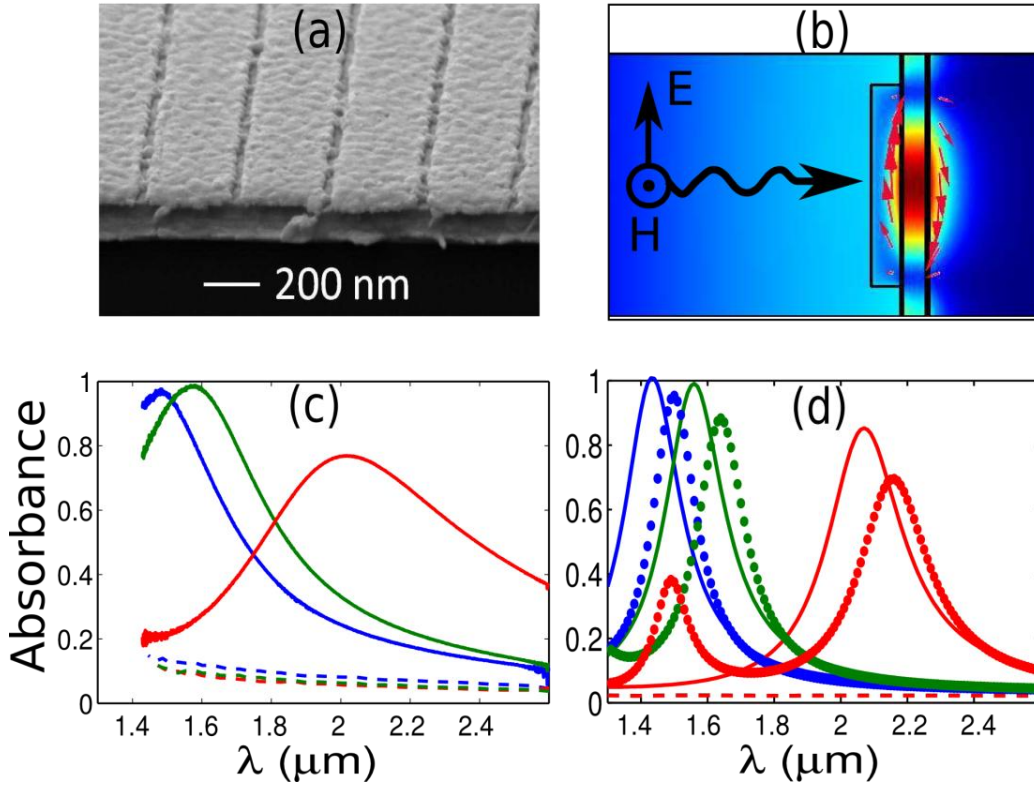
Figure 6.4. (a) SEM image of the strip absorber structure. (b) Simulated field profile at the resonance. Color: $|\vec{H}|$, arrow: $\vec{E}$ field. (c) Measured and (d) simulated absorbance with polarization perpendicular (solid lines) and parallel (dashed lined) to the strips. The dimensions are [L, W]=[300 nm, 230 nm] (blue), [330 nm, 250 nm] (green), and [450 nm, 350 nm] (red). D=30 nm and G=22 nm for all three cases. Incident beams are 25° P-polarized for both experiments and simulations. The dotted lines in (d) are predicted absorbencies for square patch arrays with identical parameters and normal incidence.

6.4 ANGLE-RESOLVED INFRARED SPECTROSCOPY OF WIDE-ANGLE PLASMONIC ABSORBERS

In this section, we experimentally demonstrate that (i) the absorption peak of the infrared plasmonic resonance can be spectrally tuned/controlled by changing the unit cell's dimensions as described in Section 6.2, and (ii) that the absorbance is wide-angle in

agreement with earlier theoretical calculations [94, 95, 96, 45] and with the theory presented in Section 6.2. To test (i), we have measured the reflection spectra from different LAWASSPA pixels fabricated on a single wafer as described in Section 6.3. Reflectance (R) spectra were collected with a Thermo Scientific Continuum microscope coupled to a Nicolet 6700 FTIR spectrometer using P-polarized radiation and a $2\ cm^{-1}$ wavenumber resolution in the $7000\ cm^{-1}$- $650\ cm^{-1}$ ($1.4\ \mu m$-$15.4\ \mu m$) spectral range. A wire-grid polarizer aligned the electric field polarization along the periodicity direction y as illustrated by Fig. 6.4 (b). Experimental absorbance for several LAWASSPA pixels of different dimensions is shown in Fig. 6.4 (c) by solid lines for the y-polarized infrared radiation. The incidence angle of the infrared beam on the sample is approximately fixed at $25°$ by microscope optics.

By changing the unit cell's dimensions W and L (see Fig. 6.1 for definitions), we have experimentally demonstrated spectral tunability of the plasmonic absorber between $\lambda_0 = 1.6\ \mu m$ and $\lambda_0 = 2.0\ \mu m$ for the y-polarized beam. Much smaller absorption measured for the orthogonal light polarization (electric field parallel to the long dimension, z, of the strips) shown in Fig. 6.4 (c) by the dashed lines does not exhibit any spectral selectivity. As expected, the strip-based plasmonic absorber is polarization-sensitive: it acts as a "perfect" absorber/reflector for the y/z-polarized beams.

Simulations were performed and compared with experimental results. In calculations, the Drude model for Au and the refractive index $n_{spacer} = 1.8$ for In$_2$O$_3$ were used. Theoretical absorption spectra plotted in Fig. 6.4 (d) for the same unit cell dimensions as the fabricated samples (solid lines) show good agreement with the experimental spectra plotted in Fig. 6.4 (c). To account for thin post-etching metal residue between the strips that was identified in SEM images, an extra 2 nm of Au on top of the spacer was assumed in calculations. The effect of this metal residue is a slight

blue-shifting of the resonance. While the extra metal layer was not intentional in this set of experiments, it could become a useful feature for specific applications that require electric contact between the metal strips of the absorber. Likewise, polarization selectivity of strip-based plasmonic absorbers could be useful for some applications (e.g., thermal infrared emitters with controlled polarization state) and detrimental for others (e.g., infrared photodetectors). Nevertheless, the results obtained for the strip-based absorbers are directly relevant to patch-based [45, 96] polarization-insensitive absorbers shown in Fig. 6.1 (b). Specifically, using COMSOL simulations, we have found that the absorptivity of an array of square patches is essentially identical to that of the infinite strips if the widths and periods (W and L) of these structures are chosen to be identical. The comparison between strip-based (solid lines) and patch-based (dotted lines) plotted in Fig. 6.4 (d) shows only a small systematic red shift of the latter with respect to the former. This observation is useful from the design standpoint because strip-based absorbers are much easier to simulate using two-dimensional FEM simulations. Strip-based absorbers provide an excellent starting point for designing fully three-dimensional patch-based plasmonic absorbers. We conclude that, while 2D strip arrays are easier to analyze and engineer, absorbers with both strip and square patch arrays show the same physics of critical coupling and high absorbance if their geometric parameters are near-identical.

If the structure is to be used as an effective absorber, the absorption rate must remain high for a wide range of incident angles. Because the spectra shown in Fig. 6.4 (c) were obtained using a fixed-angle geometry (IR microscope), a separate optical setup enabling variable-angle spectroscopy was used to test the wide-angle properties of the absorber. The beamline is based on the FTIR spectrometer and uses standard infrared focusing optics assembled on the optical table. It provides a means for variable incidence

83

angles, polarization control, and a $200 \, \mu m$ spot size. The geometric parameters of the strip-based LAWASSPA are given by [L, W, D, G]=[300 nm, 230 nm, 10 nm, 17 nm], and the dielectric spacer is SiO$_2$ ($n_{spacer} = 1.5$). Angle-resolved absorption spectra were measured for both S and P polarizations of the incident light as illustrated in Fig. 6.1 (a), and presented as a color map in Figs. 6.5 (a) and (b), respectively. Both polarizations exhibit a fairly wide-angle absorptivity, although P polarization is much less angle-dependent than S polarization. As was noted in earlier theoretical work [94], this dependence occurs because the plasmonic resonance responsible for "perfect" absorption is primarily magnetic and, therefore, is sensitive to the out-of-plane component of the magnetic field. The qualitative agreement between theory (Fig. 6.5 (c,d)) and experiment (Fig. 6.5 (a,b)) is excellent. Inhomogeneous broadening of the experimental spectra compared to theoretical predictions most likely results from the absorber's structural imperfections. However, as we have demonstrated, the absorber design is robust against imperfections, and therefore the absorptivity remains high. One unintentional but interesting feature of this absorber is that the absorption is not maximized at normal incidence. In fact, for P polarization, the measured absorbance peaks at $A = 96 \, \%$ for $\theta = 70°$ and drops to $A = 87 \, \%$ for $\theta = 20°$.
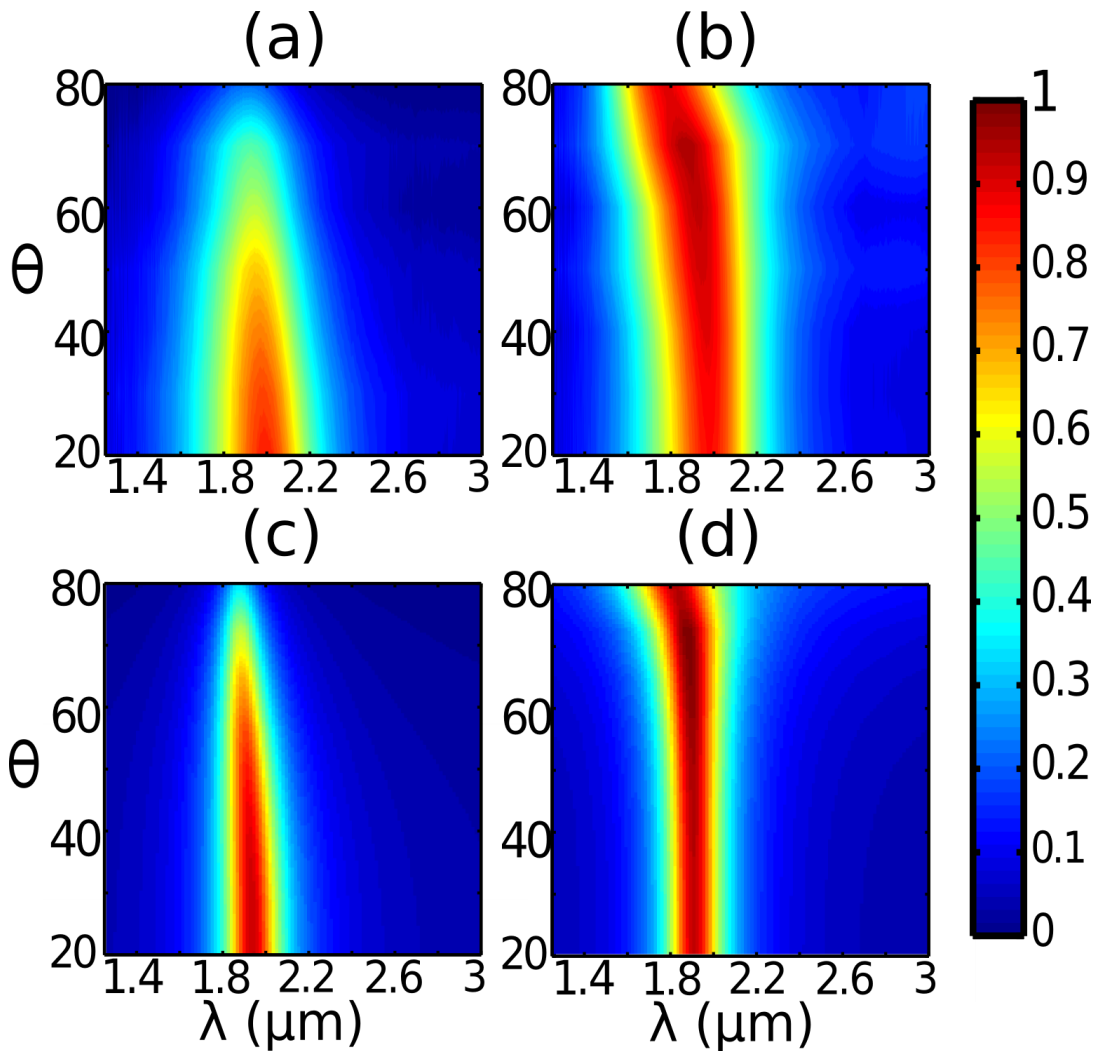
Figure 6.5: Angular-resolved absorption spectra, $A(\theta, \lambda)$, for the strip-based plasmonic absorber shown in Fig.~\ref{fig:experiment}. The measured absorbance with (a) S- and (b) P-polarized incidence (illustrated in Fig. 6.1 (a)) is given in the upper panel, and the calculated absorbance with (c) S- and (d) P-polarized incidence is given in the lower panel.

6.5   DESIGN OF SMALL-PIXEL INFRARED ABSORBERS

In this section, we discuss the implications of the wide-angle absorptivity of the infrared plasmonic absorbers. One of the consequences of wide-angle absorptivity is that

the coherence propagation length l_c of the surface plasmon responsible for the absorption is very short. If $l_c \leq L$, then the interaction between the adjacent unit cells is small. Therefore, one can envision combining a very small number of unit cells into a micro-pixel which can be as small as one wavelength across. Such micro-pixels can act as an independent absorber/emitter. One possible application of such micro-pixels could be a large focal plane array (FPA) for hyper-spectral imaging. Such an array would consist of macro-pixels comprised of several micro-pixels, each of which is tuned to a different wavelength. For example, a macro-pixel comprised of a 5×5 micro-pixels of width $w_j = \lambda_{0j}$ (where $1 < j < 25$) would be capable of monitoring 25 different wavelengths while remaining relatively small. The small size (several wavelengths across) of a macro-pixel is essential for imaging/surveillance with a small angular resolution.

Our experimental data indeed indicates that $l_c < L$ and, therefore, the adjacent unit cell have very little cross-talk between them. Quantitative estimate of the propagation length can be obtained from the angular dependence of the absorptivity, $A(\omega, k_y)$, which is plotted in Fig. 6.5 as a function of the related variables $\lambda = 2\pi c/\omega$ and θ. The propagation length along the y-direction is given by $l = v_g \tau$, where $v_g = \partial \omega_0 / \partial k_y$ is the group velocity in the y-direction, and τ is the lifetime of the resonant mode that can be estimated as $\tau \approx A^{-1} \partial A/\partial \omega$. Assuming that the absorption rate is maximized at the angle-dependent eigenfrequency, $\omega_0(k_y)$, and that the peak absorption rate remains close to unity ($A(\omega_0, k_y) \approx 1$), we find that $|v_g| \approx |(\partial A/\partial k_y)/(\partial A/\partial \omega)|$. Combining these expressions for τ and v_g, and by assuming that $A \approx 1$, we obtain the following simple estimate for the propagation length: $l_c \approx |\partial A/\partial k_y|$. By noting that $ck_y = \omega \sin(\theta)$, we estimate the maximum plasmon propagation length as $l_c < (\lambda/2\pi) \, max \, [\partial A/\partial \cos(\theta)]$. From the experimental data

for the wide-angle absorber, we estimate that the propagation length cannot exceed $l_c < 300$ nm, i.e., about one period. Therefore, a resonant mode in a single cell is significantly damped before reaching adjacent unit cells, and the cross-talk between them is small.

To substantiate our claim that the unit cells of the MM absorber function independently, the absorbance of a limited number of MM unit cells is investigated theoretically. In Fig. 6.6, we consider an incoming Gaussian beam with an intensity FWHM of $2.6\,\mu m$ impinging on MM surfaces consisting of 4, 8, 12, and 16 unit cells. The unit cells possess $[L,\ W,\ D,\ G]$ = [350 nm, 250 nm, 20 nm, 14 nm]. The metal is Au and the spacer is SiO_2. Figure 6.6 (a) shows absorbance with different numbers of unit cells, whereas in Fig. 6.6 (b) the peak absorbance is compared to the incoming flux within the structured area. It is shown from the comparison that the MM absorber remains perfect absorbing to the incident flux, even though the incoming field is not planar and the MM consists of as few as four unit cells. This property can find applications in thermal imaging, where a pixel can be defined by a small number of MM unit cells. On-chip spectrometers are also envisioned, in which MM absorbers tuned to different wavelengths are patterned side-by-side on a single chip.
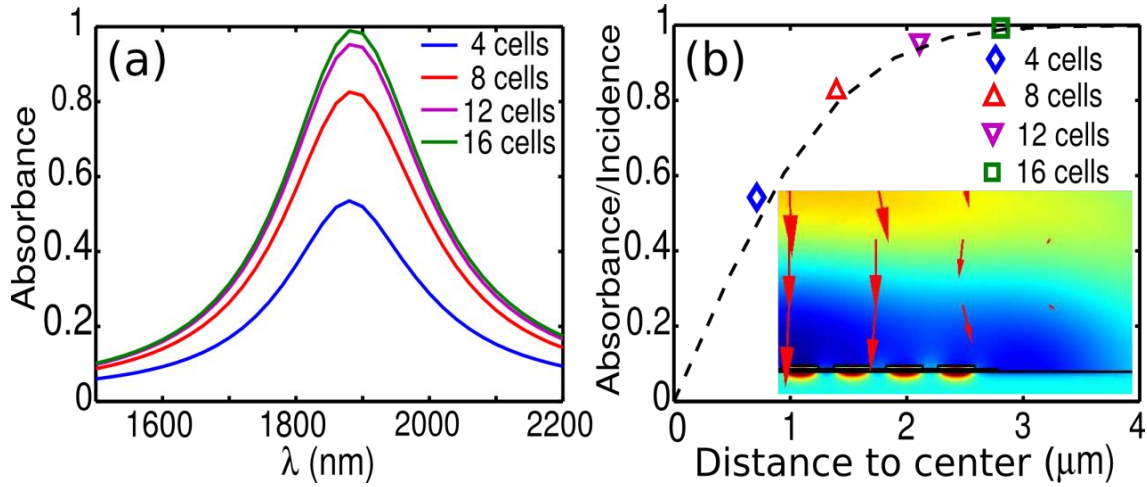
Figure 6.6: (a) The absorbance by a finite number of unit cells illuminated by a Gaussian beam with an intensity FWHM of 2.6 μm. (b) Peak absorbance versus patterned-area width. Dashed line: fractional overlap between the patterned area and the laser beam. Inset: a simulation of eight unit cells (only half are shown) under the incoming Gaussian beam. Color: out-of-page magnetic field, arrows: Poynting flux.

CONCLUSIONS

In conclusion, we have demonstrated a simple design of an ultra-thin, wide-angle plasmonic absorber exhibiting spectrally selective near-unity absorption. The high absorbance of the structure is described in terms of critical coupling, where the scattering cross-section is equal to the absorptive cross-section. The critical coupling perspective provides a guideline for designing MM absorbers with tunable resonant frequencies: with low loss metals, the structure should be designed in such a way that the resonances have low radiative loss. Based on this theory, the gold strips and ground plate in this simple structure can be replaced by other metals, e.g., tungsten for high-temperature applications, and the dielectric spacer layers can be replaced by absorbing materials, e.g., semiconducting materials for photovoltaic applications. We have also developed a

convenient tool for designing such structures based on the eigenvalue simulations of the "leaky" plasmon resonances. These simulations are used for calculating the impedance of the absorbing surface at arbitrary frequencies, which can then be used for predicting absorbance and reflectance. Because a number of applications require inexpensive, large-area plasmonic absorbers, the fabrication approach is paramount. We have fabricated plasmonic absorbers using step-and-flash ultraviolet nano-imprint lithography, which has the advantages of reusable masks and large-area fabrication compared with the serial fabrication methods. By patterning absorber pixels of various dimensions over a large area, we have experimentally demonstrated that the spectral response of the absorber can be controlled over a wide wavelength range ($1.5\,\mu m < \lambda < 2.0\,\mu m$) while maintaining a near-unity peak absorbance. Using angle-resolved infrared spectroscopy, we have experimentally demonstrated that these Large-Area, Wide-Angle, Spectrally Selective Plasmonic Absorbers (LAWASSPA) exhibit near-unity absorptivity for incidence angles from 20° to 80°. Moreover, we have experimentally demonstrated and theoretically validated that P-polarized light exhibits wider-angle absorption than S-polarized light. Such wide-angle absorption indicates short propagation lengths (less than one unit period) of the plasmonic mode, a feature useful in designing ultra-small (one wavelength across) absorbing pixels that can be used as building blocks for hyper-spectral focal plane arrays and infrared emitters.

Chapter 7

Designing Meta-surfaces with Broadband Absorption Using the Surface Impedance Model

7.1 INTRODUCTION

Plasmonic metamaterials (MMs) are subwavelength metallic nanostructures designed to provide extraordinary electromagnetic properties in specified frequency ranges [104, 105]. The combination of the plasmonic response of conduction electrons and appropriate (but not necessarily geometrically complicated) design of the structures results in subwavelength feature sizes and strong near-field enhancement. These properties pave the way to various applications, such as surface enhanced Raman scattering [32, 106], light trapping [107], bio-molecule sensing [82], and plasmonic absorbers. For the reasons going beyond the simplicity of fabrication, many applications utilize MM surfaces instead of MMs. For example, MM surfaces provide solid/liquid interfaces for bio-sensing, or can be used as ultra-thin coatings to provide spectrally-selective optical properties (e.g, absorption). Simple designs of narrow-band MM absorbers (NBMA) comprised of an array of plasmonic strips/patches separated by a thin dielectric spacer from a ground plate, as illustrated in Fig. 7.1 (a), have been demonstrated both theoretically and experimentally [94, 95, 96, 45, 108], "Perfect" (100% at the peak) light absorption by NBMAs is enabled by the resonant excitation of a surface plasmon polariton (SPP) whose frequency is controlled by the structural dimensions.

A straightforward strategy of constructing a broad-band metamaterial absorber (BBMA) using different NBMAs has been conceived [109, 110]: combining several

NBMAs ($i = 1 \ldots N$) with spectrally-close absorption peaks at $\omega_0^{(i)}$ and bandwidths $\Delta\omega_0^{(i)}$ into a macro-cell should deliver the desired broad-band feature as long as $\left|\omega_0^{(i+1)} - \omega_0^{(i)}\right| < \Delta\omega_0^{(i)}$. In reality, designing BBMAs using this approach has been challenging. For example, the individual absorption peaks of the constitutive NBMAs can each yield "perfect" absorption, but at the expense of large spectral separation. Alternatively, constitutive NBMA's with spectrally-close absorption peaks can fail to provide "perfect" absorption at every peak. Systematic approach to designing NBMAs and combining them into a unit cell of a BBMA is needed. In this Chapter, we provide such an approach based on a simple impedance model. We show that the surface impedance, z, of a BBMA can be obtained from the impedances, z_i, of the constitutive NBMAs using a simple additive formula (see Eq. (7.3)), which is valid as long as the SPPs' propagation lengths are much smaller than the separation between NMBAs.

7.2   THE COUPLED MODEL WITH A RESONATOR BACKED BY A REFLECTOR

We start by introducing a simple single-resonance model of an NMBA based on the periodic structure shown in Fig. 7.1 (a). The structure coupled to the incident radiation is described within the framework of a single resonator model [1]. An open resonator is defined by its natural frequency, ω_0, and finite lifetimes, $\tau_o = 1/\omega_{io}$ and $\tau_e = 1/\omega_{ie}$, respectively determined by the Ohmic and radiative losses. The interaction between the resonator and the incident field of amplitude E_I is described by the following equations:

$$\frac{d}{dt}a = -i\omega_0 a - (\omega_{io} + \omega_{ie})a + \sqrt{2\omega_{ie}}E_I ,$$

$$E_R = -E_I + \sqrt{2\omega_{ie}}a \qquad\qquad (7.1)$$

where a and E_R are the amplitudes of the resonator and the reflected field, respectively. The specific geometry of the resonator that includes the ground plate is manifested in the expression for E_R, which is a superposition of the resonator re-radiation, $\sqrt{2\omega_{ie}}a$, and the ground plate reflection, $-E_I$. Within this simple single-resonance model, the surface impedance defined as $z \equiv (1+r)/(1-r)$, where $r = E_R/E_I$, is given by:

$$z = \frac{\omega_{ie}}{-i(\omega - \omega_0) + \omega_{io}},\qquad(7.2)$$

and all optical properties of the NBMA are determined by three parameters: ω_0, ω_{ie}, and ω_{io}. These parameters depend on the structural dimensions and can be obtained by calculating the "leaky" SPP eigenmodes using eigenvalue simulations (i.e., no incident field) as demonstrated in Chapter 6. By tuning the geometric parameters of the NBMA, one can engineer ω_0, ω_{ie}, and ω_{io} and achieve $z = 1$ (and therefore perfect absorption) whenever the critical coupling condition, $\omega_{ie} = \omega_{io}$, is satisfied. The accuracy of the $z(\omega)$ obtained from Eq. (7.2) using the eigenmodes was verified against the impedance calculated from the reflection coefficients using $z \equiv (1+r)/(1-r)$ at various frequencies, ω, of the incident radiation. Plasmonic strips and ground plate are described by the Drude permittivity of gold with $\epsilon_{Au} = 1 - \omega_p^2/[\omega(\omega + i\omega_c)]$, where $\omega_p = 1.32 \times 10^{16}\ rad/s$ and $\omega_c = 1.2 \times 10^{14}\ rad/s$. The spacer is assumed to have a non-dispersive dielectric permittivity with $\epsilon_d = 2.25$. Excellent agreement shown in Fig. 7.1 (b) validates the single-frequency model, which is highly computationally efficient because only a single eigenvalue/eigenmode simulation is required [108] to determine $z(\omega)$ for all frequencies. The tunability of the NBMA's frequency characteristics $(\omega_0, \omega_{ie}, \omega_{io})$ with respect to the spacer thickness, G, is illustrated in Fig. 7.1 (b). Note from Fig. 7.1 (b) that considerable peak absorbance (in excess of 90%) is achieved for a wide range of spacer thicknesses $10\ nm < G < 20\ nm$. The smooth

dependence of the frequency characteristics on G shown in Fig. 7.1 (b) (as well as on the other structure parameters) enables rapid design of the appropriate parameter set (W, L, G, D) of the NBMA that provides the targeted ($\omega_0, \omega_{ie}, \omega_{io}$).
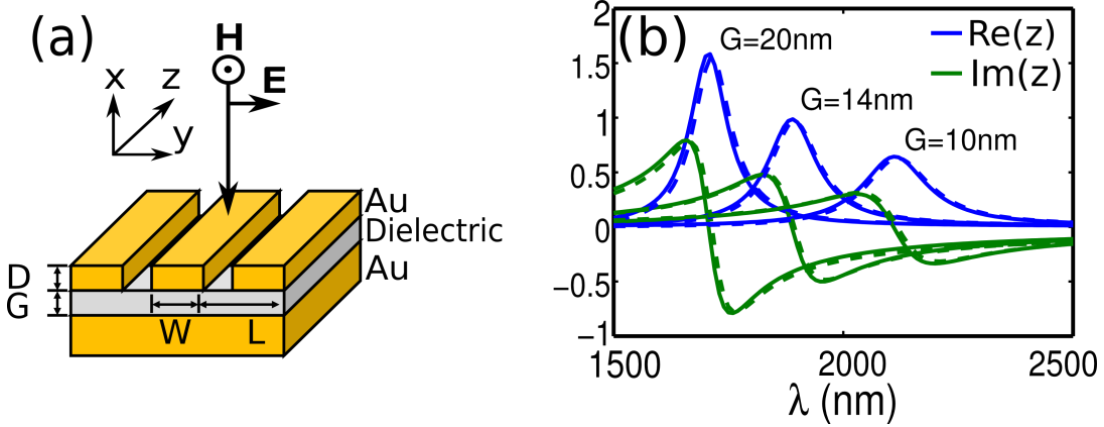
Figure 7.1: (a) Schematic of the Narrow Band Metamaterial Absorber (NBMA). (b) Impedances of NBMAs for 3 values of G. Solid lines: from driven simulations, dashed lines: from the single oscillator model.

7.3 THE SERIES IMPEDANCE MODEL FOR BBMA

Two important features of the NBMAs make them promising building blocks for designing a BBMA. First, their period is strongly sub-wavelength: $L_i \ll \lambda_0^{(i)} \equiv 2\pi c / \omega_0^{(i)}$. That implies that a sub-wavelength ($L = \sum_i L_i \leq \lambda$) unit cell of a BBMA can accommodate a large number of NBMA-based sub-units satisfying $L_i \ll L \leq \lambda$. Second, the propagation length, $l_{SPP}^{(i)}$, of the SPP responsible for absorption satisfies $l_{SPP}^{(i)} < L^{(i)}$. This property has been shown in Chapter 6 to be related to the wide-angle absorbance of the NBMA. While these two conditions are related, they are not equivalent as shown

93

below. Nevertheless, when both conditions are satisfied, a simple expression for the surface impedance of a BBMA with a macro-cell composed of N NBMA's can be obtained:

$$z = \sum_{i=1}^{N} z_i L_i / \sum_{i=1}^{N} L_i, \qquad (7.3)$$

where z_i (L_i) is the impedance (period) of each periodic constitutive NBMA. Derivation of Eq. (7.3), based on the series combination model [111], is illustrated in Fig. 7.2 (a), where the external field represents a voltage drop and each NBMA resonator is treated as a circuit element. The key assumption is that each component of the circuit functions independently from each other, i.e., there is little mutual capacitive or inductive coupling between adjacent sub-units. This condition is satisfied owing to the second feature of NBMAs, i.e., $l_{SPP}^{(i)} < L^{(i)}$. Below we verify Eq. (7.3) for two cases: (i) strongly (Fig. 7.2 (b,c)) and (ii) weakly (Fig. 7.2 (d,e)) confined SPPs of the individual sub-units. In each case the unit cell of a candidate BBMA consists of two sub-units with dimensions stated in the caption of Fig. 7.2.

In case (i), excellent agreement between BBMA's impedance calculated from Eq. (7.3) and from direct numerical simulations is shown in Fig. 7.2 (b). Each sub-unit, representing a resonant high-impedance ($z_{1,2} \approx 2$) surface, is independent of the other inside the macro-cell because $l_{SPP} \approx 360\,nm < L_{1,2}$. The impedance of the combined candidate BBMA has two spectral peaks with values $z \approx 1$ corresponding to 100% absorption, in accordance with the prediction by Eq. (7.3). On the other hand, Eq. (7.3) clearly fails in case (ii) as shown in Fig. 7.2 (d). That is because $l_{SPP} \approx 705\,nm > L_i$, and the two sub-units strongly interact inside the macro-cell, thereby invalidating the series impedance model. Note that to achieve such long propagation length of the SPP in case (ii), the electron collision frequency, ω_c, in Au has been artificially reduced by a

factor of four. We've tested Eq. (7.3) on a recently proposed BBMA structure with a germanium spacer [110]. Excellent agreements with the series combination model were found even with deeply subwavelength dimensions of the sub-units ($\lambda/L \approx 6.5$).
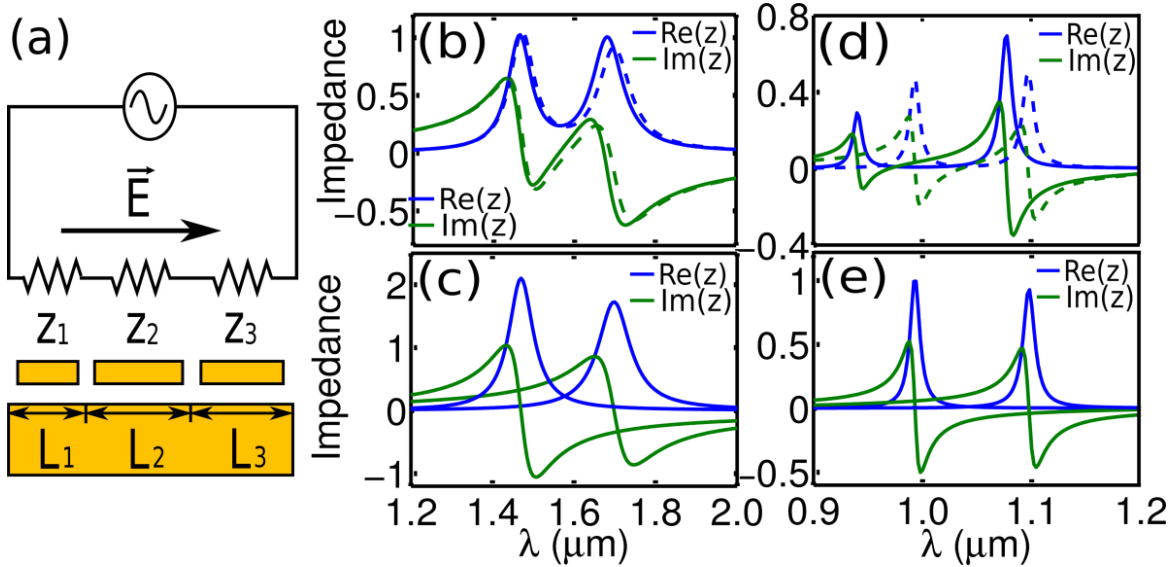
Figure 7.2: (a) Illustration of the circuit model used to derive Eq. (7.3). (b,d) The impedance, z, of the resonant surface with a macro-cell comprised of two sub-units. Sub-unit dimensions: (b) $[L_1, L_2, W_1, W_2] = [407\text{nm}, 383\text{nm}, 268\text{nm}, 227\text{nm}]$ and $[D,G]=[17\text{nm}, 28\text{nm}]$; (d) $[L_1, L_2, W_1, W_2] = [432\text{nm}, 371\text{nm}, 409\text{nm}, 356\text{nm}]$ and $[D,G]=[13\text{nm}, 15\text{nm}]$. Solid lines in (b,d): z calculated from direct simulations; dashed lines: z calculated from Eq. (7.3), with individual impedances, $z_{1,2}$ plotted in (c,e), respectively.

7.4 DESIGNING THE BBMA

We now present two examples of BBMAs constructed by engineering their unit cells from several (two in Fig. 7.3 (a,c) and three in Fig. 7.3 (b,d)) NBMA sub-units. We use the example of two sub-units inside the unit cell of a BBMA to describe the computational procedure for obtaining an absorber with two 100% absorption peaks at

the prescribed frequencies ω_1 and ω_2. That corresponds to $z(\omega_1) = z(\omega_2) = 1$, where $z(\omega)$ is calculated from Eq. (7.3). The resulting four equations (note that z is a complex number) must be satisfied for four unknown. For simplicity, we assume $D_1 = D_2$ and $G_1 = G_2$ to be fixed. This leaves the complex impedance, $z = z(L_1, L_2, W_1, W_2)$, as a function of four unknowns that can be numerically solved for to satisfy the above four equations. The numerical implementation based on the multi-dimensional Newton's method is greatly simplified by the variables' separation in Eq. (7.3): the number of partial derivatives, $\partial z/\partial L_i$ and $\partial z/\partial W_i$, is reduced because $\partial z_i/\partial (L,W)_j = \delta_{i,j} \partial z_0/\partial (L,W)$, where z_0 is the impedance of one single sub-unit.
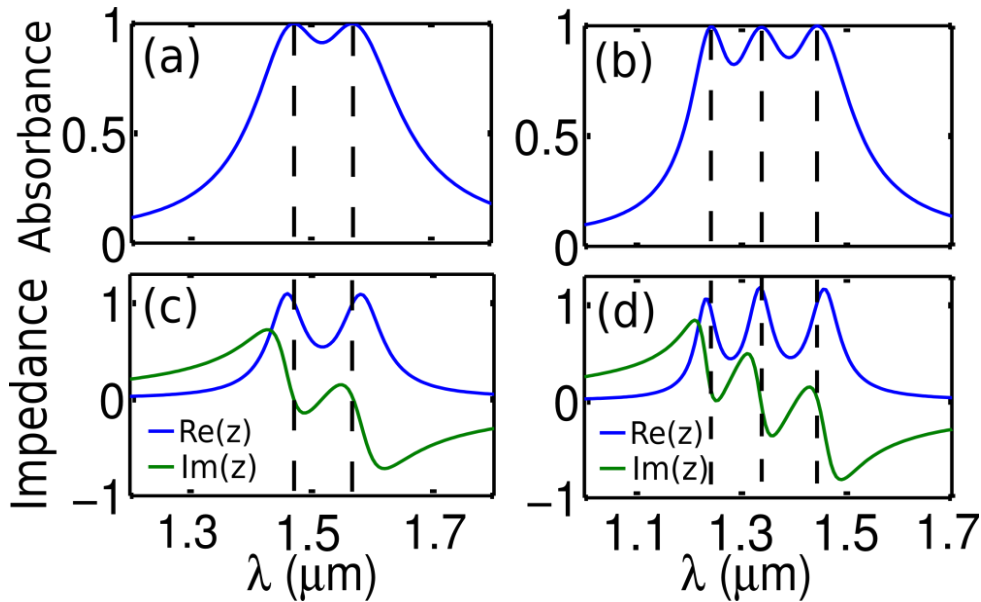
Figure 7.3: The absorption spectrum (top row) and the surface impedance (bottom row) of the designed Broad Band Metamaterial Absorbers (BBMA) with two (left column) and three (right column) sub-units per unit cell. Sub-units dimensions: $[L_1, L_2, W_1, W_2] = [448\text{nm}, 348\text{nm}, 249\text{nm}, 226\text{nm}]$ in (a,c); $[L_1, L_2, L_3] = [327\text{nm}, 280\text{nm}, 271\text{nm}]$ and $[W_1, W_2, W_3] = [224\text{nm}, 200\text{nm}, 180\text{nm}]$ in (b,d). Metal and spacer thickness given by $[D, G] = [17\text{nm}, 28\text{nm}]$ remain the same for all sub-units shown here.

The results of such numerical calculations for a BBMA with two sub-unit per unit cell are shown in Fig. 7.3 (left column), where the resulting double-peaked impedance, z, is plotted in Fig. 7.3 (c) and the corresponding frequency-broadened absorptivity is plotted in Fig. 7.3 (a). A similar numerical procedure was employed to design a triple-peaked BBMA illustrated in Fig. 7.3 (right column; all sub-unit parameters in the caption). Over 90% absorptivity is achieved in average over the spectral range of $1.2\ \mu m\ <\lambda\ <\ 1.5\ \mu m$. Note that in both examples presented in Fig. 7.3, the periodicity $L_{BBMA} = \sum_i L_i$ of the BBMA is sub-wavelength: $L_{BBMA} < \lambda$. It is essential to satisfy this condition to avoid the emergence of the additional diffraction orders which create additional radiative loss channels and further complicate the impedance model. In practice, this sets a limit on the attainable bandwidth. For example, for the strip-based designs presented in this Letter, the number of sub-units is limited to 3 (or 9 for a patche-based design). A possible solution could involve an aperiodic distribution of sub-units. Based on negligible interaction between the sub-units, it is expected that Eq. (7.3) should still hold.

In conclusion, we have demonstrated that a broad-band metamaterial absorber (BBMA) can be designed by constructing a super-lattice structure with each sub-lattice absorbing at different frequencies. Based on a single oscillator model and a series circuit model, broad-band absorbers with multiple perfectly absorbing peaks are shown to be attainable, and a procedure for designing such absorbers is provided. Examples of BBMAs comprised of two and three sub-units operating in the telecommunications frequency range are presented, and an average 90% absorbance in the $1.2\ \mu m\ <\lambda\ <$ $1.5\ \mu m$ range is predicted. Such ultra-thin (<100 nm) BBMAs can be used for infrared detection and other applications.

Chapter 8

Metamaterial-Based Integrated Plasmonic Absorber/Emitter

for Solar Thermophotovoltaic Systems

8.1   INTRODUCTION

Plasmonic nanostructures have been shown to possess extraordinary optical properties such as negative reflective index [112, 113, 85, 86] and indefinite permittivity [104, 105], and have been implemented in numerous applications across various disciplines. Examples include surface enhanced Raman spectroscopy (SERS) [32, 106], surface enhanced infrared absorption (SEIRA) spectroscopy [34], photothermal cancer therapy [114, 115, 116], and solar energy harvesting [107], to name a few. In the case of solar energy collection using photovoltaic (PV) cells, light trapping and enhanced absorbance by surface plasmons have been suggested [117, 118]. The main challenge with direct utilization of plasmonic resonance absorption of solar energy in the visible range is significant Ohmic losses and heating. Moreover, the Shockley-Queisser (SQ) limit [119] restricts the solar cell efficiency even when Ohmic heating from plasmonic dissipation is neglected. Because not all energy of the solar spectrum can be used to generate electron-hole pairs, the ultimate limit is about 44 % for semiconductors with $E_g = 1.1$ eV bandgap, and lower still for smaller values of E_g.

An attractive route to avoid the consequences of plasmonic overheating from direct visible absorption is to utilize solar thermo-photovoltaics (STPV). Fig. 8.1 illustrates the concept of an integrated Solar Absorber/Narrow-band Thermal Emitter (SANTE) film based on large-area nanoimprint-patterned plasmonic structures. Fig. 8.1 (a) illustrates the structure of the SANTE film which consists of a high melting temperature dielectric (e.g. AlN) deposited on a refractory metal foil such as tungsten.

A top metal layer can be patterned using methods such as nanoimprint lithography discussed in Chapter 6 to selectively tune the thermal emission properties of the film. Large-area devices fabricated using methods such as roll-to-roll imprint lithography will provide a means to construct STPV systems such as depicted in Fig. 8.1 (b). In this illustration, concentrated solar radiation is directed to a cylindrical core wrapped with the SANTE film. Broad-band absorption of the solar radiation is re-emitted from the SANTE film into a narrow IR band determined by the structure dimensions of the imprinted plasmonic structures. The emitted narrow-band IR radiation can be efficiently coupled into a separate PV cell positioned coaxially with the SANTE film to maximize power conversion efficiency. The performance of the STPV system is regulated by the efficiency of the total solar spectrum absorptivity and the coupling efficiency of the narrow-band thermal radiation into the PV cell. The advantage of the STPV approach illustrated in Fig. 8.1 lies in the ability to engineer SANTE film structure feature dimensions to select specific thermal emission properties. An STPV system operating in the mid-IR range enables plasmon-enhanced absorption with a substantial reduction in ohmic losses. Tuning of the emission frequency and emission spectral bandwidth to match the bandgap of the PV cell can dramatically improve the cell power conversion efficiency [120, 121].

Most STPV systems rely on separate absorbing and emitting surfaces [122, 121]. The absorbing structure provides close to 100 % absorption of solar radiation (primarily UV, visible, and near-infrared). Several surface designs based on corrugated dielectric or metallic gratings [123, 124] have been shown to provide uniformly high absorption across the solar spectrum. The emitter is typically [121] a resonant structure or material (e.g., Er-YAG) with narrow-band infrared absorption and, by virtue of Kirchhoff's Law, a commensurate emission that can be tuned to match the bandgap E_g of the PV cell. A

typical infrared emitter cannot function as an efficient absorber because it does not provide high light absorption in the solar range. Having a monolithic engineered surface functioning as both the integrated solar absorber and narrow-band thermal emitter will add a number of benefits to the overall STPV system design. To our knowledge, such surfaces have not been described previously. In this paper, we introduce the concept of a monolithic SANTE structure using a metamaterial-inspired design. The SANTE structure is based on previously published works [108, 98, 45, 96] for ultra-thin, narrow-band, wide-angle infrared absorbers using low-loss (high reflectivity) metals (e.g., Ag or Au). The primary difference is replacement of the high reflectivity metals with high-loss (low reflectivity) refractory metals (e.g., W or Mo). The optical properties of the refractory metals and high reflectivity metals are similar in the infrared, but display substantial differences in the UV/visible (solar) spectrum. Because the optical properties are different in the two regions, the design of plasmonic-coupled nanostructures that combine broad-band visible (solar) absorbance with narrow-band thermal emissivity in the infrared is possible.

The   plasmonic structure is based on a two-dimensional array of square features that are separated from a conducting ground plane (typically a metal foil) by an ultra-thin spacer layer with electrical properties ranging from insulating up to semiconducting [108, 98, 45, 96]. In the SANTE device, the top layer consists of a patterned refractory metal (tungsten), whose feature dimensions define the plasmonic coupling frequency and narrow-band emission. Two designs with the emissivity peaks tuned to $\lambda \approx 2.5\ \mu m$ (see Fig. 8.1: lower-temperature emission) and $\lambda \approx 1.9\ \mu m$ (see Fig. 8.2: higher-temperature emission) are presented. To highlight the thermal insulation capability of the SANTE film, its equilibrium temperature is calculated as the function of the solar concentration and compared with that of a black body emitter. The experimental test of the wide-angle

100

infrared absorptivity of the SANTE film based on a one-dimensional array of gold strips using angle-resolved Fourier transform infrared (FTIR) spectroscopy is described in Chapter 6. The overall efficiency of an STPV system based on tungsten SANTE film is calculated in Section 8.3 and shown to exceed the SQ limit for single-junction PV cells.
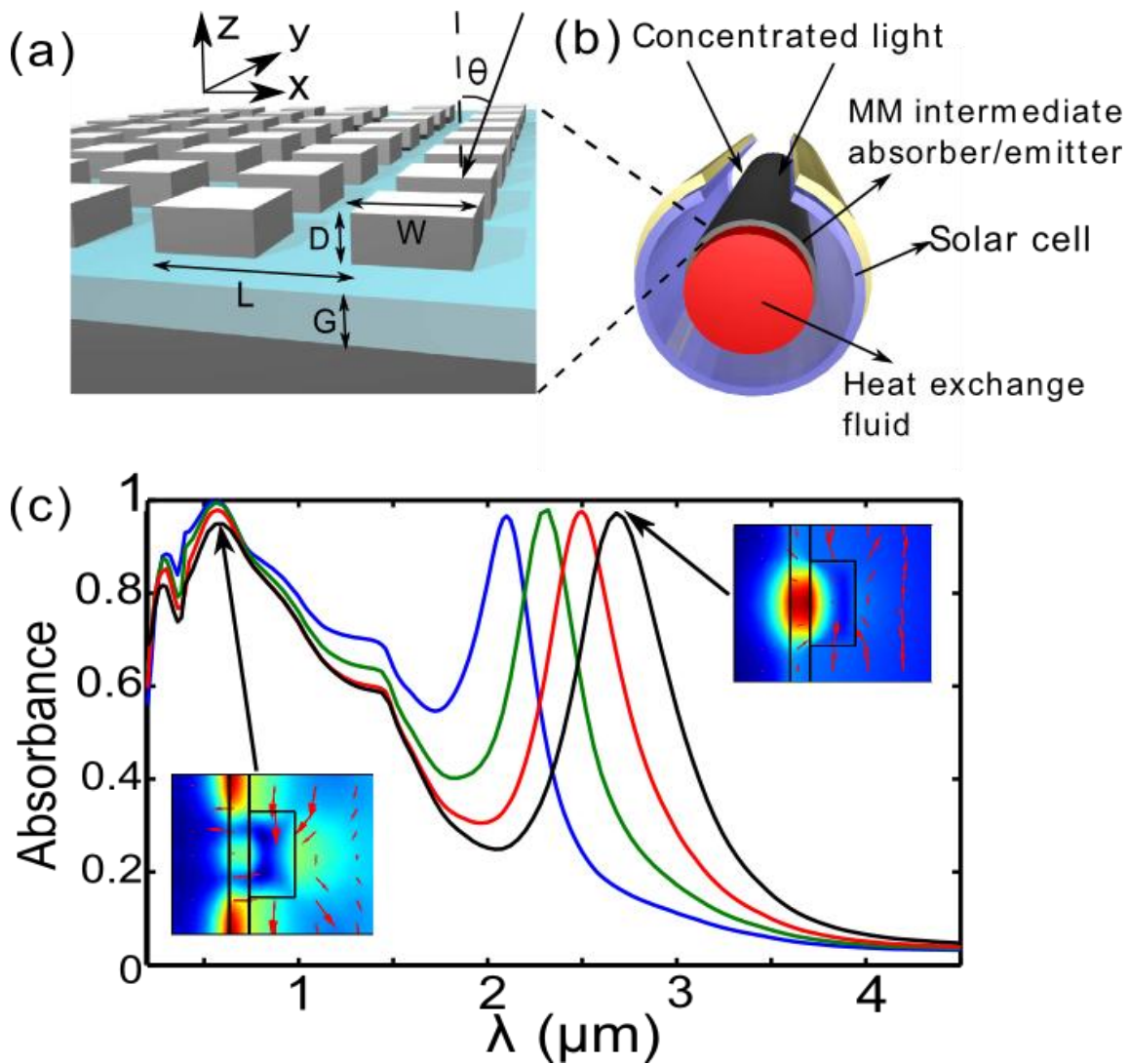
Figure 8.1: (a) Schematic of the Solar Absorber/Narrow-band Thermal Emitter (SANTE) structure. Gray regions: low reflectivity refractory metal (e.g., tungsten or molybdenum); light blue regions: dielectric spacer with high melting temperature (e.g., aluminum nitride). (b) Conceptual schematic of the overall STPV system employing the SANTE and a heat exchange fluid to extend the power-generating period beyond the daytime. (c) Calculated absorbance spectra of the SANTE structure for several geometric sizes (in nm): [Pitch (L), Width (W), Feature Depth (D), Dielectric Depth (G)]=[383, 206, 83, 27] nm (blue), [393, 230, 79, 24] nm (green), [404, 252, 73, 23] nm (red), and [396, 269, 72, 22] nm (black). Insets: field profiles for peak absorption frequencies. Color: out-of-plane magnetic field, arrows: in-plane electric field.

8.2 **SOLAR ABSORBER/NARROW-BAND THERMAL EMITTER FILMS**

The visible absorption of the SANTE film is used to collect solar energy and to heat the structure. The mid-IR absorption peak is utilized for achieving spectrally selective thermal emissivity $E(\lambda, T_e)$ by virtue of Kirchhoff's Law: $E(\lambda, T) = E_{BB}(\lambda, T_e) \times \langle A(\lambda, \theta, \phi) \rangle$, where $E_{BB}(\lambda, T_e)$ is the black-body emissivity spectrum at temperature T_e and $\langle A(\lambda, \theta, \phi) \rangle$ is the angle- and polarization-averaged absorption spectrum of the SANTE surface. For STPV applications, it is essential that the materials can withstand high temperatures (at least up to 1500 K). In this paper, we based our models on the assumption that the metal layers are tungsten (W) and the spacer is aluminum nitride (AlN). Because the SANTE device is designed to absorb visible (solar) radiation, the film will become heated. The heated device will, in turn, re-emit a majority of the energy via a narrow mid-IR spectrum dictated by the plasmonic structure feature dimensions. One possible geometry for fabricating an STPV system with a SANTE film is illustrated in Fig. 8.1(b). In this geometry, the SANTE film is wrapped around a cylindrical core heat exchange element. A standoff coaxial shield with an opening slit permits concentrated solar radiation to illuminate the SANTE film and core. Absorbed radiation is converted to heat which is predominantly dissipated from the core by virtue of radiative emission. Because the SANTE film is designed with arrays of plasmonic emitters, radiative emission is limited to a narrow-band that can be efficiently coupled to an external collector PV cell (shown on the interior wall of the shield). Collected energy can then be transferred through the shield to a power storage unit.

As we've seen in Chapter 6 and 7, gold-based exhibit nearly 100 % wide-angle spectrally selective absorption in the mid-IR despite very low ohmic losses of gold. We

103

also demonstrated in Chapter 6 that high absorbance can be explained in terms of critical coupling, in which case resistive losses are matched to radiative losses. With this simple design, the presence of the ground plane induced magnetic resonances, which dramatically reduce the radiative losses of the plasmonic eigenmodes. By choosing proper dimensions, the radiative and resistive losses were made equal, resulting in zero reflection.

From this perspective, various metals that display higher ohmic losses relative to gold can be adopted to create a narrow absorption/emission peak in the mid-IR range. On the other hand, high optical losses in tungsten naturally create broad-band absorption in the visible range for patterned tungsten surfaces [123]. Both the narrow-band infrared and broad-band visible absorption features are clearly identified in Fig. 8.1 (c), where it is shown that the frequency of the mid-IR absorption peak can be tuned by adjusting the patterning feature dimensions of the plasmonic structures while maintaining broad-band absorbance in the visible. An important feature of the SANTE structure is that it is extremely thin: less that $200\,nm$ assuming that the ground plane's thickness is on the order of the thickness of the patterned features, D. Therefore, it can be conformally wrapped around any heat exchange structure, such as hollow tubes (solar light receivers) that have a heat exchange fluid circulating through them. In this regard, power generation could be extended beyond the daylight period and maintain operation on cloudy days.
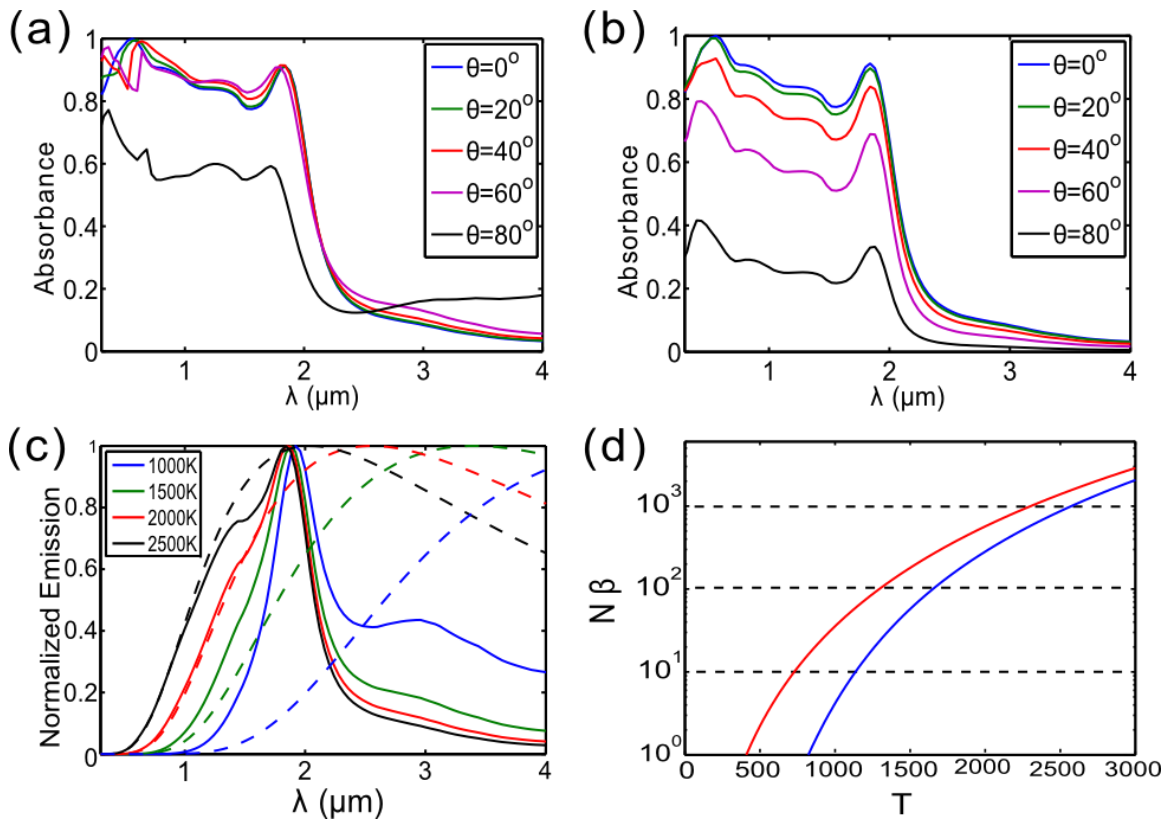
Figure 8.2: Numerical demonstration of wide-angle absorbance spectra of the SANTE film for (a) p polarized and (b) s polarized incident radiation for various incidence angles. (c) Normalized thermal emission spectra (per unit frequency) for black-body (dashed lines) and SANTE (solid lines) surfaces. Different colors correspond to different emitter temperatures. (d) Solar concentration versus equilibrium temperature for the SANTE surface (blue curve) and a black-body (red curve). Dimensions of the SANTE structure are given in nanometers for [L, W, D, G]=[330, 176, 80, 35] nm.

The specific choice for the narrow-band absorption peak at $\lambda_{IR} \approx 2.5\ \mu m$ for the designs illustrated in Fig. 8.1 is ideally suited to a PV cell that employs a narrow-gap semiconductor with $E_g < 0.5\ eV$. The SANTE film would operate at a modest temperature, $T_e < 2000\ K$, that corresponds to the black-body emission peak at $\lambda \approx 2.5\ \mu m$. The advantage of long λ_{IR} emission is that it is sufficiently far from the

105

visible absorption band, and therefore better spectral selectivity is achieved. The disadvantage is a lower operational temperature and, therefore, a smaller number of thermally emitted photons. As will be shown in Section 8.3, higher operation temperatures result in higher open circuit voltage and more efficient solar cells by virtue of lower Boltzman population of the semiconductor. The absorption spectra for a film design that operates at higher temperature and has an emissivity peak at $\lambda_{IR} \approx 1.9 \, \mu m$ are shown in Figs. 8.2 (a,b) for p and s polarizations, respectively. In this structure, the spectral selectivity of the IR absorption was considerably obscured by high absorption in the visible range. However, the effect of the visible absorption overlap did not prevent this particular SANTE from emitting spectrally-narrow thermal radiation.

The normalized thermal emissivity, $E(\lambda, T_e)$ (per unit frequency), of the SANTE film surface is shown in Fig. 8.2 (c) for several values of T_e. The emission spectrum centered at $\lambda_{IR} \approx 1.9 \, \mu m$ is spectrally narrow on both sides of λ_{IR}. The rapid decrease of emissivity for $\lambda > \lambda_{IR}$ is caused by the spectral selectivity of $A(\lambda, \theta, \phi) \equiv A(\lambda, \Omega)$ (where Ω is the solid angle). On the other hand, the rapid decrease of emissivity for $\lambda < \lambda_{IR}$ is caused by the dependence of $E_{BB}(\lambda, T_e)$. The frequency-selective emission of the surface, on one hand, helps to preserve the heat of the reservoir by reducing sub-bandgap emission, on the other, maintains a narrow emission spectrum that is used to generate electricity even when the temperature drops. By combining the structure with a heat reservoir (such as a heat exchange fluid), the STPV will have additional advantages over PVs. In this regard, the STPV cells can still generate electricity from the heat reservoir even in partial sun or darkness.

Another important function of the SANTE film is to provide heat insulation for the STPV system and core heat exchange element to reduce the rate of radiative losses. Better heat insulation permits lower solar radiation concentration to reach the design

temperature. Typically, the emitter needs to be maintained at highly elevated temperature ($T_e > 1000\ K$) to attain a high conversion efficiency. This is achieved by concentrating incident solar energy into the absorber, for example, by using non-imaging lenses or mirrors. For our calculations, we assumed moderate sun concentrations, $N \sim 1000$, so that the angular variation of the surface absorbance can be neglected, and the absorbed energy is directly proportional to N. Neglecting convective losses, the temperature T_e of the SANTE film is determined from the balance between heating by the absorbed solar energy and cooling by thermal infrared emission. In general, the area of solar absorption, A_{ab}, may be only a fraction of the total emitting surface area, A_e, as illustrated in Fig. 8.1 (a). We denote the ratio as $\beta = A_{ab}/A_e < 1$. The equilibrium temperature, T_e, is then found from the following equation:

$$\beta \int dE \int_{N\Omega_s} d\Omega \cos(\theta)\, \epsilon(\Omega, E) I_B(E, T_s)$$
$$= \int dE \int d\Omega \cos(\theta)\, \epsilon(\Omega, E)\, I_B(E, T_e), \tag{8.1}$$

where $d\Omega = d\phi\, dcos(\theta)$, $\Omega_s = 68.5\ \mu\text{Sr}$ is the solid angle subtended by the sun, N is the number of concentrated suns, and the sun's temperature $T_s \approx 6000\ K$ is assumed. The blue curve in Fig. 8.2 (d) can be used to determine the product of the sun's concentration and the fractional area of the absorber, $N\beta$, which is needed to achieve the equilibrium temperature T_e of the SANTE film. For comparison, the same dependence (red curve) is calculated for a black-body absorber/emitter. As these two curves in Fig. 8.2 (d) indicate, lower sun concentration is needed for the SANTE film due to better thermal insulation.

8.3 EFFICIENCY OF THE STPV SYSTEM

The conversion rate of solar energy to electric power using solar cells is limited by the detailed balance in the conversion process. In STPV systems, the efficiency of the solar energy absorber plays a large role in the total power conversion efficiency. The highest achievable overall system efficiency, η, can be conveniently represented as a product of the absorber efficiency, η_{ab} (which represents the fraction of the incident solar flux converted into heat by the SANTE), and the solar cell efficiency, η_{SC} (the highest achievable fraction of the IR flux incident from the SANTE onto the PV cell): $\eta = \eta_{ab}\,\eta_{SC}$ [121]. Although these two quantities can be independently evaluated, they are intimately tied together to each other because both absorption and emission occur on the same side of the SANTE film device, which is backed by a larger heat exchange reservoir.

The absorber efficiency is defined as the ratio between the absorbed and incident solar flux:

$$\eta_{ab} = \frac{\int dE \int_{N\Omega_s} d\Omega \cos(\theta)\,\epsilon(E,\Omega) I_B(E,T_s)}{\int dE \int_{N\Omega_s} d\Omega \cos(\theta)\,I_B(E,T_s)}, \qquad (8.2)$$

where $E = \hbar \times 2\pi c/\lambda$ is the photon's energy and $\epsilon(E,\Omega) \equiv E(\lambda,\Omega)$. Finite reflectance of the solar light results in $\eta_{ab} < 1$. Based on the same SANTE design given in Fig. 8.2, and assuming the black-body solar spectrum, we obtain from Eq. (8.2) that $\eta_{ab} = 89\,\%$ for normally incident sunlight.

Next, we calculated the collector PV cell efficiency η_{SC}. Assuming that the emitter temperature is maintained at T_e and the solar cell has an energy gap of E_g, the upper limit of the conversion efficiency from thermal radiation to electric power is given by $\eta_{sc} = U \times v \times m$ [119], where U is the so-called "ultimate efficiency" (proportional to the number of photo-excited electron-hole pairs times E_g, divided by the

incident thermal radiation flux), ν is the ratio of the open circuit voltage to $V_g = E_g/e$, and m is the so-called impedance mismatch that arises from the difference between open circuit and optimal voltage of the solar cell. Note that U, ν, and m are functions of T_e and E_g as well as functionals of $\epsilon(E,\Omega)$.

The ultimate efficiency, U, is calculated by assuming that every photon with energy greater than E_g excites one electron-hole pair. Taking into account the angular dependence of $\epsilon(E,\Omega)$ and averaging over both polarizations $(\epsilon(E,\Omega) = \epsilon_s(E,\Omega)/2 + \epsilon_p(E,\Omega)/2)$, U is then given by [119, 121]:

$$U = \frac{\int_0^{\pi/2} d\theta \, \sin(2\theta) \int_{E_G}^{\infty} dE \, \epsilon(E,\theta)I_B(E,T_e)E_g/E}{\int_0^{\pi/2} d\theta \, \sin(2\theta) \int_0^{\infty} dE \, \epsilon(E,\theta)I_B(E,T_e)}. \qquad (8.3)$$

However, the EMF induced by the electron-hole pair is only a fraction of E_g because of recombination processes in solar cells. The ratio between the open circuit voltage, V_{op}, and $V_g = E_g/q$ of a solar cell is denoted by ν. ν reaches a value of one when the solar cell temperature, T_c, is $0\,K$, and drops to zero when $T_c = T_e$. ν is given by:

$$\nu = \frac{V_{op}}{V_g} = \frac{k_b T_c}{E_g} \ln\left[f \frac{Q_e(T_e,E_g)}{Q_c(T_c,E_g)}\right]. \qquad (8.4)$$

Here, f describes non-ideal factors of the solar cell such as non-radiative recombination and non-unity absorption of the incident photons. We take $f = 1/2$ for the ideal case. The ratio Q_e/Q_c is expressed as:

$$\frac{Q_e}{Q_c} = \frac{\int_0^{\pi/2} d\theta \, \sin(2\theta) \int_{E_g}^{\infty} dE \, \epsilon(E,\theta)E^2/(\exp\left(\frac{E}{k_b T_e}\right) - 1)}{\int_{E_g}^{\infty} dE \, E^2/(\exp\left(\frac{E}{k_b T_c}\right) - 1)}. \qquad (8.5)$$

For a thermal emitter, the total number of photons emitted by the unit area of the emitter increases with the solid angle into which the IR photons are emitted. Therefore, wide-angle emissivity ensures that each point of the PV cell efficiently couples IR

109

photons from a large area of the emitter, resulting in higher voltages and enhanced conversion efficiency. It follows from Eqs. (8.4) and (8.5) that, for a given temperature, T_e, of the intermediate absorber/emitter, wide-angle emissivity results in higher V_{op}. For example, with $T_c = 300\,K$ and $E_g = 0.5\,eV$, an order of magnitude increase in the solid angle span results in a $12\,\%$ increase in v.
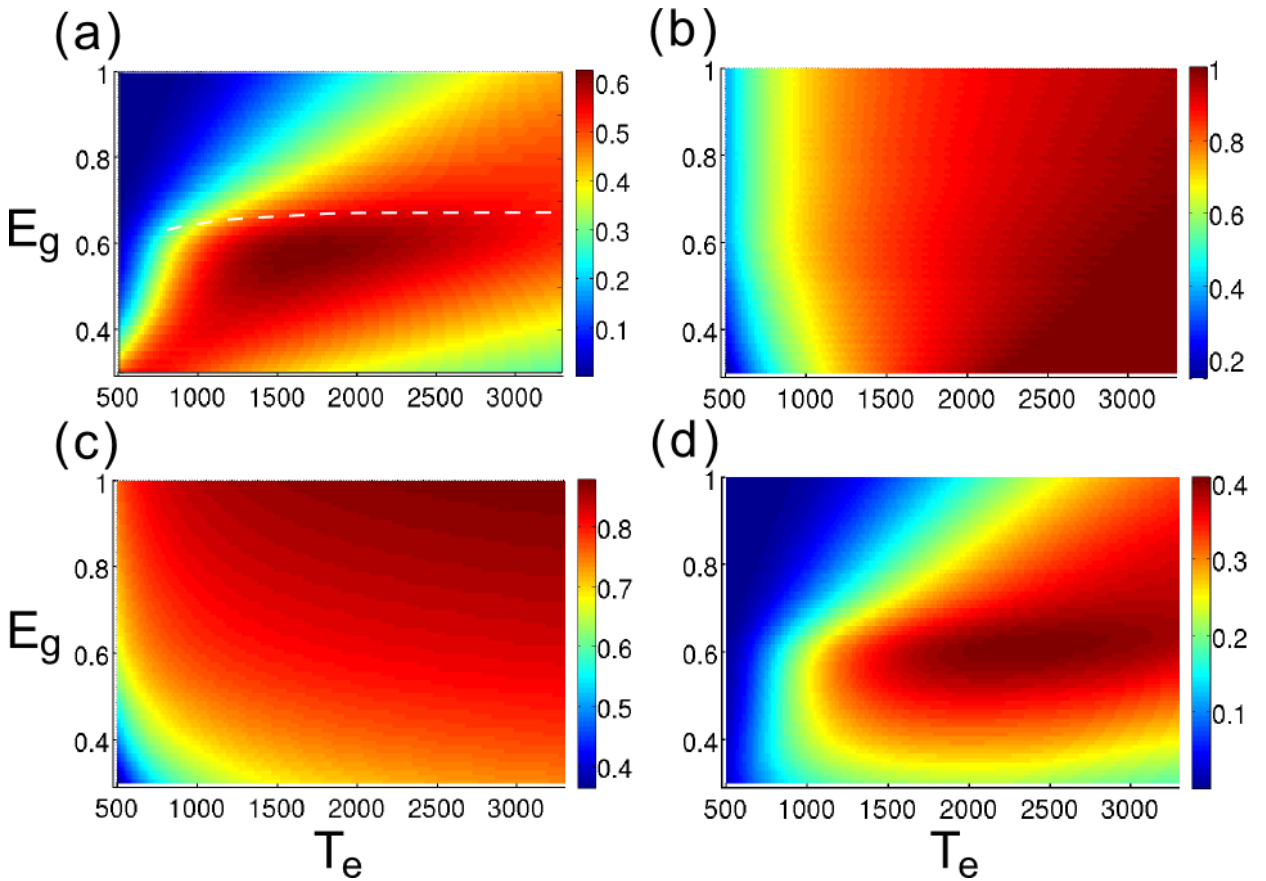
Figure 8.3: Efficiency limitation of the STPV system as a function of both solar cell energy gap, E_g, and emitter temperature, T_e. (a) Ultimate efficiency, U, (b) $v = V_{op}/V_g$, (c) impedance matching factor, m, and (d) the total efficiency $\eta = \eta_{ab}(89\,\%) \times U \times v \times m$. Dashed line in (a) represents the photon energy at the peak of IR emission ($\lambda_{IR} = 1.9\,\mu m$, or $E_{IR} = 0.67\,eV$) from the SANTE surface.

The impedance factor, denoted by m, maximizes the electric power that can be extracted from a single-junction solar cell with an open circuit voltage V_{op}, and is given by:

$$m = \frac{z_m^2}{(1 + z_m - \exp(-z_m))(z_m + \ln(1 + z_m))}, \qquad (8.6)$$

with z_m being determined by $z_m + ln(1 + z_m) = qV_{op}/k_bT_c$.

Individual efficiency factors U, v, and m) as well as the total efficiency, η, are plotted in Fig. 8.3 as functions of the band gap, E_g, of a single-junction collector PV cell and the temperature, T_e, of the SANTE structure. Fig. 8.3 (a) illustrates that the ultimate efficiency, U, of the collector PV cell is optimized when the energy of an IR photon emitted at the peak of the IR emissivity is slightly higher than E_g to minimize the number of "wasted" thermal photons whose energy fall below the band gap energy. Ultimate efficiency peaks at the modest temperature, $T_e \approx 1700\,K$, and falls off for higher temperatures because of the thermal broadening of the emissivity spectrum. The decrease of U for lower temperatures is due to the strong mismatch between the peaks of $E_{BB}(\lambda, T_e)$ and $A(\lambda, \Omega)$ as illustrated for $T_e = 1000\,K$ in Fig. 8.2 (c). Nevertheless, the highest total conversion efficiency, $\eta = 41\,\%$, is achieved at a considerably higher absorber/emitter temperature of $T_e \approx 2300\,K$ because of the monotonic increase of the remaining two efficiency factors with temperature.
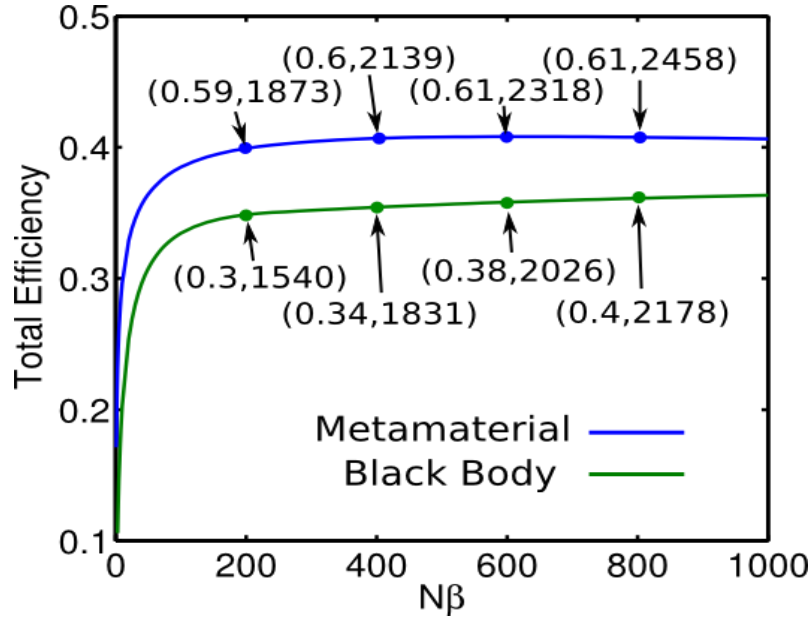
Figure 8.4: Total efficiency of the STPV system, η, versus solar concentration, $N\beta$. The blue curve corresponds to using the metamaterial as the intermediate structure and the green curve corresponds to using a black body. Numbers in the parentheses, (E_g, T_e), show the optimized band gap of the PV cell and the equilibrium temperature of the intermediate layer under the corresponding solar concentration.

It is clear from Fig. 8.3 (a) that the major advantage of the STPV system resides in the enhancement of the ultimate efficiency, U. Because the engineered emission spectrum of the SANTE structure reduces the number of sub-bandgap photons, U reaches 62 % compared to 44 % for the case of traditional visible PV cells. On the other hand, because T_e is much smaller than the temperature of the sun, and also a smaller E_g is typically used, both v and m are slightly smaller than in the case of PV cells. Nevertheless, the overall STPV efficiency (at $E_g = 0.6\ eV$) considerably exceeds the corresponding SQ limit of $\eta_{SQ} = 31$ %. Note that, depending on the specific design of the SANTE surface, the optimal T_e and E_g corresponding to the highest overall

efficiency will shift. Therefore, it may be possible to design an appropriate SANTE for any values of (T_e, E_g) dictated by specific technological constraints.

In Fig. 8.4, we compared the case of using the metamaterial structure as the intermediate layer to that of using a black body. First of all, it is shown that the total efficiency of using the metamaterial (41%) is indeed higher than that of using a black body (~35%). Moreover, because of the property of thermal insulation provided by the metamaterial emissivity, the equilibrium temperature of the metamaterial emitter is typically 300 degrees higher than that of the black body. It is also noticed that, because of the engineered emissivity targeting 0.6 eV, the optimized band gap of the PV cells, E_g, stays a constant in the case with the metamaterial emitter, while optimized E_g varies from 0.3 to 0.4 eV when changing the solar concentration.

8.4   CONCLUSIONS

STPV systems are attractive for achieving higher solar power conversion efficiencies versus PV devices with single junctions. However, the efficiencies of STPV systems highly depend on the specific absorbing and emitting properties of the intermediate structures. Integrated structures that can absorb a large fraction of the solar spectrum, yet only emit in a narrow-band frequency into secondary bandgap-matched PV cells are desired. We demonstrated that a combination of high material ohmic loss in the visible with structural resonances in the mid-IR led to a SANTE film design that was capable of achieving both broad-band absorption to collect solar energy and narrow-band emission to drive the solar cells. The theoretical limit of an STPV system with such SANTE structures was calculated to be 41 %, which is higher than the SQ limit of

31 %. The efficiency remains above 31 % for $T_e > 1200\ K$, when a heat reservoir that extends the power-generating period is included in the STPV system design.

Chapter 9

Conclusions and Outlook

9.1 SUMMARY

In the previous Chapters, we have seen the plasmonic Fano resonant structures being applied to a variety of areas, ranging from signal processing, biomolecule detection, sub-diffraction imaging, to absorbers designed for energy harvesting and thermal emission. The strength of the plasmonics or the metamaterials resides in the capability of engineering and shaping the optical properties of the material to our desired bandwidth and functionality. For example, we intentionally designed the Fano resonant structure in Chapter 4, so that the resonances overlap with the biomolecule fingerprints. In this way, we were able to demonstrate ultra-sensitive characterization of the molecules. Also in Chapter 8, we showed that a metamaterial surface can be designed to both absorb the sunlight and emit to the specific frequency suitable for the PV cells. Such spectral selective design results in enhanced energy conversion efficiency.

Despite being able to show intriguing optical responses, the nanostructure designs should be kept as simple as possible to widen their applicability. During the discussion, we have seen that interesting properties doesn't necessarily rely on complicated structural designs. The nan-protractor presented in Chapter 5 involves as simple as two nanoparticles to demonstrate the Fano resonance and the concept of PST. Although AFM manipulation was used in the study, self-assembling techniques can in principle be applied to assemble these clusters. Therefore, utilizing the PST to imaging and tracking the motions of molecules can be envisioned. The absorber design introduced in Chapter 6 is another example of simple plasmonic designs. It consists of strip or patch arrays backed by a ground plate reflector. These absorbers have only one layer of shaped

115

structures, and therefore can be fabricated using the nano-imprint lithography, which has much higher throughput compared to the lift-off process.

Even though our discussion is very limited to the group of Fano resonant plasmonic structures rather than the whole spectrum of the plasmonics, these examples should still suffice to demonstrate the potential usefulness of the plasmonic nanostructures. Because of its wide applicability, the study of plasmonics has become an interdisciplinary research area that combines physics, nano-engineering, material science, chemical engineering, life science and so on. During my PhD study leading to this dissertation, I have not only learned about the physics of plasmonics and nanostructures, but also dabbled in computer science when learning advanced numerical techniques and molecular biology when investigating the interaction between the biomolecules and the plasmonic structures. It is a field that learning new things and combining knowledge from different areas can generate new ideas and possibilities.

9.2   DIRECTIONS FOR FUTURE RESEARCH

There are certainly many aspects of the plasmonics or the Fano interference that I haven't touched in this dissertation, and therefore future research is warranted. In the following, I'll complete my dissertation by pointing out some potentially interesting topics extending from our works presented in this dissertation.

In regard to the DCF presented in Chapter 3, we used a multilayer structure to demonstrate the broadband slow light and the uniform GVD. The drawback of such structure is mainly the difficulty in fabrication. Additionally, the Ohmic loss of about 60 % may be useful for constructing a broadband or spectral selective absorber, but is certainly not appealing for signal processing purposes. These issues can in principle be

resolved by considering other platforms for realizing the DCF. For example, a photonic waveguide can be adopted to replace the layer-by-layer plasmonic structure to reduce the footprint. Also the Ohmic loss is dramatically reduced when using photonic crystals.

Dielectric metamaterials that use high index semiconductors, such as Si and Ge, to replace metals seem to be an alternative approach to avoid the Ohmic loss in plasmonic structures. The idea behind using dielectrics is to take advantage of the Mie resonances of the structure in order to induce either the electric or magnetic responses. There are limitations to the dielectric metamaterials as well. For example, the volume of the dielectric has to be large enough to support the Mie resonances, and therefore the structure sizes of the metamaterials cannot reach deep subwavelength scale. Also the high index semiconductors are generally very lossy in the near IR and visible range because the photon energy is close to the semiconductor bandgaps.

Nevertheless, the dielectric metamaterials still seem to have certain advantages over metals in the mid-IR frequency range. In Chapter 2, we showed that the quality factor of the Fano interference is ultimately limited by the Ohmic loss in metal. By switching to dielectric materials, the Ohmic loss can be dramatically reduced, and therefore a much higher quality factor, Q, can be reached while still keeping a small mode volume, V_{mode}, of a metamaterial. The Purcell factor, $F = \frac{3}{4\pi^2} \left(\frac{\lambda}{n}\right)^3 \frac{Q}{V_{mode}}$, involves both Q and V_{mode}. It defines the strength of light-matter interactions, such as the nonlinear effect of a material and the spontaneous emission rate of a gain medium. In photonic devices, such a whisper galley modes, extremely high Q of 8×10^9 is achievable, but at the cost of a large mode volume (about $6000\ \lambda^3$) [125]. On the other hand, in plasmonic resonators, such as bowtie antennae, the mode volume can be as small as $10^{-4}\ \lambda^3$ with a Q value less than10 [126]. It would be interesting to see if there is

117

advantage in utilizing dielectric metamaterials in the mid-IR range to attain both high Q and small V_{mode}, and therefore much larger Purcell factors.

During our research in the FRAMM, we found that the dark resonance of the FRAMM actually relies on collective response to certain extent. The quadrupolar resonance of a single FRAMM cell is not a dark resonance by itself, because a quadruple still radiates along a 2-dimensional plan. When using a periodic FRAMM array, the quadrupolar radiations from different cells cancel out because the radiating wavelength is incommensurate to the lattice constant. As a result, the radiative loss can be essentially zero. Our preliminary study indicates that about ten cells would be enough to induce efficient cancellation of the quadrupolar radiation, and therefore reach a high quality collective resonance. It would be interesting to investigate how the presence of other resonators affects the collective response, or how different unit cells interact with each other. On the other hand, imperfect arrangement of the array and variations from cell to cell are always practical issues when fabricating the samples. Therefore, how randomness or artificially introduced variations in the array affect the collective behavior and energy distribution in the medium is also an important issue, and would promote our understanding on how to manipulate electromagnetic fields.

Bibliography

1. H. Haus, *Waves and Fields in Optoelectronics* (Prentice-Hall:Englewood Cliffs, NJ, 1984).

2. R. E. Hamam, A. Karalis, J. D. Joannopoulos, and M. Soljačić, Coupled-mode theory for general free-space resonant scattering of waves. *Physical Review A* **75**, 053801 (2007).

3. Z. Ruan and S. Fan, Superscattering of Light from Subwavelength Nanostructures. *Physical Review Letters* **105**, 013901 (2010).

4. Z. Ruan and S. Fan, Temporal coupled-mode theory for light scattering by an arbitrarily shaped object supporting a single resonance. *Physical Review A* **85**, 043828 (2012).

5. E. Waks and J. Vuckovic, Coupled mode theory for photonic crystal cavity-waveguide interaction. *Optics Express* **13** (13), 5064-5073 (2005).

6. N. Liu, L. Langguth, T. Weiss, J. Kästel, M. Fleischhauer, T. Pfau, and H. Giessen, Plasmonic analogue of electromagnetically induced transparency at the Drude damping limit. *Nature Materials* **8**, 758-762 (2009).

7. S. Zhang, D. A. Genov, Y. Wang, M. Liu, and X. Zhang, Plasmon-Induced Transparency in Metamaterials. *Physical Review Letters* **101**, 047401 (2008).

8. A. Majumdar, A. Faraon, E. Kim, D. Englund, H. Kim, P. Petroff, and J. Vuckovic, Linewidth broadening of a quantum dot coupled to an off-resonant cavity. *Physical Review B* **82**, 045306 (2010).

9. S. J. Orfanidis, Electromagnetic Waves and Antennas, Available at http://eceweb1.rutgers.edu/~orfanidi/ewa/ (2010).

10. L. V. Hau, S. E. Harris, Z. Dutton, and C. H. Behroozi, Light speed reduction to 17 metres per second in an ultracold atomic gas. *Nature* **397**, 594-598 (1999).

11. T. F. Krauss, Why do we need slow light? *Nature Photonics* **2**, 448 - 450 (2008).

12. Z. Zhu, D. J. Gauthier, and R. W. Boyd, Stored Light in an Optical Fiber via Stimulated Brillouin Scattering. *Science* **318**, 1748-1750 (2007).

13. S. E. Harris, Electromagnetically Induced Transparency. *Physics Today* **50** (7), 36 (1997).

14. D. Budker, D. F. Kimball, S. M. Rochester, and V. V. Yashchuk, Nonlinear Magneto-optics and Reduced Group Velocity of Light in Atomic Vapor with Slow Ground State Relaxation. *Phys. Rev. Lett.* **83** (9), 1767–1770 (1999).

15. G. Shvets and J. S. Wurtele, Transparency of Magnetized Plasma at the Cyclotron Frequency. *Phys. Rev. Lett.* **89** (11), 115003 (2002).

16. Y. Avitzour and G. Shvets, Manipulating Electromagnetic Waves in Magnetized

Plasmas: Compression, Frequency Shifting, and Release. *Phys. Rev. Lett.* **100** (6), 065006 (2008).

17. N. Papasimakis, V. A. Fedotov, N. I. Zheludev, and S. L. Prosvirnin, Metamaterial Analog of Electromagnetically Induced Transparency. *Phys. Rev. Lett.* **101** (25), 253903 (2008).

18. U. Fano, Effects of Configuration Interaction on Intensities and Phase Shifts. *Phys. Rev.* **124** (6), 1866–1878 (1961).

19. A. E. Miroshnichenko, S. Flach, and Y. S. Kivshar, Fano resonances in nanoscale structures. *Reviews of Modern Physics* **82**, 2257–2298 (2010).

20. B. Luk'yanchuk, N. I. Zheludev, S. A. Maier, N. J. Halas, P. Nordlander, H. Giessen, and C. T. Chong, The Fano resonance in plasmonic nanostructures and metamaterials. *Nature Materials* **9**, 707–715 (2010).

21. K. L. Tsakmakidis, A. D. Boardman, and O. Hess, 'Trapped rainbow' storage of light in metamaterials. *Nature* **450**, 397-401 (2007).

22. Q. Gan, Z. Fu, Y. J. Ding, and F. J. Bartoli, Ultrawide-Bandwidth Slow-Light System Based on THz Plasmonic Graded Metallic Grating Structures. *Phys. Rev. Lett.* **100** (25), 256803 (2008).

23. M. A. Ordal, Robert J. Bell, R. W. Alexander,Jr, L. L. Long, and M. R. Querry, Optical properties of fourteen metals in the infrared and far infrared: Al, Co, Cu, Au, Fe, Pb, Mo, Ni, Pd, Pt, Ag, Ti, V, and W. *Applied Optics* **24** (24), 4493–4499 (1985).

24. K. Henzler-Wildman and D. Kern, Dynamic personalities of proteins. *Nature* **450**, 964-972 (2007).

25. R. Jimenez, G. Salazar, J. Yin, T. Joo, and F. E. Romesberg, Protein dynamics and the immunological evolution of molecular recognition. *Proc. Natl Acad. Sci. USA* **101**, 3803-3808 (2004).

26. D. D. Boehr and P. E. Wright, How Do Proteins Interact? *Science* **320**, 1429-1430 (2008).

27. L. C. James, P. Roversi, and D. S. Tawfik, Antibody Multispecificity Mediated by Conformational Diversity. *Science* **299**, 1362-1367 (2003).

28. E. Gizeli and C. R. Lowe, *Biomolecular sensors* (Taylor & Francis, New York, 2002).

29. N. Ramachandran, D. N. Larson, P. R. H. Stark, E. Hainsworth, J. LaBaer, Emerging tools for real-time label-free detection of interactions on functional protein microarrays. *FEBS Journal* **272**, 5412-5425 (2005).

30. K. Phillips, J. Homola, Surface plasmon resonance-based sensors. *Analytical and Bioanalytical Chemistry* **390**, 1221-1222 (2008).

31. D. M. Gakamsky, I. F. Luescher, and I. Pecht, T cell receptor-ligand interactions: A conformational preequilibrium or an induced fit. *Proc. Natl Acad. Sci. USA* **101**,

9063-9066 (2004).

32. F. Le, D. W. Brandl, Y. A. Urzhumov, H. Wang, J. Kundu, N. J. Halas, J. Aizpurua , and P. Nordlander, Metallic Nanoparticle Arrays: A Common Substrate for Both Surface-Enhanced Raman Scattering and Surface-Enhanced Infrared Absorption. *ACS Nano* **2**, 707–718 (2008).

33. S. Nie and S. R. Emory, Probing Single Molecules and Single Nanoparticles by Surface-Enhanced Raman Scattering. *Science* **275**, 1102 (1997).

34. R. Adato, A. A. Yanika, J. J. Amsden, D. L. Kaplan, F. G. Omenetto, M. K. Hong, S. Erramilli, and H. Altug , Ultra-sensitive vibrational spectroscopy of protein monolayers with plasmonic nanoantenna arrays. *Proc. Natl Acad. Sci. USA* **106**, 19227–19232 (2009).

35. D. Enders, S. Rupp, A. Kuller, and A. Pucci, Surface Enhanced Infrared Absorption on Au Nanoparticle Films Deposited on SiO2/Si for Optical Biosensing: Detection of the Antibody-Antigen Reaction. *Surf. Sci.* **600**, L305–L308 (2006).

36. E. Cubukcu, S. Zhang, Y.-S. Park, G. Bartal, X. Zhang, Split ring resonator sensors for infrared detection of single molecular monolayers. *Appl. Phys. Lett.* **95**, 043113 (2009).

37. A. Dong, P. Huang, and W. S. Caughey, Protein Secondary Structures in Water from Second-Derivative Amide I Infrared Spectra. *Biochemistry* **29**, 3303-3308 (1990).

38. L. P. DeFlores, Z. Ganim, R. A. Nikodemus, A. Tokmakoff, Amide I-II 2D IR Spectroscopy Provides Enhanced Protein Structural Sensitivity. *J. Am. Chem. Soc.* **131**, 3385-3391 (2009).

39. E. Kauffmann, N. C. Darnton, R. H. Austin, C. Batt, and K. Gerwert, Lifetimes of intermediates in the β-sheet to α-helix transition of β-lactoglobulin by using diffusional IR mixer. *Proc. Natl Acad. Sci. USA* **98**, 6646–6649 (2001).

40. D. R. Smith, J. B. Pendry, and M. C. K Wiltshire, Metamaterials and Negative Refractive Index. *Science* **305**, 788–792 ((2004)).

41. G. Dolling, C. Enrich, M. Wegener, C. M. Soukoulis, and S. Linden, Observation of simultaneous negative phase and group velocity of light. *Science* **312**, 892–894 (2006).

42. V. A. Fedotov, N. Papasimakis, E. Plum, A. Bitzer, M. Walther, P. Kuo, D. P. Tsai, and N. I. Zheludev, Spectral collapse in ensembles of meta-molecules. *Phys. Rev. Lett.* **104**, 223901 (2010).

43. T. J. Yen, W. J. Padilla, N. Fang, D. C. Vier, D. R. Smith, J. B. Pendry, D. N. Basov, X. Zhang, Terahertz Magnetic Response from Artificial Materials. *Science* **303**, 1494–1496 (2004).

44. A. J. Hoffman, L. Alekseyev, S. S. Howard, K. J. Franz, D. Wasserman, V. A. Podolskiy, E. E. Narimanov, D. L. Sivco, and C. Gmachl, Negative refraction in semiconductor

metamaterials. *Nature Mater.* **6**, 946–950 (2007).

45. N. Liu, M. Mesch, T. Weiss, M. Hentschel, and H. Giessen., Infrared perfect absorber and its application as plasmonic sensor. *Nano Lett.* **10**, 2342–2348 (2010).

46. N. Liu, M. L. Tang, M. Hentschel, H. Giessen, and A. P. Alivisatos, Nanoantenna-enhanced gas sensing in a single tailored nanofocus. *Nature Materials* **10**, 631-636 (2011).

47. A. V. Kabashin, P. Evans, S. Pastkovsky, W. Hendren, G. A. Wurtz, R. Atkinson, R. Pollard, V. A. Podolskiy, and A. V. Zayats, Plasmonic nanorod metamaterials for biosensing. *Nature Mater.* **8**, 867–871 (2009).

48. J. B. Lassiter, H. Sobhani, J. A. Fan, J. Kundu, F. Capasso, P. Nordlander and N. J. Halas, Fano Resonances in Plasmonic Nanoclusters: Geometrical and Chemical Tunability. *Nano Lett.* **10**, 3184–3189 (2010).

49. C. Yu, A. Ganjoo, H. Jain, C. G. Pantano, and J. Irudayaraj, Mid-IR Biosensor: Detection and Fingerprinting of Pathogens on Gold Island Functionalized Chalcogenide Films. *Anal. Chem.* **78**, 2500–2506 (2006).

50. F. J. García de Abajo, Light scattering by particle and hole arrays. *Rev. Mod. Phys.* **79**, 1267–1290 (2007).

51. N. Papasimakis, V. A. Fedotov, Y. H. Fu, D. P. Tsai, and N. I. Zheludev, Coherent and incoherent metamaterials and order-disorder transitions. *Phys. Rev. B* **80** (4), 041102(R) (2009).

52. V. A. Fedotov, M. Rose, S. L. Prosvirnin, N. Papasimakis, and N. I. Zheludev, Sharp Trapped-Mode Resonances in Planar Metamaterials with a Broken Structural Symmetry. *Phys. Rev. Lett.* **99**, 147401 (2007).

53. C. Wu, A. B. Khanikaev, and G. Shvets, Broadband Slow Light Metamaterial Based on a Double-Continuum Fano Resonance. *Phys. Rev. Lett.* **106**, 107403 (2011).

54. N. Verellen, Y. Sonnefraud, H. Sobhani, F. Hao, V. V. Moshchalkov, P. V. Dorpe, P. Nordlander and S. A. Maier, Fano resonances in individual coherent plasmonic nanocavities. *Nano Lett.* **9**, 1663–1667 (2009).

55. J. A. Fan, K. Bao, C. Wu, J. Bao, R. Bardhan, N. J. Halas, V. N. Manoharan, G. Shvets, P. Nordlander, and F. Capasso, Fano-like Interference in Self-Assembled Plasmonic Quadrumer Clusters. *Nano Lett.* **10**, 4680–4685 (2010).

56. J. A. Fan, C. Wu, K. Bao, J. Bao, R. Bardhan, N. J. Halas, V. N. Manoharan, P. Nordlander, G. Shvets, F. Capasso, Self-Assembled Plasmonic Nanoparticle Clusters. *Science* **328**, 1135–1138 (2010).

57. N. Verellen, P. V. Dorpe, C. Huang, K. Lodewijks, G. A. E. Vandenbosch, L. Lagae, and V. V. Moshchalkov, Plasmon Line Shaping Using Nanocrosses for High Sensitivity Localized Surface Plasmon Resonance Sensing. *Nano Letters* **11**, 391 (2011).

58. H. Chen, J. Huang, J. Lee, S. Hwang, and K. Koh, Surface plasmon resonance

spectroscopic characterization of antibody orientation and activity on the calixarene monolayer. *Sens. Actuators B* **147**, 548–553 (2010).

59. S. Kumar, J. Aaron, and K. Sokolov, Directional conjugation of antibodies to nanoparticles for synthesis of multiplexed optical contrast agents with both delivery and targeting moieties. *Nature Protoc.* **3**, 314-320 (2008).

60. E. N. Lewis, P. J. Treado, R. C. Reedor, G. M. Stay, A. E. Dowrey, C. Marcott, I. W. Levin, Fourier Transform Spectroscopic Imaging Using an Infrared Focal-Plane Array Detector. *Anal. Chem.* **67**, 3377-3381 (1995).

61. M. Hentschel, M. Saliba, R. Vogelgesang, H. Giessen, A. P. Alivisatos, and N. Liu, Transition from Isolated to Collective Modes in Plasmonic Oligomers. *Nano Lett.* **10**, 2721–2726 (2010).

62. J. D. Joannopoulos, S. G. Johnson, J. N. Winn, and R. D. Meade, *Photonic Crystals: Molding the Flow of Light*, 2nd ed. (Princeton University Press, Princeton, NJ, 2008).

63. X. Jiang, E. Zaitseva, M. Schmidt, F. Siebert, M. Engelhard, R. Schlesinger, K. Ataka, R. Vogel, and J. Heberle, Resolving voltage-dependent structural changes of a membrane photoreceptor by surface-enhanced IR difference spectroscopy. *Proc. Natl Acad. Sci. USA* **105**, 12113-12117 (2008).

64. D. Englund, A. Faraon, I. Fushman, N. Stoltz, P. Petroff, and J. Vuckovic, Controlling cavity reflectivity with a single quantum dot. *Nature* **450**, 857–861 (2007).

65. Y. M. Bae, B.-K. Oh, W. Lee, W. H. Lee, J.-W Choi, Study on orientation of immunoglobulin G on protein G layer. *Biosensors & Bioelectronics* **21**, 103–110 (2005).

66. K. Li, M. I. Stockman, and D. J. Bergman, Self-Similar Chain of Metal Nanospheres as an Efficient Nanolens. *Physical Review Letters* **91**, 227402 (2003).

67. A. Bouhelier, M. Beversluis, A. Hartschuh, and L. Novotny, Near-Field Second-Harmonic Generation Induced by Local Field Enhancement. *Physical Review Letters* **90**, 013903 (2003).

68. S. Kim, J. Jin, Y.-J. Kim, I.-Y. Park, Y. Kim and S.-W. Kim, High-harmonic generation by resonant plasmon field enhancement. *Nature* **453**, 757-760 (2008).

69. N. Fang, H. Lee, C. Sun, and X. Zhang, Sub–Diffraction-Limited Optical Imaging with a Silver Superlens. *Science* **308**, 534-537 (2005).

70. T. Taubner, D. Korobkin, Y. Urzhumov, G. Shvets, and R. Hillenbrand, Near-Field Microscopy Through a SiC Superlens. *Science* **313**, 1595 (2006).

71. A. Cvitkovic, N. Ocelic, J. Aizpurua, R. Guckenberger, and R. Hillenbrand, Infrared Imaging of Single Nanoparticles via Strong Field Enhancement in a Scanning Nanogap. *Physical Review Letters* **97**, 060801 (2006).

72. S. Kawata, Y. Inouye and P. Verma, plasmonics for near-field nano-imaging and superlensing. *Nature Photonics* **3**, 388-394 (2009).

73. K.-H. Su, Q.-H. Wei, X. Zhang, J. J. Mock, D. R. Smith, and S. Schultz, Interparticle Coupling Effects on Plasmon Resonances of Nanogold Particles. *Nano Letters* **3** (8), 1087–1090 (2003).

74. L. V. Brown, H. Sobhani, J. B. Lassiter, P. Nordlander, and N. J. Halas, Heterodimers: Plasmonic Properties of Mismatched Nanoparticle Pairs. *ACS Nano* **4** (2), 819-832 (2010).

75. C. Sönnichsen, B. M. Reinhard, J. Liphardt, and A. P. Alivisatos, A molecular ruler based on plasmon coupling of single gold and silver nanoparticles. *Nature Biotechnology* **23**, 741-745 (2005).

76. Y.-W. Jun, S. Sheikholeslami, D. R. Hostetter, C. Tajon, C. S. Craik, and A. P. Alivisatos, Continuous imaging of plasmon rulers in live cells reveals early-stage caspase-3 activation at the single-molecule level. *PNAS* **106**, 17735-17740 (2009).

77. N. Liu, M. Hentschel, T. Weiss, A. P. Alivisatos, and H. Giessen, Three-Dimensional Plasmon Rulers. *Science* **332**, 1407-1410 (2011).

78. L. Stryer and R. P. Haugland, Energy transfer: a spectroscopic ruler. *PNAS* **58** (2), 719–726 (1967).

79. R. Roy, S. Hohng, and T. Ha, A practical guide to single-molecule FRET. *Nature Methods* **5**, 507 - 516 (2008).

80. L. Novotny, EffectiveWavelength Scaling for Optical Antennas. *Physical Review Letters* **98**, 266802 (2007).

81. S. Mukherjee, H. Sobhani, J. B. Lassiter, R. Bardhan, P. Nordlander, and N. J. Halas, Fanoshells: Nanoparticles with Built-in Fano Resonances. *Nano Letters* **10** (7), 2694–2701 (2010).

82. C. Wu, A. B. Khanikaev, R. Adato, N. Arju, A. A. Yanik, H. Altug, and G. Shvets, Fano-resonant asymmetric metamaterials for ultrasensitive spectroscopy and identification of molecular monolayers. *Nature Materials* **11**, 69-75 (2012).

83. D. A. Powell, M. Lapine, M. V. Gorkunov, I. V. Shadrivov, and Y. S. Kivshar, Metamaterial tuning by manipulation of near-field interaction. *Physical Review B* **82**, 155128 (2010).

84. Y. A. Urzhumov and G. Shvets, Optical magnetism and negative refraction in plasmonic metamaterials. *Solid State Communications* **146**, 208-220 (2008).

85. J. B. Pendry, Negative Refraction Makes a Perfect Lens. *Phys. Rev. Lett.* **85** (18), 3966–3969 (2000).

86. D. Schurig, J. J. Mock, B. J. Justice, S. A. Cummer, J. B. Pendry, A. F. Starr, and D. R. Smith, Metamaterial Electromagnetic Cloak at Microwave Frequencies. *Science* **314**, 977-980 (2006).

87. A. Alu and N. Engheta, Guided modes in a waveguide filled with a pair of single-negative (SNG), double-negative (DNG), and/or double-positive (DPS) layers. *IEEE*

Trans. Microw. Th. Tech. **52** (1), 199 - 210 (2004).

88. H.-T. Chen and J. F. O'Hara and A. K. Azad and A. J. Taylor and R. D. Averitt and D. B. Shrekenhamer and W. J. Padilla, Experimental demonstration of frequency-agile terahertz metamaterials. *Nature Photonics* **2**, 295 - 298 (2008).

89. N. I. Landy, S. Sajuyigbe, J. J. Mock, D. R. Smith, and W. J. Padilla, Perfect Metamaterial Absorber. *Phys. Rev. Lett.* **100** (20), 207402 (2008).

90. T. J. Coutts, A review of progress in thermophotovoltaic generation of electricity. *Renewable and Sustainable Energy Reviews* **3**, 77-184 (1999).

91. M. Laroche, R. Carminati, and J.-J. Greffet, Near-field thermophotovoltaic energy conversion. *Journal of Applied Physics* **100** (6), 063704 (2006).

92. K. Tvingstedt, N.-K. Persson, O. Inganäs, A. Rahachou, and I. V. Zozoulenko, Surface plasmon increase absorption in polymer photovoltaic cells. *Applied Physics Letters* **91** (11), 113514 (2007).

93. H. Tao, C. M. Bingham, A. C. Strikwerda, D. Pilon, D. Shrekenhamer, N. I. Landy, K. Fan, X. Zhang, W. J. Padilla, and R. D. Averitt, Highly flexible wide angle of incidence terahertz metamaterial absorber: Design, fabrication, and characterization. *Phys. Rev. B* **78** (24), 241103(R) (2008).

94. C. Wu, Y. Avitzour, and G. Shvets, Ultra-thin wide-angle perfect absorber for infrared frequencies. *Proc. SPIE* **7029**, 70290W (2008).

95. M. Diem, T. Koschny, and C. M. Soukoulis, Wide-angle perfect absorber/thermal emitter in the terahertz regime. *Phys. Rev. B* **79** (3), 033101 (2009).

96. J. Hao, J. Wang, X. Liu, W. J. Padilla, L. Zhou, and M. Qiu, High performance optical absorber based on a plasmonic metamaterial. *Applied Physics Letters* **96** (25), 251104 (2010).

97. S. C. Johnson, T. C. Bailey, M. D. Dickey, B. J. Smith, E. K. Kim, A. T. Jamieson, N. A. Stacey, J. G. Ekerdt, C. G. Willson, D. P. Mancini, W. J. Dauksher, K. J. Nordquist, and D. J. Resnick, Advances in Step and Flash imprint lithography. *Proc. SPIE* **5037**, 197 (2003).

98. Y. Avitzour, Y. A. Urzhumov, and G. Shvets, Wide-angle infrared absorber based on a negative-index plasmonic metamaterial. *Phys. Rev. B* **79** (4), 045131 (2009).

99. X. Liu, T. Starr, A. F. Starr, and W. J. Padilla, Infrared Spatial and Frequency Selective Metamaterial with Near-Unity Absorbance. *Phys. Rev. Lett.* **104** (20), 207403 (2010).

100. N. I. Landy, C. M. Bingham, T. Tyler, N. Jokerst, D. R. Smith, and W. J. Padilla, Design, theory, and measurement of a polarization-insensitive absorber for terahertz imaging. *Phys. Rev. B* **79** (12), 125104 (2009).

101. D. R. Smith, S. Schultz, P. Markoš, and C. M. Soukoulis, Determination of effective permittivity and permeability of metamaterials from reflection and transmission

coefficients. *Phys. Rev. B* **65** (19), 195104 (2002).

102. B. Neuner III, D. Korobkin, C. Fietz, D. Carole, G. Ferro, and G. Shvets, Critically coupled surface phonon-polariton excitation in silicon carbide. *Optics Letters* **34** (17), 2667-2669 (2009).

103. S. Y. Chou, P. Krauss, and P. J. Renstrom, Nanoimprint lithography. *Journal of Vacuum Science & Technology B* **14** (6), 4129 (1996).

104. I. V. Lindell, S. A. Tretyakov, K. I. Nikoskinen, and S. Ilvonen, BW media-Media with negative parameters, capable of supporting backward waves. *Microw. Opt. Techn. Let.* **31**, 129-133 (2001).

105. D. R. Smith and D. Schurig, Electromagnetic wave propagation in media with indefinite permittivity and permeability tensors. *Phys. Rev. Lett.* **90** (7), 077405 (2003).

106. P. L. Stiles, J. A. Dieringer, N. C. Shah, and R. P. Van Duyne, Surface-enhanced Raman spectroscopy. *Annu. Rev. Anal. Chem.* **1**, 601 (2008).

107. H. A. Atwater and A. Polman, Plasmonics for improved photovoltaic devices. *Nature Materials* **9**, 205 (2010).

108. C. Wu, B. Neuner III, J. John, A. Milder, B. Zollars, S. Savoy, and G. Shvets, Large-area wide-angle spectrally selective plasmonic absorber. *Phys. Rev. B* **84**, 075102 (2011).

109. X. Liu, T. Tyler, T. Starr, A. F. Starr, N. M. Jokerst, and W. J. Padilla, Taming the blackbody with infrared metamaterials as selective thermal emitters. *Phys. Rev. Lett.* **107**, 045901 (2011).

110. Y. Cui, J. Xu, K. H. Fung, Y. Jin, A. Kumar, S. He, and N. X. Fang, A thin film broadband absorber based on multi-sized nanoantennas. *Applied Physics Letters* **99** (25), 253101 (2011).

111. A. Salandrino, A. Alu, and N. Engheta, Parallel, series, and intermediate interconnections of optical nanocircuit elements. 1. Analytical solution. *J. Opt. Soc. Am. B* **24**, 3007 (2007).

112. V. G. Veselago, THE ELECTRODYNAMICS OF SUBSTANCES WITH SIMULTANEOUSLY NEGATIVE VALUES OF ϵ AND μ. *Soviet Physics Uspekhi* **10** (4), 509 (1968).

113. D. R. Smith, Willie J. Padilla, D. C. Vier, S. C. Nemat-Nasser, and S. Schultz, Composite Medium with Simultaneously Negative Permeability and Permittivity. *Phys. Rev. Lett.* **84** (18), 4184–4187 (2000).

114. X. Huang, I. H. El-Sayed, W. Qian, and M. A. El-Sayed, Cancer Cell Imaging and Photothermal Therapy in the Near-Infrared Region by Using Gold Nanorods. *J. Am. Chem. Soc.* **128** (6), 2115–2120 (2006).

115. A. M. Gobin, M. H. Lee, N. J. Halas, W. D. James, R. A. Drezek, and J. L. West, Near-Infrared Resonant Nanoshells for Combined Optical Imaging and Photothermal Cancer Therapy. *Nano Lett.,* **7** (7), 1929–1934 (2007).

116. S. Lal, S. E. Clare, and N. J. Halas, Nanoshell-Enabled Photothermal Cancer Therapy: Impending Clinical Impact. *Acc. Chem. Res.* **41** (12), 1842–1851 (2008).

117. R. A. Pala, J. White, E. Barnard, J. Liu, M. L. Brongersma, Design of Plasmonic Thin-Film Solar Cells with Broadband Absorption Enhancements. *Advanced Materials* **21** (34), 3504-3509 (2009).

118. V. E. Ferry, M. A. Verschuuren, H. B. T. Li, E. Verhagen, R. J. Walters, R. E. I. Schropp, H. A. Atwater, and A. Polman, Light trapping in ultrathin plasmonic solar cells. *Optics Express* **18** (S2), A237-A245 (2010).

119. W. Shockley and H. J. Queisser, Detailed Balance Limit of Efficiency of p-n Junction Solar Cells. *Journal of Applied Physics* **32** (3), 510 (1961).

120. N.-P. Harder and P. Würfel, Theoretical limits of thermophotovoltaic solar energy conversion. *Semiconductor Science and Technology* **18**, S151 (2003).

121. E. Rephaeli and S. Fan, Absorber and emitter for solar thermo-photovoltaic systems to achieve efficiency exceeding the Shockley-Queisser limit. *Optics Express* **17** (17), 15145-15159 (2009).

122. W. Spirkl and H. Ries, Solar thermophotovoltaics: An assessment. *Journal of Applied Physics* **57**, 4409 (1985).

123. E. Rephaeli and S. Fan, Tungsten black absorber for solar light with wide angular operation range. *Applied Physics Letters* **92** (21), 211107 (2008).

124. R. Esteban, M. Laroche, and J. J. Greffet, Dielectric gratings for wide-angle, broadband absorption by thin film photovoltaic cells. *Applied Physics Letters* **97** (22), 221111 (2010).

125. D. W. Vernooy, V. S. Ilchenko, H. Mabuchi, E. W. Streed, and H. J. Kimble, High-Q measurements of fused-silica microspheres in the near infrared. *OPTICS LETTERS* **23** (4), 247 (1998).

126. T. Schumacher, K. Kratzer, D. Molnar, M. Hentschel, H. Giessen, and M. Lippitz, Nanoantenna-enhanced ultrafast nonlinear spectroscopy of a single gold nanoparticle. *Nature Communications* **2**, 333 (2011).